UNIVERSITY OF HELSINKI REPORT SERIES IN PHYSICS

HU-P-D278

Investigations on Physical Processes During Conductive Channel Formation in Vacuum Breakdown

Zhipeng Zhou

Helsinki Institute of Physics
Helsinki Accelerator Laboratory
Division of Materials Physics
Department of Physics
Faculty of Science
University of Helsinki
Helsinki, Finland

School of Electrical Engineering
Xi'an Jiaotong University
Xi'an, China

ACADEMIC DISSERTATION

To be presented for public examination with the permission of the Faculty of Science of the University of Helsinki, on 29th September, 2022 at 10 o'clock. The defence is open for audience through remote access.

HELSINKI 2022

ISBN 978-951-51-8389-7 (printed version)
ISSN 0356-0961
Helsinki 2022
Unigrafia

ISBN 978-951-51-8390-3 (PDF version)
http://ethesis.helsinki.fi/
Helsinki 2022
Electronic Publications @ University of Helsinki

ABSTRACT

When the applied voltage and electric field exceed a certain threshold, the breakdown of vacuum gap will occur, characterizing that its insulating capability is lost. Vacuum breakdown often occurs in applications such as vacuum circuit breakers, particle accelerators, spacecraft components, X-ray tubes, and micro-nano devices. The breakdown adversely affects the normal operation of these devices and might even cause serious safety accidents. Therefore, the study on the basic physical processes of vacuum breakdown and on improving the insulation performance of vacuum gaps is an important research direction. The formation of a conductive channel is crucial for a vacuum gap to complete the transition from an insulator to a conductor. A clear understanding on this process is an indispensable part in understanding the entire vacuum breakdown and is a prerequisite for optimizing the design of vacuum insulation. The current theories on the formation of conductive channel mostly agree that the generation of cathode glow is the starting point of constructing conductive channel, while the role of anode glow in this process is controversial. The conclusions of previous studies are mostly phenomenological descriptions for the results obtained under specific experimental conditions, without discussing the underlying mechanisms of relevant physical phenomena, their relationships, and their ultimate roles in the construction of conductive channels. Therefore, the research objectives of this dissertation are to reveal the intrinsic mechanisms and relationships of various physical phenomena related to the formation of conductive channel in vacuum breakdown, to clarify their adequacy and necessity in the process of establishing such channels, to develop the existing theories for describing the formation of conductive channel, and to provide reference and guidance for the insulation design of vacuum equipment such as vacuum circuit breakers and particle accelerators.

In the present dissertation, the light emission and electrical waveforms during vacuum breakdown were detected experimentally. The indicator of the conductive channel formation and the temporal and spatial evolution of the light emission were obtained. The key role of the cathode plasma in starting a vacuum breakdown was revealed. The secondary role of the expansion of anode glow in the construction of conductive channel was elucidated. According to the experimental results, a vacuum breakdown starts when the electric field on the cathode surface reaches about 160 MV/m, and this threshold is independent of the gap size. The generation of cathode plasma is an indicator and necessary condition of the start of vacuum breakdown, and the complete collapse of gap voltage is the indicator of conductive channel formation. During the breakdown, the cathode glow generated by the cathode plasma does not expand obviously, while the anode glow keeps expanding toward the cathode since its appearance. However, the instant when the anode glow reaches the cathode is much later than the instant when the gap voltage collapses, meaning that the expansion of the anode glow is not a necessary condition for the formation of the conductive channel, and the conductive channel can be formed even in a dark gap. It is further

speculated that the expansion of the cathode plasma to anode is the main reason for the formation of the conductive channel.

Spectroscopic and morphological analyses on the anode glow and anode surface during vacuum breakdowns have found that both the cathode and the anode provide atoms for the anode glow. The expansion mode of the cathode plasma and its significance in the formation of conductive channels are elucidated. The results indicate that the atoms provided by the anode to the anode glow contain both anode and cathode materials, because the material migration during previous breakdowns results in a contamination layer of cathode material on the anode surface. The increase in the thickness of contamination layer can lead to the attenuation or even complete disappearance of the anode material spectra in the anode glow. The cathode also provides some atoms of cathode material to the anode glow. These atoms are the product of charge neutralization and reflection at the anode surface after the ions in the cathode plasma expand and reach the anode, and they have reached the anode before the anode glow appears. Therefore, although there is no significant expansion of the cathode glow, the cathode plasma can expand to the anode without emitting light. Thus, the expansion of the cathode plasma plays a major role in the formation of conductive channels in vacuum breakdowns.

The development of vacuum breakdowns under different conditions were detected by using a streak camera with continuous time resolution, and the influence of experimental conditions on the delay between the anode glow and the cathode glow was obtained. The results reveal the main contribution of sputtering process on the anode surface to the anode glow and a new theory was proposed that the generation and expansion of the cathode plasma is the necessary and sufficient condition for the formation of conductive channels. Under the experimental conditions of this dissertation, the atoms on the anode surface leave the anode and participate in the anode glow mainly due to the sputtering effect of the cathode ion flow, rather than the heating effect of the cathode electron flow on the anode surface. This discovery complements the traditional view that the anode glow comes from heating and evaporation of the anode surface by electron flow. There is a strong linear correlation between the appearance of anode glow and the formation of conductive channels. This correlation exists because both events are the consequences of the expansion of the cathode plasma reaching the anode, but there is no causal relationship between these two events. This means that neither the appearance nor the expansion of the anode glow is necessary for the formation of conductive channels. Combining all the experimental results in this dissertation, it is proposed that the necessary and sufficient condition for the establishment of conductive channels in vacuum breakdowns is the generation and expansion of the cathode plasma.

Based on the PIC-MCC method, a simulation model for the vacuum breakdown was developed, and the distribution of particles and electric field within the vacuum gap were obtained, which visually demonstrates the construction of a conductive channel and verifies the sufficiency and necessity of the cathode plasma generation and expansion in the formation of conductive channels. The initiation of a vacuum breakdown is marked by the generation of the cathode plasma. Before the generation

of the cathode plasma, there is only electron emission current limited by the space charge effect in the gap, so the gap voltage is extremely high and the gap remains its insulation. Metal vapor is generated near the cathode due to the heating effects of electron emission, which is further ionized when colliding with electrons, subsequently building up cathode plasma. The cathode plasma counteracts the limitation of the space charge effect and the gap current starts rising rapidly. The cathode plasma expands toward the anode and the expansion front is determined by the velocity of the ions. The gap voltage is concentrated between the cathode plasma front and the anode, which accelerates the electrons emitted from the cathode plasma toward the anode and ensures the continuity of the current. With the expansion of the cathode plasma, more and more areas in the vacuum gap become quasi-neutral. The gap voltage continues to drop and the current continues to rise. When the expanding cathode plasma reaches the anode, the gap voltage drops to the lowest value while the current reaches the highest, meaning a conductive channel has been formed in the vacuum gap.

In summary, the generation of the cathode plasma and its expansion toward the anode is the necessary and sufficient condition for the formation of conductive channels in vacuum breakdown, while the anode glow is only a secondary phenomenon of the cathode plasma expansion, which does not have a decisive role in the formation of conductive channels. Some of the previous conclusions emphasizing the significance of the anode glow are only phenomenological descriptions obtained under certain conditions when the anode is overheated by electron flow, which do not account for the necessity of the anode glow for the formation of conductive channels. The conclusions obtained in this dissertation are not only consistent with the previous experimental results, but they also clarify the formation mechanism of conductive channels during vacuum breakdown in a more rigorous way, which contribute in the better understanding of fundamentals of the theory for conductive channel formation, and can contribute to the optimization of vacuum insulation design.

CONTENTS

1 INTRODUCTION

1.1 RESEARCH BACKGROUND OF VACUUM BREAKDOWN

1.1.1 CONCEPT OF VACUUM INSULATION

Since the Second Industrial Revolution emerged in the late 1860s, human society has entered the electrical age, and electric power has become indispensable for the development of the society. Electricity can not be generated or used without a variety of electrical devices, which are always composed of two parts: conductors and insulators. The role of a conductor is to conduct current, while the role of an insulator is to block it. Conductors and insulators are assembled together in a reasonable structure to enable the electrical devices to play their respective roles in the power system. Problems with either can cause failures of the individual devices or even the entire power system, bringing economic losses and safety accidents. Therefore, electrical insulation, referring to using insulating materials to isolate charged bodies of different potentials for the purpose of stopping the flow of current between charged bodies and controlling the direction of current flow, is an important issue that must be considered for the safe and reliable use of electrical energy.

Depending on the insulating medium used, electrical insulation includes solid insulation (glass, ceramics, rubber), liquid insulation (natural mineral oil, natural vegetable oil and synthetic oil), gas insulation (air, CO_2, N_2, SF_6) and vacuum insulation. However, the insulating properties of insulating materials are not permanent. When subjected to a sufficiently high voltage, insulating materials will lose their ability to block current and transform into conductive materials, and this process is called electrical breakdown.

Vacuum insulation is using vacuum environment as insulating medium. Vacuum refers to a thin gas state below atmospheric pressure. Depending on the gas pressure, vacuum can be divided into low/coarse vacuum (10^5-10^2 Pa), medium vacuum (10^2-10^{-1} Pa), high vacuum (10^{-1}-10^{-5} Pa) and ultra-high vacuum ($<10^{-5}$ Pa)[1]. According to Townsend Discharge Theory[2], the occurrence of breakdown in gases requires three prerequisites including:

(1) a high electric field to accelerate electrons;

(2) initial electrons used to trigger ionization and subsequent electron avalanche process;

(3) a gas medium to be ionized and providing ions.

When these condtions are fulfilled, gas channels will transform to a new state of matter containing a significant portion of charged particles (ions and electrons), which is called plasma. Plasma is one of the four fundamental states of matter, with the other

three being solid, liquid and gas. Unlike other states, the presence of charged particles makes plasma electrically conductive, which is exactly the reason why the insulating ablility is lost during breakdowns. The local densities of positive charged particles (usually ions) and negative charged particles (usually electrons) are almost the same in plasma, resulting in the quasi-neutral characteristics of plasma and low voltage drop across plasma.

In high vacuum (10^{-1}-10^{-5} Pa), however, the mean free path of electrons can reach the order of 0.1-1000 m[1]. This means that within a limited gap length, electrons have no chance to collide with gas molecules, so no ionization and electron multiplication can occur. Therefore, vacuum has pretty high insulating capability. However, in practice, if the voltage applied across a vacuum gap continuously increases, a breakdown can still occur. This electrical breakdown occurring in vacuum is called vacuum breakdown.

1.1.2 TYPICAL APPLICATION SCENARIOS IN WHICH VACUUM BREAKDOWN OCCURS

Typical scenarios in which vacuum breakdown occurs include vacuum circuit breakers[1], particle accelerators[3-6], triggered vacuum switches[7, 8], spacecrafts[9, 10], X-ray tubes[11-13], and Micro-Nano Devices[14-16]. Except for triggered vacuum switches which make use of vacuum breakdown, most vacuum devices do not want vacuum breakdown to occur. This is because the occurrence of vacuum breakdown in these systems often results in loss of normal functionality, potential irreversible damage, or even larger security risks. Therefore, many researchers focus on the physical processes of vacuum breakdown, hoping to propose effective measures for the improvement of vacuum insulation capacity based on deeper understanding of the vacuum breakdown evolution. In the following, the occurrence and effects of vacuum breakdown are introduced by taking vacuum circuit breakers and particle acceleartors as examples.

1.1.2.1 Vacuum circuit breakers and vacuum interrupters

Vacuum circuit breaker is a mechanical switching device that takes vacuum as insulating and interrupting medium, which can not only close, open and carry current under normal circumstances, but also carry and open abnormal current within specified time. A vacuum interrupter is the core component used for insulation and arc extinguishing in vacuum circuit breakers, consisting of insulating shell, contacts, conducting rod, bellows, shield, etc. The interior of it is a vacuum environment (10^{-4} Pa), as shown in Figure 1-1. Compared with SF_6 (a gas with pretty good insulation and arc extinguishing properties, but with a very serious greenhouse effect, 23900 times that of carbon dioxide) circuit breakers, which are widely used in high voltage power systems, the most obvious advantage of vacuum circuit breakers is that they do not produce the greenhouse effect. In addition, it has the advantages of long life, maintenance-free, small size and low noise.

The idea of using vacuum as a switching medium appeared in 1890, when Enholm applied for a patent called “Device for transforming and controlling electric currents”[17]. Over the next three decades, patents for vacuum switches increased at a rate of almost one per year[18-22], but vacuum switches during this period were limited to low-power systems. In 1926, Professor Sorensen's team at the California Institute of Technology successfully switched a current of 900 A at 40 kV voltage using a vacuum switch[23, 24]. In the late 1950s, The invention of the transverse magnetic field contact structure has increased the rated short-circuit breaking current of the vacuum circuit breaker to the level of 30 kA[25]. In the 1960s, with the progress of vacuum material smelting technology and contact structure research, vacuum circuit breakers capable of breaking 12.5 kA, 26 kA and 31.5 kA at a rated voltage of 15 kV were introduced one after another[1]. This has led to the application of vacuum circuit breakers into high voltage, high capacity power systems. In the late 1970s, Toshiba Electric Co., Inc. of Japan developed a vacuum interrupter with axial magnetic field contacts, which further improved the breaking capacity of vacuum circuit breakers[1].

Currently, vacuum circuit breakers are widely used in medium voltage distribution systems from 3.6-40.5 kV[1] and are developing to higher voltage levels. Once the vacuum breakdown occurs between the two contacts of the vacuum interrupter, a vacuum arc is formed in the vacuum gap, causing the vacuum circuit breaker to lose its isolation and protection role as a switching device. Therefore, studying basic physical process of vacuum breakdown and trying to improve the insulation capability of the vacuum gap is a challenge that vacuum circuit breakers must face when moving to higher voltage levels.

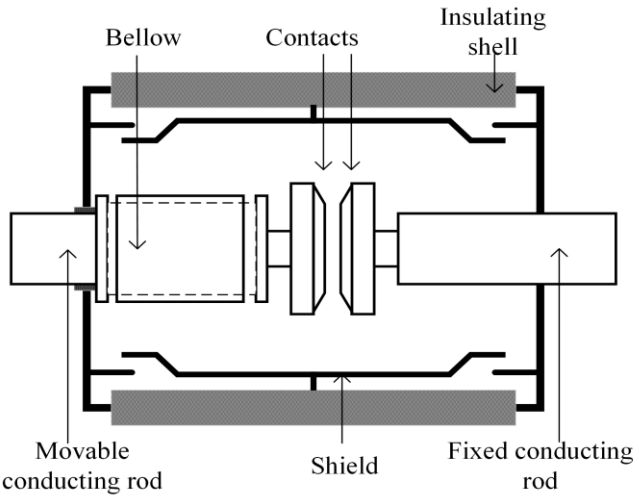

Figure 1-1 Structure diagram of vacuum interrupter

1.1.2.2 Particle accelerator

Vacuum breakdown may also occur in charged particle accelerators[6]. Charged particle accelerators, often referred to as “particle accelerators” or “accelerators”, are devices that confine microscopic charged particles to a specific area and accelerate

them through an electromagnetic field, thereby allowing the particles to reach higher energies[3]. Accelerators can accelerate various types of charged particles, including electrons, protons, alpha particles, and heavier ions, to various energies; they can also be used to generate new secondary particles by the interaction of the accelerated particles with other particles or matter. To ensure the efficiency of the acceleration and the collimation of the particle beam, accelerators usually use vacuum environment. High-energy charged particle beams obtained in accelerators can be used as an important tool for exploring the properties, internal structure and interactions of atomic nuclei and particles, and also have important and widespread practical applications in various aspects of industrial and agricultural production, medical and health care, science and technology.

There are many ways to classify particle accelerators. In terms of the types of accelerated particles, they can be divided into electron accelerator, proton accelerator, heavy ion accelerator, etc.; from the point of view of the trajectory of the particles during acceleration, they are divided into linear accelerators, cyclotrons, etc.; and by the type of acceleration electric field, they can be divided into high voltage electrostatic field (HVES) accelerator and time-varying electromagnetic field (TVEM) accelerator[26, 27]. Accordingly, from the technical process of accelerating energy acquisition, the HVES accelerator uses a single-time acceleration technology, also known as voltage drop acceleration technology, which obtains higher energy at one time on the premise of providing a higher potential difference; while the TVEM accelerator uses the cumulative acceleration technique, that is the charged particles obtain higher energy by accumulation of multiple smaller potential differences.

HVES accelerators use a linear structure in which a high DC voltage is applied across the two ends of the accelerator tube in vacuum. Charged particles move from one end to the other under the action of the electric field, accelerating to desired energy. When the voltage across the two ends exceeds a certain threshold, a vacuum breakdown occurs inside the tube, the accelerating electric field disappears, thus making the accelerator lose its acceleration capability. Therefore, vacuum breakdown is a major limiting factor for the acceleration capability of HVES accelerators.

To further increase the energy of particles, cumulative acceleration technology must be used. The cumulative acceleration technique requires the use of a time-varying electromagnetic field to ensure that the motion of the particles and the changes in the accelerating electric field are in sync[28]. The acceleration structure of the TVEM accelerator can be linear or spiral. A typical example of a TVEM accelerator in a spiral orbit is a cyclotron. Cyclotrons use a magnetic field to move charged particles in a circular orbit and accelerate the particles by an electric field of the same frequency in each cycle. A typical example of a TVEM accelerator in a linear orbit is the CLIC (Compact Linear Collider) project[29] being carried out by the European Organization for Nuclear Research (CERN). The goal of the CLIC project is to achieve the collision of electrons and positrons at the energy of 3 TeV. The project will be implemented in three phases, with the future construction length reaching from 11 km to 50 km. The CLIC project uses a linear structure and radio frequency electromagnetic waves to provide an accelerating electric field. Considering that the electromagnetic waves in

free space are horizontal waves (the direction of the electric field is perpendicular to the direction in which the electromagnetic waves travel), it is not possible to provide an accelerated electric field for electrons in the direction of electromagnetic wave propagation. As a result, CLIC uses specially designed waveguide structures to create vertical electric field components in space for electron acceleration. To save costs and improve acceleration efficiency, the electric field gradient in the structure used by CLIC will reach 100 MV/m. With such a high electric field gradient, vacuum breakdown can also occur on the metal walls of the accelerator chamber. The occurrence of vacuum breakdown will increase the energy consumption of the accelerator, reduce the beam luminosity of the accelerated particles and cause instability of the device, so the study on vacuum breakdown mechanism is also an important subject in the implementation of the CLIC project[4, 5, 29-32].

1.2 CURRENT SITUATION OF RESEARCH ON CONDUCTIVE CHANNEL FORMATION IN VACUUM BREAKDOWN

1.2.1 OVERVIEW OF VACUUM BREAKDOWN PROCESS

Vacuum breakdown is an electrical breakdown that occurs in a vacuum environment, transforming the vacuum gap from an insulating state to a conducting state. As mentioned above, the occurrence of breakdown in gases requires three prerequisites: initial electrons, critical electric field, and ionizing media (i.e. gas molecules). Only in this way can a conductive channel consisting of plasma be established in the gap. Similarly, the transition of a vacuum gap to the conductive state also requires plasma to form a conductive channel, so all the three conditions mentioned above is indispensable. The voltage applied across a vacuum gap can obviously establish an electric field in the gap, while the mechanisms for the generation of the initial electrons and the ionized medium are different from that in gas.

In fact, according to the field electron emission theory[33, 34], the free electrons inside metals can tunnel the surface barrier and enter vacuum when there is a high electric field at the metal surface. These electrons form electron emission. The current density of the electron emission can be described by the Fowler-Nordheim equation as follows:

$$J_{\mathrm{FN}}=1.54\times10^{-6}\frac{E_{\mathrm{Loc}}^{2}}{\phi_{\mathrm{w}}}\exp\left(-6.83\times10^{9}\frac{\phi_{\mathrm{w}}^{1.5}}{E_{\mathrm{loc}}}\right) \tag{1-1}$$

in which J_{FN} is the current density of field electron emission (in A/m^2); E_{Loc} is the local electric field at the emission point (in V/m); φ_{w} is the work function of the material (in eV). Many experimental results have shown that the electron emission in a vacuum gap can be described by Equation (1-1)[1, 35]. Therefore, initial electrons are provided by field electron emission from the cathode surface during a vacuum breakdown.

In a vacuum environment, the molecule density of residual gas is extremely low, so

the medium used to form the conductive channel can only be supplied by metal electrodes. Therefore, vacuum breakdowns use metal vapor as the ionizing medium, and the vacuum arc (final stage of vacuum breakdown) is a metal vapor arc. The impact ionization of electrons and metal vapor forms plasma, which eventually builds up a conductive channel in the vacuum gap.

According to the physical processes that occur in a vacuum gap, the evolution of a vacuum breakdown can be divided into three stages[1, 36]. Figure 1-2(a) and (b) show simplified diagrams of vacuum breakdowns under impulse voltage and DC voltage, respectively. The first stage is the pre-breakdown stage, in which only electron emission from the cathode is present. Due to the small value of electron emission current, the voltage across the gap remains high and the gap is basically insulated. The end of the pre-breakdown stage is marked by a sudden rise in the gap current, which means that ionization due to electron-vapor interaction begins. The number of charged particles grows rapidly from this instant, forming the initial plasma. This instant also marks the beginning of a vacuum breakdown, leading the breakdown into the second stage. In the second stage, the gap current gradually increases, while the gap voltage decreases at the same time. The vacuum gap is gradually filled with plasma during this phase, and a conductive channel is then formed. Therefore, the second stage is called conductive channel formation stage. The end of the second stage is marked by the complete collapse of the gap voltage, after which the breakdown evolution enters the final stage. The vacuum gap in the third stage is characterized by high current and low voltage. The equivalent resistance of the gap is very small and the current variation is completely controlled by the parameters of external circuit. This low voltage, high current plasma channel characterizes an electric arc, so the third stage is also called as vacuum arc stage[37].

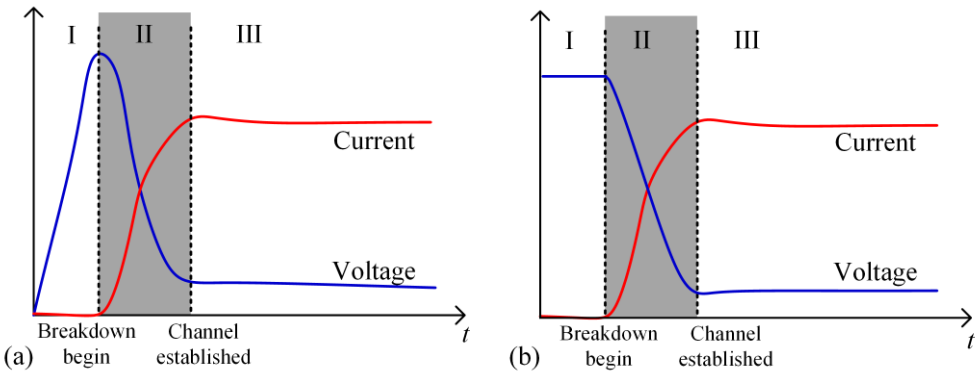

Figure 1-2 Simplified diagrams of vacuum breakdown evolution under impulse (a) and DC (b) voltage

The research on the vacuum arc stage mainly includes experiments and simulations of arc pattern, arc parameters and the interactions between arc and electrodes[1, 36, 38-42], aiming at the better control and faster extinguishing of vacuum arc. The study in this dissertation focuses on the stage of conductive channel formation, as shown in the shaded area in Figure 1-2. In-depth study of this stage can help to find the key physical processes that cause the failure of vacuum insulation and provide a clearer direction for insulation design. Since the conductive channel formation is preceded by the pre-

breakdown stage, the current research status on these two stages is summarized in the following parts.

1.2.2 STUDIES ON PRE-BREAKDOWN STAGE OF VACUUM BREAKDOWN

The core problem of the research on the pre-breakdown stage is to discuss the threshold conditions at which vacuum breakdown occurs. That is, what conditions can cause the rapid rise of gap current. According to the breakdown threshold conditions, there are two main theories for the trigger mechanism of vacuum breakdown: cathode-dominated breakdown and anode-dominated breakdown.

1.2.2.1 Cathode-dominated breakdown theory

In the discussion on vacuum breakdown mechanism, cathode-dominated breakdown theory is more widely accepted. Typical experimental evidence is that the breakdown process takes the local electric field of the cathode surface as the threshold value.

The most important process in the pre-breakdown phase is the field electron emission, which not only provides initial electrons, but also is a prerequisite for other subsequent physical processes related to breakdown. As can be seen from Equation (1-1), current density of the emitted electrons is directly determined by the local electric field at the cathode surface. In1953, Dyke and his colleagues made the first precise measurement of the field electron emission in a vacuum gap[35, 43]. They used a precisely-machined single crystal tungsten needle as a cathode, which forms a vacuum gap with a spherical anode with a gap length of 4-10 cm. The tip radius of tungsten needles is in the micron magnitude and can be accurately measured using an electron microscope, which makes it possible to accurately calculate the electric field on the cathode surface. They found that the measured current values can be described by using the Fowler-Nordheim equation in a wide range (6 A/cm^2-6×10^6 A/cm^2) when there is no breakdown. When the current is higher, the limitation of the space charge effect[44] causes slight deviation of the measured current from the Fowler-Nordheim equation. When the gap voltage continues to rise, the current rises rapidly by more than two orders of magnitude. At this point, a vacuum breakdown occurs. By comparison, it was found that the field emission current density from tungsten needles of different sizes is always in the range of 4×10^7-7×10^7 A/cm^2 when the gap breaks down, and the corresponding electric field at the cathode tip is approximately 7×10^7 V/cm[35, 43]. In addition, the authors excluded the possible effects of vapor and ions from the anode on breakdown by using short pulse voltages. They convincingly demonstrated that the breakdown under the tested system is determined by the cathode emission, and that the determinant is the current density of the electron emission or the intensity of the local electric field. After breakdowns, the cathode tip melts significantly, increasing the radius by two orders of magnitude. They attributed the breakdown to thermal instability at the cathode tip and calculated the temperature of the cathode. The results show that the cathode temperature can exceed the melting point in a short time under

the critical current density for breakdown initiation.

However, during the study of vacuum breakdown between plane-parallel electrodes, many researchers[45-48] found that the breakdown field varied with the gap length and that the calculated breakdown field was at least one order of magnitude smaller than the results of Dyke. Alpert et al.[48] explained this phenomenon by introducing the concept of electric field enhancement factor, and attributed the variation of the breakdown field with gap length to the change of the enhancement factor. In fact, microscopic analysis reveals that there are inevitably various defects on the cathode surface, including micro protrusions, grain boundaries, particles, cracks and so on[49]. The presence of these defects can enhance the local electric field at the microscopic surface, and the corresponding enhancement factor is called microscopic electric field enhancement factor $\beta_{\mathrm{m.}}$ At the macroscopic level, as the gap length increases, the electric field between finite-sized plane-parallel electrodes is no longer uniformly U/d, but there may be an enhancement of electric field at the edge of the electrodes, which is represented by geometric electric field enhancement factor β_{g}[36, 50]. Therefore, the electric field in the Fowler-Nordheim equation should be replaced by:

$$E_{\mathrm{loc}}=\beta_{\mathrm{m}}\beta_{\mathrm{g}}E \tag{1-2}$$

$$E=u_{\mathrm{gs}}/d_{\mathrm{g}} \tag{1-3}$$

in which u_{gs} is the gap voltage (in V); d_{g} is the gap length (in m). The product of the two electric field enhancement factors ($\beta=\beta_{\mathrm{m}}\times\beta_{\mathrm{g}}$) can be calculated according to the current-voltage curve for the field electron emission[48, 51, 52]. After considering the effects of the enhancement factors, Alpert et al. found that the local breakdown field, which was exactly the same as that obtained by Dyke (near 7×10^{7} V/cm), did not change with the gap size (10^{-4} cm-10 cm) and electrode geometry. Some other researchers also obtained similar results in experiments[31, 53-55].

Researchers, who support the theory of cathode-dominated breakdown, have attributed the onset of breakdown to a thermal instability process, i.e. the field electron emission current results in an excessive heating of local cathode surface through Joule and Nottingham effects[56]. Mesyats et al.[36, 53, 57-60] proposed an explosive electron emission mechanism (known as the "Ecton" model). They believe that microprotrusions quickly reach the critical temperature of the cathode material under the heating of critical electron emission current density, causing explosions of microprotrusions to form plasma. Timko et al.[61, 62] established a simulation model for vacuum breakdown based on the PIC (Particle-In-Cell) algorithm, and the results show that with a certain neutral particle evaporation rate, a positive feedback of particle emission can be formed at the cathode surface under positive ion bombardment, resulting in dense plasma. Kyritsakis et al.[63] performed multiscale atomic simulations and obtained the evaporation rates required by the positive feedback particle emission. They also reported the mechanism of thermal instability on the nano tip of metal cathode. Since the time and spatial scale of the initial breakdown is very small, no experimental results have been able to clearly distinguish the above two possible mechanisms. However, whether the microprotrusions explode

or evaporate rapidly under positive feedback, what happens on the cathode surface is an extremely fast process. The result of this fast process is the formation of plasma near the cathode. The appearance of cathode plasma allows electron emission current at the cathode surface to break through the limitation of the space charge effect. In addition, a significant increase in temperature at local cathode surface also changes the mechanism of electron emission from a simple field emission to a thermal-field emission[64, 65]. As a result, the gap current begins to rise rapidly under such conditions and the vacuum breakdown is initiated.

1.2.2.2 Anode-dominated breakdown theory

The anode-dominated breakdown theory holds that vacuum breakdown occurs in the case of thermal instability on the anode surface, i.e. the anode evaporates a large amount of vapor under the heating of electron flow from the cathode, which collides with electrons to induce ionization and subsequent breakdown. The experimental evidence for the anode-dominated breakdown mechanism is that the anode material has an effect on the breakdown voltage, and that the anode material with poor thermal conductivity corresponds to a lower breakdown voltage[1, 36, 66].

Utsumi[67] believes that both the cathode and the anode are possible to trigger a vacuum breakdown, and that the effect of the anode is important when the gap is greater than a few millimeters. The gap length is also used as a standard to distinguish cathode-dominated and anode-dominated breakdown in the book of Slade[1]. He believes that the breakdown in small gaps is dominated by cathodes, while the breakdown in gaps larger than 2 mm is mainly controlled by the process at the anode side. Charbonnier et al.[68, 69] consider that the transition between the cathode-dominated and the anode-dominated mechanisms depends on the field enhancement factor β at the cathode. If β is less than a certain value, the breakdown is triggered at the anode; if β is greater than the certain value, the breakdown is triggered at the cathode. Chalmers's team[70] and Yen's team[59], on the other hand, linked the breakdown mechanism to the breakdown delay, with the short delay breakdown corresponding to the cathode-dominated mechanism and the long delay breakdown corresponding to the anode-dominated mechanism. Jüttner[71] opposed to the anode-dominated breakdown theory and argued that the effect of anode material on breakdown voltage is due to the migration of the anode material to the cathode, which leads to changes on the cathode surface during subsequent breakdowns. Mesyats believes that vacuum breakdown begins with the production of "Ecton" and cathode plasma at the cathode, regardless of the anode vapor production or not[36]. The production of anode vapor may only play an auxiliary role in the production of cathode plasma.

For the detailed mechanism by which the anode triggers a breakdown, Utsumi[67] suggested that the heating of the anode surface by the cathode electron flow is responsible for the production of vapor and subsequent ionization. Davies et al., on the other hand, considered the heating and evaporation mechanism proposed by Utsumi as unreasonable[72]. Near the vacuum breakdown threshold, electrons reach

the anode with energy of up to tens of keV, and the ionization collision cross section between electrons and anode vapor is small under such conditions. According to the estimation of Davies, even if the entire anode evaporates into metal vapor, such a low probability of impact ionization cannot trigger a breakdown. When calculating anode temperature and evaporation, the above two teams considered the heating effect of electron flow on the anode as a surface energy flow. Slade[1], on the other hand, takes into account the penetration depth of electrons inside the anode. According to the calculation by Lamarsh[73], electrons with energy of tens of keV or more can penetrate into metals with a depth of microns. Slade believes that the electron energy is deposited in a micro-volume of micrometer thickness below the anode surface, causing a significant increase in temperature within that volume. The rapid increase in temperature in turn leads to the generation of large amounts of metal vapor and anode plasma on the anode surface in the form of micro-explosions, which can trigger breakdowns.

The studies on the pre-breakdown stage can be summarized as follows:

(1) All the researchers agreed that field electron emission at cathode microprotrusions was the initial and necessary process in vacuum breakdown;

(2) The controversial point of cathode-dominated and anode-dominated breakdown theory lies in the way the initial plasma is produced. Further, it is actually the source of the initial metal vapor;

(3) For cathode-dominated theory, the initial metal vapor is provided by the cathode. The impact ionization of metal vapor by electrons forms the initial plasma near the cathode;

(4) For the anode-dominated theory, although it is believed that the initial metal vapor is provided by the anode, there is no clear explanation as to how the vapor forms the initial plasma.

1.2.3 STUDIES ON CONDUCTIVE CHANNEL FORMATION STAGE OF VACUUM BREAKDOWN

The establishment of a conductive channel in vacuum breakdown requires two necessary conditions: initial plasma formation and plasma expansion. While the analysis of the pre-breakdown phase in the previous section discussed the formation of initial plasma, this section will discuss the plasma expansion.

Compared with the pre-breakdown stage, the researches on the conductive channel formation stage are less. Due to the formation of the initial plasma and the expansion of the plasma, the conductive channel formation stage is often accompanied by luminescence near the cathode and the anode[1, 36, 74-79]. Therefore, most researches for this stage is based on experimental observation methods, with the light radiation in the gap as observation object. According to existing experimental results, cathode glow during vacuum breakdown always precedes anode glow. So far, at least, there has been no experimental evidence that anode glow precedes cathode glow.

Based on these results, the vast majority of researchers hold a unified view on the role of cathode glow in the formation of conductive channels, that is, the production of cathode glow (cathode plasma) is a necessary prerequisite for the development of vacuum breakdown and the formation of conductive channels[1, 36]. However, the role of anode glow in is still controversial.

Mesyats[53, 80] observed the formation of conductive channels in a 0.35 mm vacuum gap and found that the cathode glow appears at the beginning of breakdown and then gradually expands toward the anode. The anode glow occurs 8-10 ns later than the cathode glow and expands toward the cathode. When comparing the evolution of light radiation and current, they found that the instant when cathode glow and anode glow meet correspond to the instant when the current reaches its peak. Inada et al.[76] conducted a breakdown experiment in a 3 mm vacuum gap composed of 1 mm diameter copper rods and found that the cathode glow appeared first, but basically did not expand. They also observed that the anode glow expanded toward the cathode and eventually bridged the entire gap, and the instant when the anode glow reached the cathode coincided with the instant when the gap voltage collapsed. Therefore, they proposed that the expansion of anode glow and the formation of the light radiation channel are necessary for the establishment of plasma channel in vacuum gaps, that is, the formation of conductive channel needs to rely on the expansion of anode glow. Chalmers et al.[81] performed similar experiments with a 0.5 mm tip-plane gap and derived the same conclusion. The above researchers believe that cathode glow and anode glow are cathode plasma jet and anode plasma jet, respectively, and anode plasma is produced as a result of anode heating by the cathode electron flow. Slade[1] argues that whether anode glow plays a decisive role in the formation of conducting channels depends on the gap size and the corresponding breakdown voltage. At gap lengths less than 0.5 mm (breakdown voltage less than 40 kV), the formation of the conductive channel depends mainly on the expansion of the cathode plasma; at gap lengths greater than 2 mm (breakdown voltages greater than 90 kV), an explosion and anode plasma can be generated on the anode surface, which plays a key role in the establishment of conductive channels. The meeting of two plasma jets in the vacuum gap leads to the establishment of a conductive channel. Maitland and Hawley[82] found similar results as Slade through high-speed imaging of the vacuum breakdown process. Yang et al.[83] have established a two-dimensional PIC model to simulate the development of vacuum breakdown, and their model takes into account the sputtering process of the anode. According to the results, a vacuum gap of 6 μm forms a conductive channel after 0.6 ns, and the conductive channel is formed when the single charged copper ions fill the entire gap. Shmelev[84] simulated the conductive channel formation in a 30 μm vacuum gap using the PIC method, which does not take into account the generation of anode plasma. According to the results, the cathode plasma expands toward the anode at a speed of 20000 m/s, and the gap voltage drops to a vacuum arc level (16 V) after 1.5 ns, establishing a conductive channel. Nefedtsev et al.[85-87]simulated the cathode plasma expansion in a 1 mm gap using a fluid method, obtaining an expansion speed of 12500 m/s. Simulations by Shmelev and Nefedtsev show that it is possible to establish conductive channels in vacuum gaps only by the expansion process of the cathode plasma.

From the above analyses, it can be seen that the mechanism of conductive channel formation given by existing studies is only an intuitive description of the results obtained under specific conditions. Researchers have not investigated the intrinsic mechanisms of the relevant physical phenomena, their interrelationships, and their adequacy and necessity in the process of conductive channel establishment. This makes the existing theory for conductive channel formation less rigorous and not complete. However, the conductive channel formation is the key process for a vacuum gap to complete the transition from insulation to conduction. A clear understanding of this process is necessary to understand the whole process of vacuum breakdown evolution and is a prerequisite for optimizing the design of vacuum insulation.

1.3 PURPOSE AND STRUCTURE

The research objectives of this dissertation are to reveal the intrinsic mechanisms and interrelationships of various physical phenomena related to the conductive channel formation stage of vacuum breakdown, to elucidate their adequacy and necessity in the process of conductive channel establishment, to improve the existing theory of conductive channel formation, and to provide reference and guidance for the insulation design of vacuum equipment such as vacuum circuit breakers and particle accelerators. Three publications produced during this project are mainly included in this dissertation as follows.

1.3.1 LIST OF PUBLICATIONS

Publication I: Direct Observation of Vacuum Arc Evolution with Nanosecond Resolution

Zhou, Zhipeng, Andreas Kyritsakis, Zhenxing Wang, Yi Li, Yingsan Geng, and Flyura Djurabekova. 2019. Scientific Reports 9(1):7814.

Publication II: Spectroscopic Study of Vacuum Arc Plasma Expansion

Zhou, Zhipeng, Andreas Kyritsakis, Zhenxing Wang, Yi Li, Yingsan Geng, and Flyura Djurabekova. 2020. Journal of Physics D: Applied Physics 53(12):125501.

Publication III: Effect of the Anode Material on the Evolution of the Vacuum Breakdown Process

Zhou, Zhipeng, Andreas Kyritsakis, Zhenxing Wang, Yi Li, Yingsan Geng, and Flyura Djurabekova. 2021. Journal of Physics D: Applied Physics 54(3).

1.3.2 STRUCTURE OF THIS DISSERTATION

Chapter 2 is based on publication I. The second chapter describes experimental observations of the main physical phenomena and processes during vacuum breakdown and its development. First, the experimental platform adopted in this dissertation is introduced. Then, the voltage and the current waveforms of the vacuum

breakdown process were measured, with which the development stage and influencing factors of the breakdown process were analyzed. After that, the space-time evolution law of light radiations in the process of vacuum breakdown is given based on ICCD (Intensified Charge-coupled Deivece) camera shots with the ability of time resolution in nanosecond. The electron microscope was used to observe the changes in the shape of the electrode surface before and after the breakdown in these experiments. Finally, the relationship between cathode glow, cathode plasma and vacuum breakdown is discussed, and the role of the expansion process of anode glow in the formation of conductive channels is analyzed.

Chapter 3 is based on publication II, where the spectral analysis of the vacuum breakdown process was carried out. First, the spectral distributions of electrode combinations of different materials under different experimental conditions are observed and the main spectral components of the anode glow are obtained. Then, the contributions of cathode and anode materials in the anode glow and the effects caused by the material transfer during the breakdown process were analyzed. Finally, the expansion mode of the cathode plasma during breakdown and its role in the establishment of the conductive channel are discussed according to the participation of cathode material atoms in the anode glow.

Chapter 4 is based on the publication III, which investigates the electrode physical processes corresponding to the anode glow and their relationship with the formation of conductive channels. First, the delay time of the anode glow with respect to the cathode glow under different anode materials and different experimental conditions is obtained using a streak camera with capability of continuous time resolution. Based on the influence of experimental conditions on the anode glow delay, the rationality of the evaporation process and the sputtering process on the anode surface in leading to the anode glow are discussed, respectively, and the main physical mechanism for the generation of the anode glow is obtained. Then, by analyzing the correlation between the instant of the anode glow appearance and the instant of the conductive channel formation, the relationship between the two physical processes is derived, and the role of the anode glow appearance in the conductive channel formation is further elucidated. Finally, the necessary and sufficient condition for the formation of the conductive channel is proposed by combining these results with the results of the two former chapters.

Chapter 5, which has not yet been published, established a simulation model of the vacuum breakdown process based on the PIC-MCC algorithm to simulate the state transition of the vacuum gap from insulation to conduction. According to the simulation results, the particle distribution, the electric field distribution, and the waveforms of voltage and current during the construction of the conductive channel are analyzed and the experimentally obtained mechanism of the conductive channel formation is verified. Finally, based on the experimental and simulation results, the evolution law of the physical processes related to the conductive channel formation stage of vacuum breakdown is summarized, and suggestions for the design of vacuum insulation are provided.

1.3.3 AUTHOR'S CONTRIBUTION

Publication I. The author planned and conducted all the experiments, analyzed the majority of the results, produced the figures and prepared the manuscript.

Publication II. The author made the experimental plan based on further analysis of the results in publication I, analyzed the results, plotted the figures and wrote the manuscript.

Publication III. The author planned and conducted all the experiments, proposed methods for analyzing the results and performed the majority of the post-experiment calculation. The figures and manuscript were also prepared by the author.

Chapter 5. The author established the simulation model, ran the simulation, performed the postprocessing, analyzed the results, and prepared the figures and words.

2 EXPERIMENTAL STUDY OF SPATIAL AND TEMPORAL EVOLUTION OF LIGHT RADIATION AND WAVEFORMS DURING VACUUM BREAKDOWN

2.1 OVERVIEW

In the process of vacuum breakdown, the metal electrodes continuously provide electrons and metal vapor to the gap, so that the gap is gradually filled by plasma under the joint action of the ionization process and the expansion process, and eventually changed from insulating to conductive state. The voltage and current of the gap vary during breakdowns, characterizing the change of the gap conductivity and the stage of the breakdown evolution.

The occurrence and development of vacuum breakdown is often accompanied by light radiation, which is the result of particle interaction in plasma, so the spatial distribution and temporal evolution of light radiation can reflect to some extent the evolution of plasma in the gap. In addition, the interaction between the plasma and the electrode during the vacuum breakdown leaves traces on electrode surfaces, so the change of the surface morphology of the electrodes can provide reference information for the analysis of the plasma state.

In this chapter, preliminary experimental observations will be described of voltage, current, light radiation and electrode morphology during vacuum breakdown. The physical processes behind the light radiation and their roles in the evolution of vacuum breakdown will be analyzed by combining the information of voltage, current, light radiation and electrode morphology.

2.2 EXPERIMENTAL PLATFORM FOR VACUUM BREAKDOWN

Figure 2-1 shows the experimental platform established in this research work. The main devices and signals in the diagram are indicated by the following letters: A-vacuum chamber; B-pulsed high-voltage source; C-four-channel oscilloscope; D-digital time delay generator (SRS DG645); E-ICCD camera (Andor DH334T-18U-04); F-high voltage output cable; G-grounded cable; H-high-voltage probe (NorthStar PVM-7); I-current sensor (Pearson Model 6595); J-monitor signal of ICCD camera, indicating the exposure interval of the camera; K-trigger signal to ICCD camera; L-trigger signal to oscilloscope; M-trigger signal to the pulsed high-voltage source.

Vacuum breakdown experiments are carried out in a demountable stainless-steel chamber (hereinafter referred to as vacuum chamber), where the pressure can be reduced to 10^{-4} Pa. The experiments in this dissertation were conducted under $2.5\times10^{-}$

^{4} Pa. The upper and lower conducting rods in the vacuum chamber are connected to the two terminals outside the chamber. A pair of metal electrodes are mounted on the two conducting rods in the chamber, and the distance between the electrodes can be adjusted stepwise between 0-10 mm by a micrometer manipulator which was mounted at the lower end of the chamber. There are three observation windows on the side wall of the chamber, through which the breakdown process can be observed.

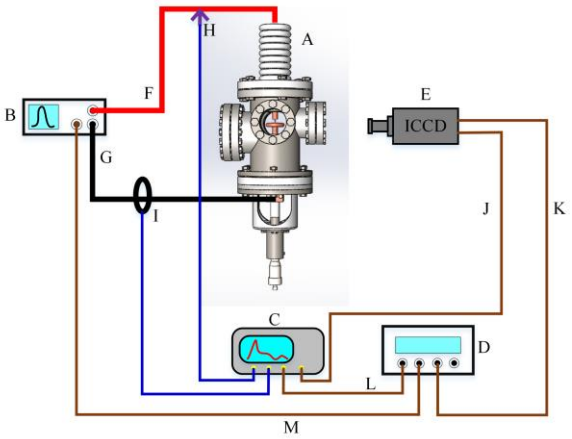

Figure 2-1 Schematic diagram of the vacuum breakdown test platform

A pulsed high-voltage source is used to trigger vacuum breakdowns. The peak voltage is adjustable between 0 and -50 kV, and the pulse width is between 1 μs and 5 μs. No-load equivalent circuit for the high-voltage source is shown in Figure 2-2. The discharge process of the voltage source is equivalent to the series connection of a charging capacitor (C_1, 0.15 μF), a current limiting resistor (R_1, 500 Ω) and a switch. In the figure, A1 and A2 are high voltage output terminal and ground terminal respectively, which are used to provide output voltage to the load. A discharge resistor (R_2, 40 kΩ) is in parallel with the load to release the charge stored in the load after the voltage source is switched off to ensure the operation safety. The voltage source receives optical trigger signal to output voltage pulse, and the pulse width of the voltage is determined by the pulse width of the trigger signal.

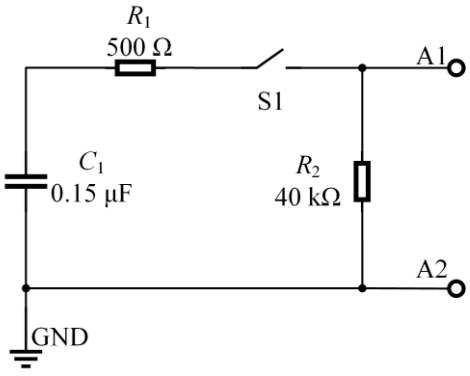

Figure 2-2 No-load equivalent circuit diagram of pulsed high-voltage source

Figure 2-3 shows the waveform of the no-load output voltage, with the peak voltage set to -10 kV and the pulse width set to 5 μs. The voltage was measured with the high-voltage probe in Figure 2-1. Upon receiving the trigger signal, the output voltage of the voltage source rises rapidly, with a rise time (10% to 90% maxiumum) of

approximately 140 ns. The duration when the output voltage remains at the peak is approximately 5 μs. After the voltage source is switched off, the charge stored in the load capacitance is gradually released through the discharge resistor (R_2, 40 kΩ) in Figure 2-2, resulting in a gradual drop in voltage.

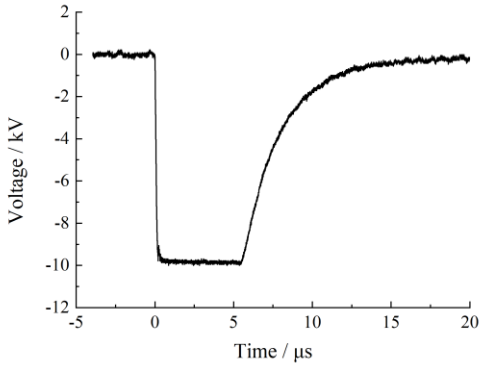

Figure 2-3 No-load output voltage waveform of pulsed high-voltage source

The high voltage output terminal (A1) and ground terminal (A2) of the voltage source are connected to the upper and lower electrodes in the chamber through the terminals of the vacuum chamber, respectively. The output of the pulse source is negative high voltage, so the upper electrode in the vacuum chamber is the cathode and the lower electrode is the anode. The electrode structure used in the experiments is a tip-plane structure, as shown in Figure 2-4(a). The upper tip electrode is the cathode, and the plane electrode below is the anode. The cathode has a diameter of 1 mm and a tip angle of 15°. The diameter and thickness of the anode are 40 mm and 10 mm, respectively. The distance between the cathode and anode is in the range of 0.5-5 mm. In fact, in order to replace the anode sample quickly in the experiments, the anode structure consists of two parts, the fixture and the replaceable anode plate, as shown in Figure 2-4(b). The replaceable anode sample has a diameter of 20 mm and a thickness of 7 mm, of which 5 mm sinks into the groove of the anode fixture. The gap length between the cathode and the anode refers to the distance between the tip of the cathode and the surface of the replaceable anode. The electrode material used in this chapter is copper.

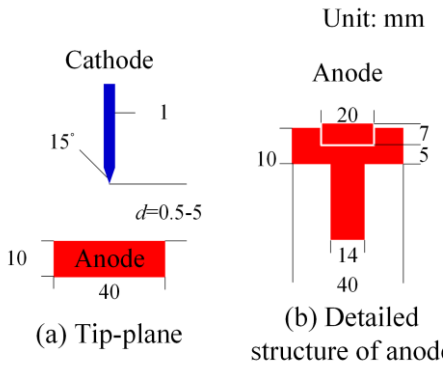

Figure 2-4 Schematic diagram of electrode structure

The light radiation during vacuum brekadown experiments was observed by using an ICCD camera, whose structure and working principle are shown in Figure 2-5. ICCD camera, namely intensified charge-coupled device camera, is widely used for imaging

analysis of fast and low-light processes. The ICCD camera consists of two parts: the image intensifier and the CCD camera. The interior of the image intensifier mainly includes a photocathode, a micro-channel plate (MCP) and a fluorescent screen. The MCP is a special optical fiber device, consisting of many microchannels (usually glass) arranged together. The inner wall of the microchannel is coated with secondary electron emitting material. A DC high voltage is applied across the MCP to produce an electrostatic field in the channels; the incident electrons can excite multiple secondary electrons on the channel wall when passing through the microchannels; these secondary electrons are accelerated by the electrostatic field and generate more electrons after bombarding the channel wall. In this way, the avalanche effect of electrons is formed, and the input signal is amplified, resulting in a large number of electrons emitted at the output of the MCP, thus achieving electron multiplication. The electron multiplication of MCP can be adjusted by the voltage applied. As shown in Figure 2-5, light radiation from the observed object is projected on the photocathode of the ICCD through lens; the photocathode converts incident photons into electrons by the photoelectric effect; the electrons move toward the MCP driven by an electric field between the photocathode and the MCP; the electrons are multiplied after passing through the MCP, resulting in significant enhancement of the measured signal; electrons, after multiplication, bombard a fluorescent screen under the acceleration of an electric field and produce visible light; the luminescence of the fluorescent screen reaches the CCD camera through a coupled optical path; the CCD camera converts the optical signal into an electrical signal and a digital image of the measured object is obtained on the computer through analog-to-digital conversion. ICCD cameras not only allow for low-light enhancement, but also for high-speed imaging at nanosecond level. There is a bias voltage between the photocathode and the MCP, and by flipping this bias voltage the on/off of the electrons from the photocathode can be quickly controlled to achieve a high-speed shutter. For the ICCD camera in this dissertation, the observable wavelength ranges from 180 to 850 nm; the shortest shutter time is 2 ns； the resolution is 1024×1024; the size of a single pixel is13 μm×13 μm； the maximum frame rate is 4.2 fps, which means that for the discharges with microsecond pulses in this dissertation, the ICCD can only record one image during each breakdown. The camera is equipped with shutter monitoring signal output, which can be connected to the oscilloscope through a special cable to indicate the opening and closing instants of the camera shutter. The ICCD camera was mounted on a three-dimensional movable stage with a zoom lens, which facilitates fast focusing and clear imaging of vacuum gaps.

The voltage signal during the experiments was measured using a high-voltage probe (NorthStar PVM-7) with a maximum applicable voltage of 100 kV, an attenuation ratio of 1000:1, a bandwidth of 120 MHz, and a minimum applicable rise time of 2.5 ns. The current signal was measured using a current sensor (Pearson Model-6595) with a maximum measurable current of 1000 A, a ratio of 0.25 V/A, a bandwidth of 150 MHz, and a minimum applicable rise time of 2.5 ns. The high time resolution of both the voltage and current sensors is well suited to the measurement requirements of the experiments in this dissertation. The voltage signal, the current signal, and the shutter monitoring signal from the ICCD camera were recorded with a four-channel

oscilloscope (bandwidth 500 MHz, rise time less than 0.7 ns). The trigger timing of each device in the experiment is controlled by a digital time delay generator (SRS DG645). The delay generator has four output channels, three of which are selected to trigger the oscilloscope, the pulsed high-voltage source, and the ICCD camera, where the signal used to trigger the pulsed high-voltage source needs to be converted to an optical trigger signal that can be received by the high-voltage source through an electrical-to-optical signal converter.

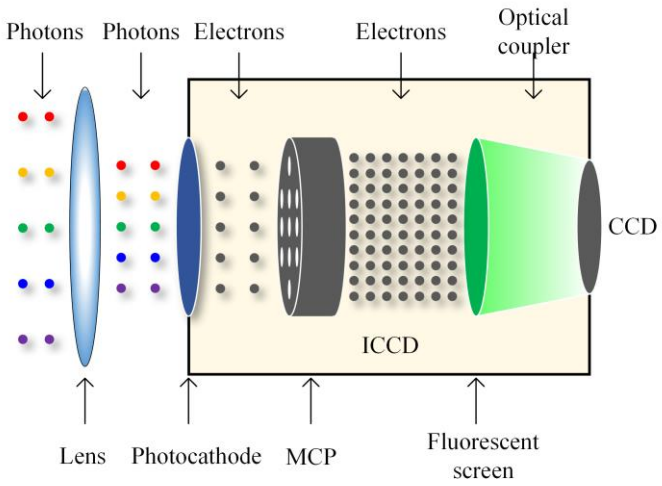

Figure 2-5 Schematic diagram of the structure and working principle of the ICCD camera

2.3 ANALYSIS OF ELECTRICAL WAVEFORMS DURING VACUUM BREAKDOWN

For the experiments in this chapter, the gap length between the cathode and the anode was in the range of 0.5-5 mm. The peak output voltage of the pulsed source is set to -40 kV, which ensures a stable triggering of vacuum breakdowns within the gap length used for the experiments. In this section, typical waveforms of voltage and current during vacuum breakdown will be given, which will be used to analyze the evolution stages of vacuum breakdown. It should be noted that the measured voltage is exactly the voltage across the gap (referred to as gap voltage, $u_g(t)$, in the following), while the measured current, denoted as $i(t)$, includes both the conduction current through the gap (referred to as gap current, $i_g(t)$, in the following) and the displacement current corresponding to the voltage variation of the gap and the voltage probe. Therefore, the gap current can be calculated by

$$i(t)=i_g(t)+i_{C2}+i_{C3} \tag{2-1}$$

where i_{C2} and i_{C3} represent the displacement current of the gap and the voltage probe repectively, and can be calculated by

$$i_{C2}=-C_2\frac{\mathrm{d}u_g(t)}{\mathrm{d}t} \tag{2-2}$$

$$i_{C3}=-C_3\frac{\mathrm{d}u_g(t)}{\mathrm{d}t} \tag{2-3}$$

where C_2 and C_3 are the capacitances of the gap and the probe. The capacitance of the probe (C_3) is 15 pF according to its manual, and the capacitance of the gap can be estimated by calculating the electric field distribution in the gap.

2.3.1 CAPACITANCE ESTIMATION OF TIP-PLANE GAP BY ELECTRIC FIELD SIMULATION

According to the characteristics of capacitive components, the capacitance (C), capacitor voltage (U) and the charge stored on the capacitor (Q) satisfy the following relationship:

$$Q=CU \tag{2-4}$$

The charge (Q) on the capacitor can be obtained by integrating the surface charge density of the metal electrodes that make up the capacitor, and the surface charge density on the metal surface, σ (in C/m^2), meets the following relationship with the electric field:

$$\sigma=\varepsilon_0\varepsilon_r E \tag{2-5}$$

where ε_0 is the vacuum permittivity (8.854×10^{-12} F/m), ε_r is the relative dielectric constant (1 for vacuum), and E is the electric field at the electrode surface (in V/m). Therefore, gap capacitance can be deduced from the electric field distribution in the gap at a given voltage.

Figure 2-6 shows the tip-plane electrode structure mounted inside the vacuum chamber with the tip electrode held by a fixture above and the plane electrode below. The model of this electrode structure is imported into COMSOL software and a vacuum domain is created around it as shown in Figure 2-7. The vacuum domain is spherical and divided into inner and outer layers. The outer spherical shell uses the Infinite Element Domain condition of COMSOL software, i.e., the outermost boundary is set to be infinitely far away to improve the accuracy of the electric field calculation. The voltage of the tip electrode is set to 0 V, while the voltage of the plane electrode is set to 1 V. The voltage at the outermost boundary is also set to 0 V. The entire region is meshed using the finite element method, and the steady state solver is used to calculate the steady state distribution of the electric field under the above boundary conditions.

Figure 2-8 shows the calculated potential distribution at a 5 mm gap, it can be seen that the maximum potential gradient (i.e. the strongest electric field) is at the surface of the tip electrode, and the potential gradually decreases with increasing distance from the center. Especially in the outer vacuum spherical shell, the potential decrease gradually shows a spherically symmetrical feature because this region is set as an infinite domain. Then, capacitance of the tip-plane gap can be calculated by integrating the electric field on the surface of the plane electrode and combining Equations (2-4)

and (2-5). As shown in Figure 2-9, the capacitance gradually decreases with the increase of the gap length, but the range of capacitance variation is not large, basically between 2.5 and 3 pF. Therefore, the gap capacitance (C_2) in the experiments can be estimated to be 3 pF.

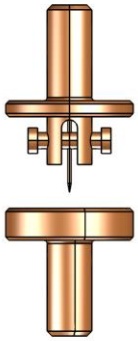

Figure 2-6 Schematic diagram of the tip-plane electrode structure installed in the vacuum chamber

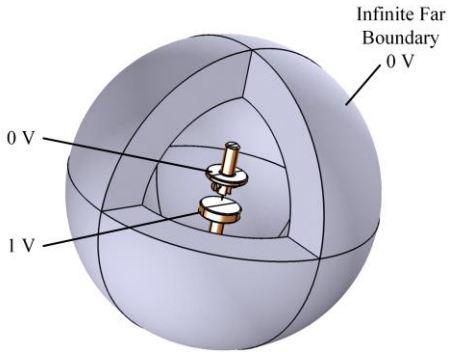

Figure 2-7 Schematic diagram of electric field simulation model of tip-plane electrode structure

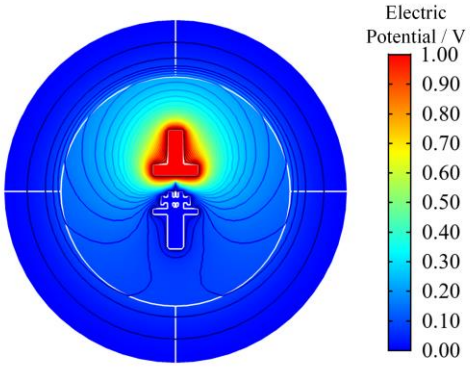

Figure 2-8 Potential distribution of a 5 mm tip-plane gap at an applied voltage of 1 V

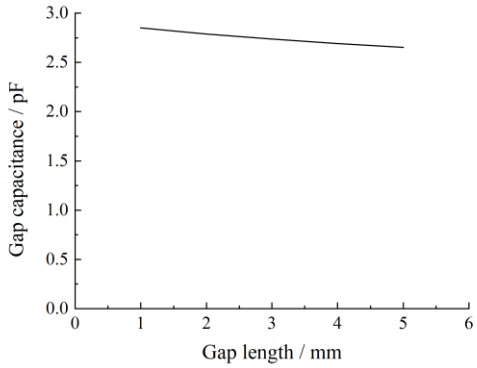

Figure 2-9 Capacitance of the plate electrode structure varies with the gap length

2.3.2 STAGES OF VACUUM BREAKDOWN EVOLUTION

Figure 2-10 shows the typical waveforms of voltage and current during vacuum breakdown. The gap length is 5 mm. The peak voltage is set to -40 kV, and the voltage pulse width is 1 μs. The horizontal axis represents time, and the vertical axes on the left and right side represent the gap voltage $u_g(t)$ and the measured current $i(t)$. Then, the displacement current is deducted from the measured current according to Equation (2-1), and the gap current $i_g(t)$ is obtaned, which is compared with the measured current in Figure 2-11. It can be seen that there is no significant difference between the two in later stage of a vacuum breakdown, which is due to the fact that the capacitance of both the gap and the high-voltage probe are relatively small and the corresponding displacement currents are much smaller than the conduction current after the breakdown begins. Before the breakdown initiation, there is no conduction current in the gap, so the gap current $i_g(t)$ is zero. The small value in the measured current is due to the charging of the gap. According to Figure 2-11, the beginning point of a vacuum breakdown can also be recognized, that is the point when the measured current $i(t)$ starts rising rapidly. This instant is defined as the time zero for the sake of convenience, and denoted as t_0 in Figure 2-10.

According to the waveforms in Figure 2-10, the entire vacuum breakdown process can be divided into four stages, represented by P0, P1, P2 and P3. The four stages are defined with four characteristic instants as separating points, including the instants when the voltage source turns on t_S, when breakdown starts t_0, when the gap voltage collapses completely t_{V0} and when the voltage source turns off t_E. The time range for P0 is t_S to t_0, during which the vacuum gap is charged by the voltage source and the gap voltage $u_g(t)$ gradually rises, so P0 is called the voltage rising stage. P1 starts at t_0 and ends at t_{V0}, in which the current continues to rise and the gap voltage gradually drops until it collapses completely (theoretically the voltage of the vacuum gap cannot be zero, but due to the presence of stray inductances, the voltage tends to cross zero when it drops, and the time when the voltage crosses zero is defined later as the instant for the complete collapse of gap voltage, t_{V0}). After P1, the vacuum breakdown enters a stable burning phase, P2. In this stage, the gap voltage remains at the level of a few tens of volts, while the current flowing through the gap (the voltage variations of the gap and the voltage probe are very small at this stage, so the measured current $i(t)$ is

almost equal to the gap current $i_g(t)$) is 80 A, which is determined by the peak voltage (-40 kV) and the current limiting resistor R_1 (500 Ω). The high current and low voltage of the vacuum gap at this stage are in accordance with the characteristics of an arc, so P2 is called the vacuum arc stage. In the vacuum arc stage (P2), the gap has a low resistance and shows the characteristics of a good conductive channel, so P1 is called the conductive channel formation stage, during which a good conductive channel was gradually built up in the previous insulated vacuum gap. Therefore, the instant t_{V0} is the instant for the formation of the conductive channel in a vacuum breakdown process. The voltage source is switched off at t_E and the vacuum breakdown enters P3. In this stage, the gap current decreases and the gap gradually regains its insulating capability, so it is called the arc extinguishing stage.

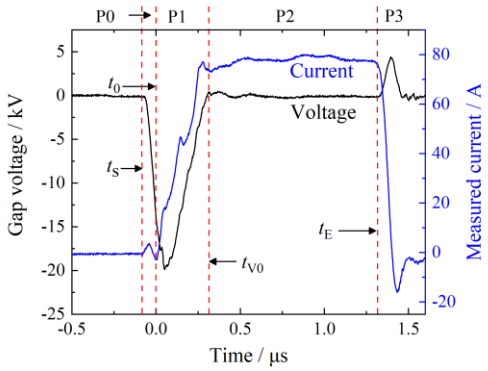

Figure 2-10 Typical voltage and current waveforms of vacuum breakdown in a 5 mm tip-plane gap

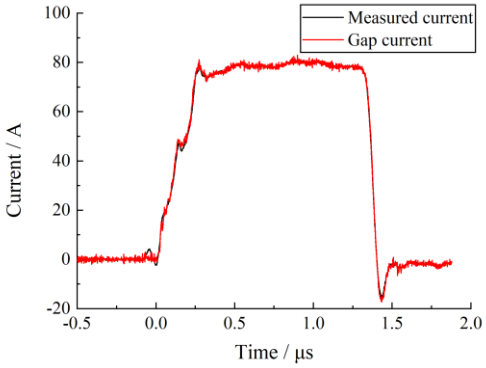

Figure 2-11 Comparison between measured current $i(t)$ and gap current $i_g(t)$

2.3.3 EFFECTS OF PULSE WIDTH AND GAP LENGTH ON STAGES OF VACUM BREAKDOWN DEVELOPMENT

2.3.3.1 Effects of voltage pulse width

Figure 2-12 and Figure 2-13 show the waveforms for gap voltage $u_g(t)$ and measured current $i(t)$ at different voltage pulse widths, respectively. To clearly show the effects of pulse width on the evolution stages of breakdown process, the waveforms for measured current which show the voltage rising stage (P0) were used in Figure 2-13. The gap length is 5 mm. The peak voltage is set to -40 kV, while the pulse width varies

between 1-5 μs. The main plots of both figures show the initial stage of vacuum breakdowns (focusing primarily on the P0 and P1), while the insets show the waveforms of the entire breakdown process. As can be seen from the figures, the vacuum breakdown processes under different pulse widths all include the four stages as stated in Figure 2-10, P0 (voltage rising), P1 (conductive channel formation), P2 (vacuum arc) and P3 (arc extinguishing). By comparison, it can be found that the change in pulse width only affects the duration of the vacuum arc stage (P2) and has no effect on the other three stages. In particular, the conductive channel formation stage (P1), which demonstrates the dynamic characteristics of vacuum breakdown, is not affected by the width of the voltage pulse.

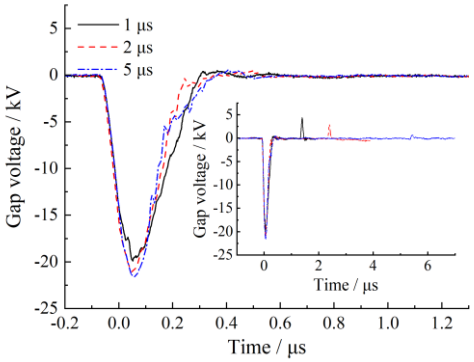

Figure 2-12 Gap voltage $u_g(t)$ waveforms of vacuum breakdowns at different voltage pulse widths

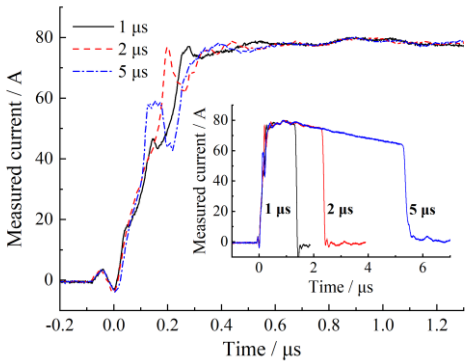

Figure 2-13 Measured current $i(t)$ waveforms of vacuum breakdowns at different voltage pulse widths

2.3.3.2 *Effects of gap length on waveforms*

Figure 2-14 and Figure 2-15 show the waveforms of the gap voltage u_g(t) and the measured current $i(t)$ during vacuum breakdowns at different gap lengths, respectively. The peak voltage and pulse width are respectively set to -40 kV and 1 μs, while the gap length varies from 0.5 mm to 5 mm. The two figures mainly cover P0 and P1 of breakdown processes, showing that both voltage and current waveforms are affected by the change of gap length. A shorter gap length leads to an earlier start of vacuum breakdown at t_0 and, accordingly, a shorter voltage rising stage (P0, t_0-t_s). In addition, the duration of the conductive channel formation stage (P1) is also extended as the gap length increases. To more accurately illustrate the effect of gap length on the duration of P0 and P1, 50 repeated experiments were conducted at each gap length and the

results were statistically analyzed as shown in Figure 2-16. The black squares in the figure represent the average duration of P0, while the red triangles represent the average duration of P1. The error bars represent the corresponding standard deviation. It is clear that the duration of the conductive channel formation stage (P1) increases significantly as the gap length increases, meaning that longer gaps take longer time to establish conductive channels, while the duration of the voltage rising stage (P0) is relatively little affected by the change of the gap length.

As can be seen in Figure 2-14, short gaps also correspond to lower gap voltage during vacuun breakdown. The breakdown voltage, U_b, of a vacuum gap can be defined as the gap voltage at t_0, i.e. $u_g(t_0)$. Through statistical analysis of the breakdown voltage under the same experimental conditions, the effect of the gap length is obtained as Figure 2-17. The data corresponding to each gap length also comes from 50 repeated experiments, with the mean and standard deviation of the breakdown voltage represented by squares and error lines, respectively. In order to reduce the effect of cathode surface conditions on the breakdown voltage, the data in Figure 2-17 were collected under the same set of tip-plane electrodes after thousands of breakdowns being performed. From the trend of breakdown voltage, it is easy to find that the breakdown voltage and the gap length are positively correlated.

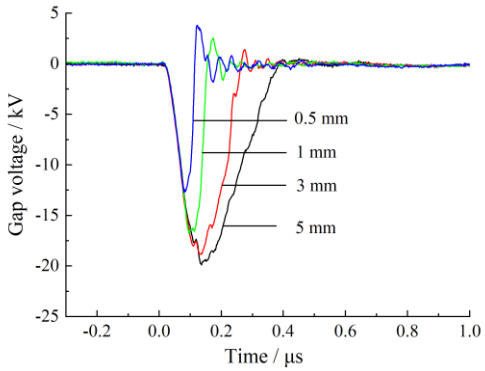

Figure 2-14 Gap voltage $u_g(t)$ waveforms of vacuum breakdowns at different gap lengths

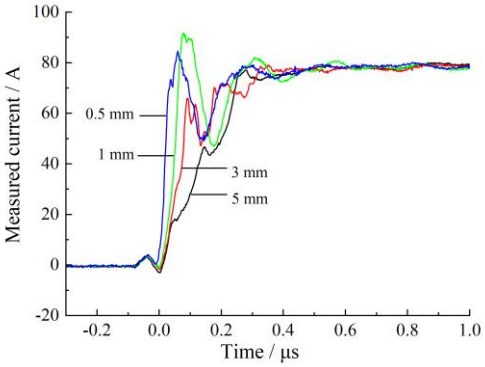

Figure 2-15 Measured current $i(t)$ waveforms of vacuum breakdowns at different gap lengths

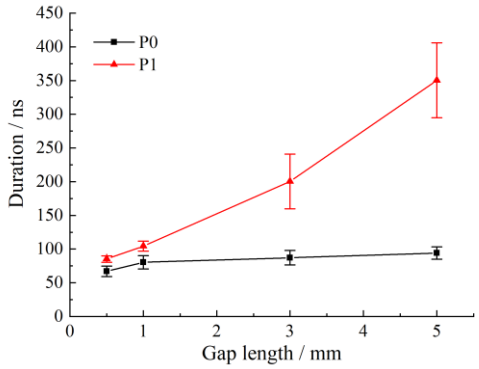

Figure 2-16 Effects of gap length on the durations of voltage rising stage (P0) and conductive channel formation stage (P1) during vacuum breakdown

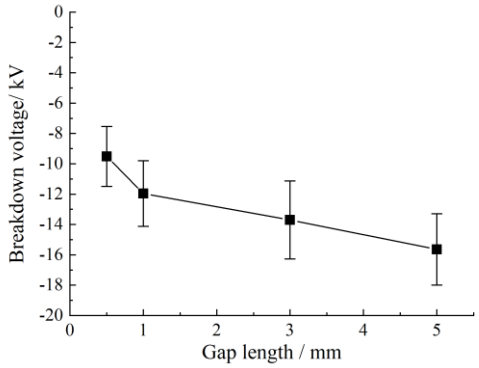

Figure 2-17 Breakdown voltage U_b for vacuum gaps with different lengths

Based on the electric field distribution in the vacuum gap obtained in Figure 2-7 and Figure 2-8, the maximum electric field appears near the tip of the cathode. In the case of an applied voltage of 1 V, the maximum electric field in vacuum gaps of different sizes, E_{1V}, is shown in Table 2-1. Combining Table 2-1 and Figure 2-17, the breakdown field, E_b (in V/m), under different gap lengths can be obtained by:

$$E_b=U_b\times E_{1V} \tag{2-6}$$

which is shown in Figure 2-18. As we see, the breakdown field is in the range of 160±30 MV/m for different vacuum gaps, which is consistent with the breakdown field for vacuum gaps between copper electrodes measured by other researchers[31, 54]. At the same time, the fact that the breakdown field does not change significantly with the gap length means that the vacuum breakdown starts after the maximum electric field at the cathode reaches a certain threshold. In other words, the electric field at the cathode surface is the key factor to determine whether vacuum breakdown occurs or not, and the vacuum breakdown is triggered at the cathode surface when the electric field reaches the breakdown threshold. This result supports the cathode-dominated breakdown theory.

Table 2-1 Maximum electric field in gaps of different lengths at an applied voltage of 1 V

Gap length/mm	5	3	1	0.5
Maximum electric field E_{1V}/V·m^{-1}	1.09×10^4	1.17×10^4	1.39×10^4	1.64×10^4

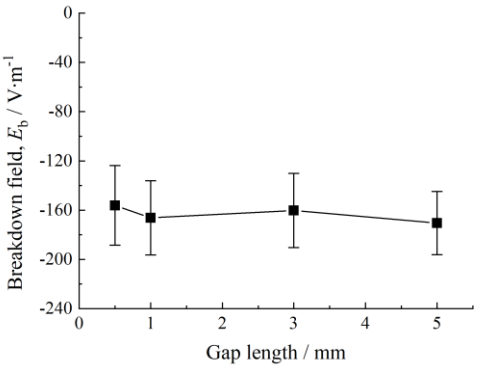

Figure 2-18 Breakdown field, E_b, for vacuum gaps of different lengths

2.4 ANALYSIS OF LIGHT RADIATION DURING VACUUM BREAKDOWN

2.4.1 SPATIO-TEMPORAL EVOLUTION OF LIGHT RADIATION

The light radiation during vacuum breakdown is observed by using an ICCD camera. According to Figure 2-16, the conductive channel formation stage (P1) lasts only tens to hundreds of nanoseconds. Therefore, in order to clearly distinguish the evolution of light radiation, the exposure time of the ICCD camera must be at a nanosecond scale. In addition, as mentioned in Section 2.2 when describing the ICCD camera, the maximum frame rate of the camera is only 4.2 fps, which means that the camera cannot output more than 5 images per second to the computer. Therefore, the ICCD camera can only take one image per vacuum breakdown (microsecond voltage pulse), and the observation of the whole process of vacuum breakdown requires repeating breakdown experiments under the same conditions and gradually adjusting the delay of the camera shutter with respect to the breakdown process. Figure 2-19 is a schematic diagram of timing setup for ICCD camera and breakdown process. The black waveform is a typical current waveform of a vacuum breakdown, and the red waveform is the shutter monitoring signal of the ICCD camera. The pulsed high-voltage source and the ICCD camera are triggered by two signals generated by the digital delay generator (SRS DG645), with the shutter monitoring signal of the camera and the current signal of breakdown connected to the oscilloscope at the same time. As shown in the figure, the vacuum breakdown starts at t_0, while the camera shutter opens at t_1 (generating a downward pulse). The delay between t_0 and t_1 is called the shutter delay of the camera, Δt, which can be adjusted by changing the delay between the two triggering signals. However, the starting instant of vacuum breakdown, t_0, may change due to the jitter of the breakdown voltage, so the shutter delay of the camera should be determined based on the oscillograms. After the shutter opens for the exposure time, t_w, the shutter will close at t_2, generating an upward pulse signal. During the experiment procedure, the light radiation at each stage of vacuum breakdown were observed with nanosecond exposure times by gradually changing the shutter delay Δt of the camera.

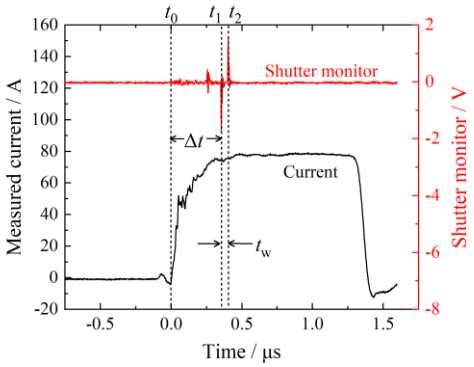

Figure 2-19 Schematic diagram of timing setup for ICCD camera and breakdown process

By combining the light radiation images obtained under different shutter delays, the light radiation evolution of the whole vacuum breakdown process can be reconstructed, with a temporal resolution of nanosecond scale. However, due to the frame rate limitation of the ICCD camera, each image comes from a different breakdown process. Therefore, the reconstruction of the images has a premise that the vacuum breakdown process under the same experimental condition is stable and repeatable. Figure 2-20 and Figure 2-21 show voltage and cuurent waveforms of three vacuum breakdowns under the same experimental conditions, respectively. The gap length is 5 mm. The peak value and pulse width of the voltage are -40 kV and 1 μs, respectively. By comparing the results of the three breakdowns, it can be found that the waveforms of each breakdown vary slightly, but the overall trend of the waveforms and the duration of the evolution stages are quite stable.

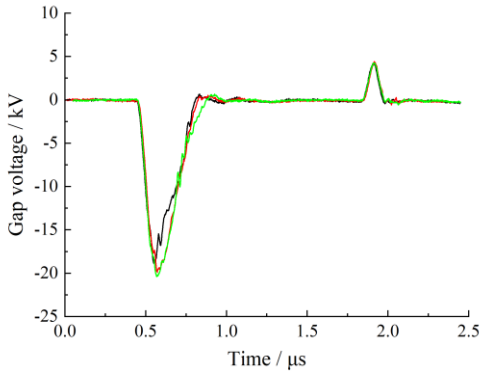

Figure 2-20 Gap voltage $u_g(t)$ waveforms of three breakdowns under the same conditions

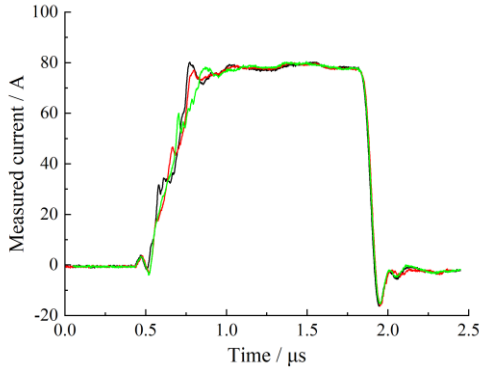

Figure 2-21 Measured current $i(t)$ waveforms of three breakdowns under the same conditions

Figure 2-22 shows the light radiation images of the three vacuum breakdowns recorded with the ICCD camera. In order to record the light radiation from the entire breakdown process, the exposure time of the camera is set to 7 μs and the breakdown process occurs when the camera shutter is opened at 3 μs. The needle cathode and the plate anode are at the top and bottom of the image, respectively, and the outlines of the electrodes are marked with white dashed lines. It can be seen that the light radiation is stronger near the electrodes and weaker in the center of the gap. The light-emitting area near the cathode is small with high intensity, while that near the anode is large with lower intensity. The distribution of light radiation in the three images is similar. Therefore, the vacuum breakdown process under the same experimental condition has good repeatability and stability, from both the viewpoints of electrical signal and light radiation. Then, the above-mentioned method for reconstructing the light radiation evolution by images of multiple breakdown experiments is feasible and effective.

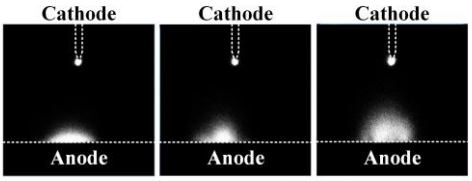

Figure 2-22 Light radiation images of three vacuum breakdowns under the same conditions

Figure 2-23 shows the spatio-temporal evolution of light radiation during vacuum breakdown. Vacuum breakdown in the figures takes place within a gap of 5 mm, and the corresponding voltage and current waveforms are shown above the sequence of images. The peak voltage and pulse width were set as -40 kV and 5 μs, respectively. The tip cathode and plane anode are located at the top and bottom of the images, with the outlines indicated by white dashed lines. The two numbers below each image represent the shutter delay Δt and the exposure time t_w of the camera, i.e. these images cover the entire breakdown event with a uniform exposure time of 50 ns. By observing the images, it is found that the evolution of light radiation during vacuum breakdown can be divided into three main stages. As can be seen from the first image, light radiation appears near the cathode immediately after the vacuum breakdown begins, starting the first stage of the light radiation evolution. During this stage, light radiation exists only near the tip of the cathode, while there is no luminescence near the anode surface. The fisrt evolution stage lasts for 250 ns, i.e. the first five frames of Figure 2-23, during which the intensity of light radiation near the cathode (hereinafter referred to as the cathode glow) increases gradually. At 250 ns (frame 6), a faint light radiation appears near the anode surface, and the second stage begins with the presence of light radiation near both electrodes. At this stage, light radiation originating from the anode surface (hereinafter referred to as the anode glow) gradually expands toward the cathode and bridges the gap after 2000 ns (frame 14 in Figure 2-23) to form a light-radiation channel. In contrast, the cathode glow did not expand significantly during this stage. After 2000 ns, the evolution of light radiation enters its final stage, in which the light radiation near the anode surface and in the middle of the gap begins to decay and eventually disappears from the gap. However, cathode glow maintains until the gap current goes down completely. Since then, the ICCD has not recorded any

radiation from the gap. Thus, the light radiation accompanies the whole process of vacuum breakdown, with the cathode glow always present and the anode glow only present during part of the process. In short, the three main stages of vacuum breakdown can be defined based on the light radiation evolution, which are cathode glow stage, anode glow expanding stage and anode glow decay stage.

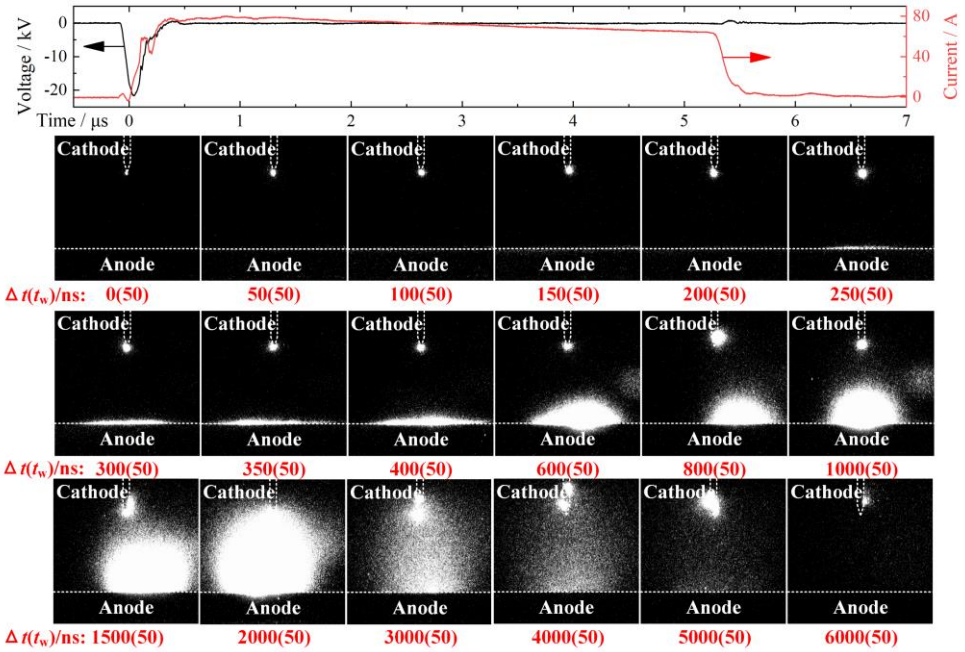

Figure 2-23 Spatio-temporal evolution of light radiation during vacuum breakdown (5 mm gap)

Figure 2-24 and Figure 2-25 show the light emission evolution in 3 mm gap and 1 mm gap. It can be seen that the light-radiation evolution is similar in vacuum gaps of different lengths when breakdown occurs, all containing the three stages mentioned above. The differences between them are the instants for the appearance of the anode glow and the formation of the light-radiation channel (i.e., the instant the expanding anode glow reaches the cathode), which are compared in Table 2-2.

As can be seen from Table 2-2, as the gap length decreases, both the appearance of anode glow and the formation of light-radiation channel happen earlier. This shortens the duration of the cathode glow stage and the anode glow expanding stage accordingly, while the anode glow decay stage is extended (the duration of the entire breakdown process equals to the voltage pulse width, unchanged). In fact, the decay of the anode glow does not necessarily continue throughout the last stage of the light radiation evolution. According to Figure 2-25, the light emission near the anode and in the gap has almost disappeared by 2000 ns, while only the cathode glow remains for the breakdown process after 2000 ns. This means that anode glow is not a necessary condition for maitaining the vacuum arc. In addition, by observing the anode glow in three different gap lengths, it can be found that when the anode glow first appeared, the spot size at the anode surface was close to the gap length, 5.7 mm, 3.4mm and 1.13 mm, respectively.

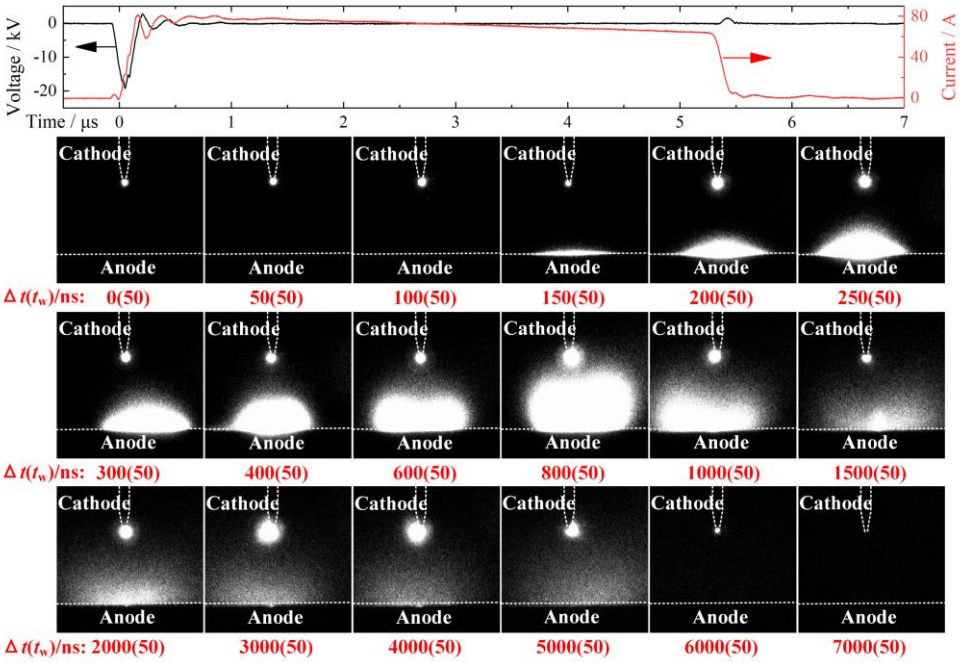

Figure 2-24 Spatio-temporal evolution of light radiation during vacuum breakdown (3 mm gap)

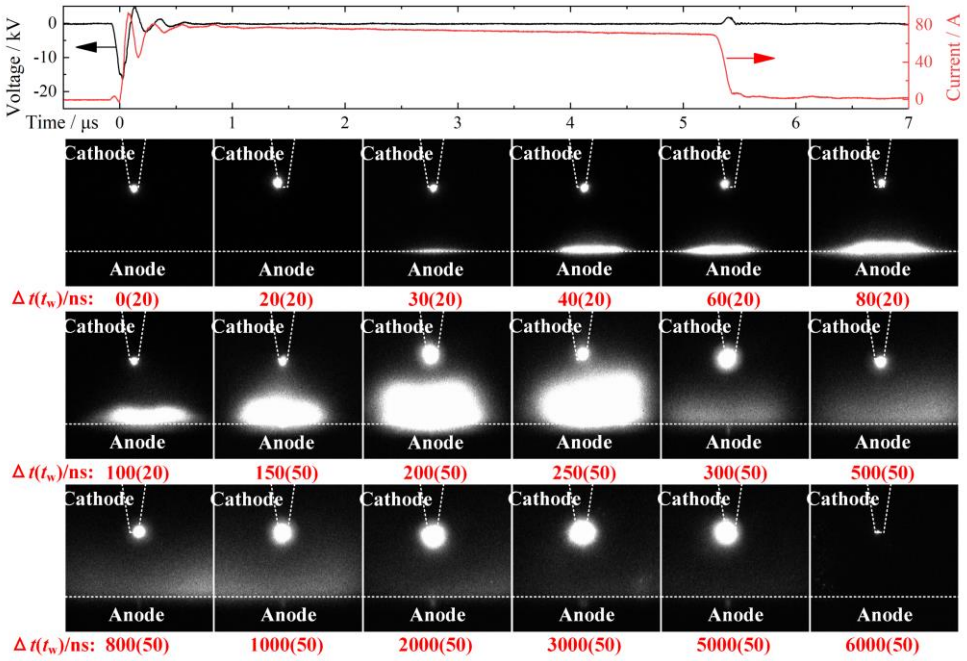

Figure 2-25 Spatio-temporal evolution of light radiation during vacuum breakdown (1 mm gap)

Table 2-2 Comparison of the instants of anode glow appearance and light-radiation channel formation for breakdowns in vacuum gaps of different lengths

Gap length/mm	Anode glow appearrance / ns	Light-radiation channel formation /ns
5	250	2050
3	150	850
1	40	300
0.5	10-20	150

2.4.2 INTENSITY DISTRIBUTION OF LIGHT RADIATION DURING VACUUM BREAKDOWN

In section 2.4.1, the spatio-temporal evolution of light radiation during vacuum breakdown was analyzed by ICCD camera. However, in order to clearly determine the spatial distribution of the light radiation, the contrast of the images is adjusted in Figure 2-23 to Figure 2-25, resulting in a loss of accurate light intensity information. In this section, the intensity distribution of the light radiation during breakdown is analyzed.

First, the field of view of the camera is adjusted to include only the cathode, and the light intensity distribution of the cathode glow is observed. Figure 2-26 is a typical distribution of the intensity of cathode glow in the process of vacuum breakdown, the unit of light intensity in the figure is dimensionless, indicating only the relative intensity of light radiation. The vacuum breakdown corresponding to this image occurs in a 5 mm gap, with peak voltage and pulse width being -40 kV and 5 μs, respectively. The exposure time of the ICCD camera is set to 7 μs to ensure that all the radiation of the cathode glow is collected throughout the breakdown process. As in the figure, the cathode glow is a highly concentrated spherical light radiation with the center intensity two orders of magnitude higher than the intensity of the surrounding area. The peak intensity of the cathode glow occurs near the tip of the cathode needle.

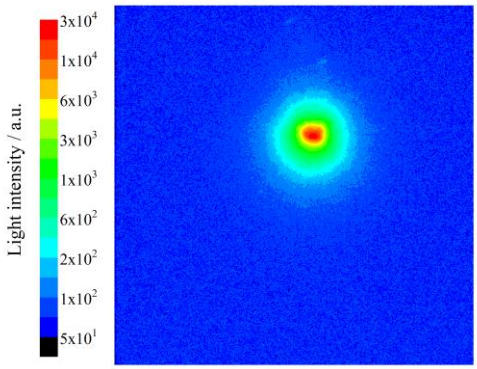

Figure 2-26 Typical intensity distribution of cathode glow during vacuum breakdown

Figure 2-27 and Figure 2-28 show, respectively, the peak and integrated light intensity of the cathode glow during vacuum breakdown under different experimental conditions. The gap length varies from 0.5 mm to 5 mm, and the voltage pulse width varies among 1 μs, 2 μs and 5 μs, while the peak voltage remains at -40 kV. The exposure times of the ICCD camera was all set to 7 μs, so each image taken (similar to Figure 2-26) contains the time integral of the cathode glow over the entire breakdown process. The peak intensity shown in Figure 2-27 refers to the peak in the spatial distribution, i.e. the center of the cathode glow in Figure 2-26. The integrated intensity in Figure 2-28 is the spatial integration of the light intensity distribution, i.e., the sum of the light intensities of all pixels of the light intensity distribution plot (similar to Figure 2-26). The experiment was repeated 10 times for each condition, and then the corresponding mean and standard deviation were calculated and represented by the height and error bars in the bar graph, respectively. As shown in the figure, the gap length has little effect on the peak and integrated intensity of cathode

glow at the same voltage pulse width. In contrast, increasing the voltage pulse width causes a significant increase in the peak and integratd intensity of the cathode glow. As the voltage pulse width increases, the integrated intensity increases almost linearly, while the peak intenstiy growth rate is relatively small. For example, when the voltage pulse width increases from 1 μs to 5 μs, the integrated intensity increases five times, while the peak intensity increases only three times. Based on this result, it can be inferred that: first, the light radiation from the cathode glow region in the vacuum breakdown process is basically unchanged; second, the cathode glow has a certain extent of expansion in the breakdown process, making the peak light intensity increase slower than the gap length.

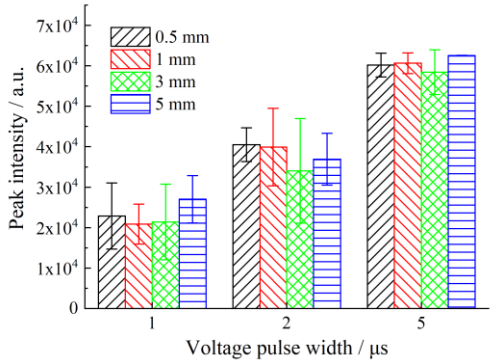

Figure 2-27 Peak intensity of cathode glow during vacuum breakdown under different conditions

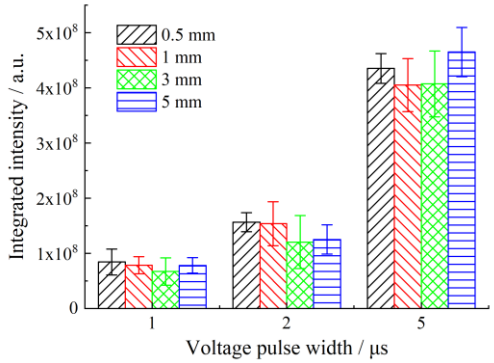

Figure 2-28 Integrated intensity of cathode glow during vacuum breakdown under different conditions

After understanding the light intensity distribution of cathode glow, the field of view of the ICCD camera is adjusted to be able to record the entire vacuum gap, and the distribution of light radiation intensity along the gap axis is analyzed. The peak and pulse width of the applied voltage are set to -40 kV and 5 μs, respectively. The exposure time is still set to 7 μs to collect the light radiation throughout the whole breakdown process. After each breakdown experiment, the camera outputs an image similar to Figure 2-22, where both cathode glow and anode glow are present. The obtained images were processed as follows:

(1) Integrating the light intensity of each pixel along the horizontal direction of the image (i.e., parallel to the anode surface) to obtain the distribution of light intensity along the vertical direction (i.e., the gap axis);

(2) Normalizing the light intensity distribution along the gap with the peak value in the cathode glow region as the reference;

(3) Normalizing the spatial position of the gap using the spatial position of the cathode and anode as reference points;

(4) Repeating the experiment ten times under the same conditions to obtain the average distribution of light intensity.

After the above processing of images, the intensity distribution of light radiation along the gap in vacuum breakdowns can be obtained for different gap lengths, as shown in Figure 2-29. The horizontal axis in the figure represents the relative position along the gap, with 0 and 1 indicating the anode surface and the tip of the cathode. The vertical axis in the figure represents the normalized light intensity. As shown in the figure, the intensity of cathode glow is much higher than that of anode glow, because the peak intensity and duration of cathode glow are both larger than anode glow. Comparing the results of different gaps, it can be found that the intensity of anode glow increases with the gap length. This can be qualitatively explained from the point of view of energy conservation. As the gap size increases, the time required to form the conductive channel increases, as well as the time during which the gap voltage keeps high. As a result, the energy provided by the external circuit to the gap increases. Since the intensity of cathode glow does not change with the size of the gap (see Figure 2-27 and Figure 2-28), the increment in the input energy into the gap will partially be consumed by the the anode glow, resulting in an increase in the total intensity of the anode glow.

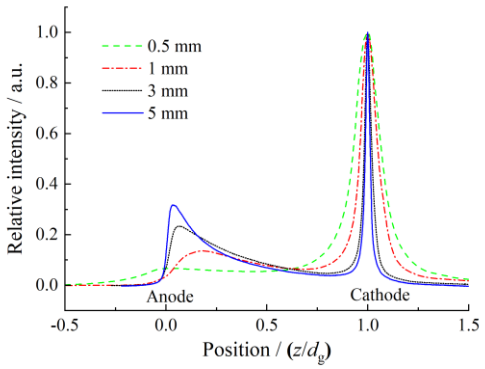

Figure 2-29 Intensity distribution of light radiation along the gap in vacuum breakdown process

Table 2-3 shows the statistical results of the FWHM (full width at half maximum) of the intensity distribution curve near the cathode in Figure 2-29. The second and third columns of the table are the mean and standard deviation of the ten results, respectively. According to table, the FWHM of the cathode glow region is not greatly affected by the gap size, which remains to be at about 0.1 mm. This also implies the stability of the cathode glow in vacuum breakdown processes. As long as the gap current remains unchanged, the glow near the cathode and the physical process behind it are fairly stable.

Table 2-3 FWHM of the intensity distribution curve near the cathode in Figure 2-29

Gap length/mm	FWHM	
	Mean value	Standard deviation
5	0.112	0.011
3	0.115	0.022
1	0.102	0.022
0.5	0.094	0.019

2.5 COMPARATIVE ANALYSIS OF ELECTRICAL SIGNALS AND LIGHT RADIATION DURING VACUUM BREAKDOWN

2.5.1 APPEARANCE OF CATHODE GLOW AND FORMATION OF CATHODE PLASMA

As can be seen from section 2.4.1, the cathode glow appears immediately after the vacuum breakdown begins (t_0) and is present in the entire process of vacuum breakdown. It is well known that in a vacuum gap with applied voltage, electrons will be emitted from the cathode surface due to the effect of the electric field, i.e. field electron emission. The current formed by electron emission inside the cathode heats the cathode tip, and the increase in cathode temperature may enhance electron emission and lead to evaporation of metal atoms, which may eventually produce a plasma near the cathode through collisional ionization of electrons and atoms. Therefore, there are two possible mechanisms to the generation of the cathode glow: one is the radiation produced by the cathode itself at high temperature, and the other is the light radiation produced by plasma formed near the cathode. If the cathode glow appears under the first mechanism, it means that there is only an electron emission process at the cathode surface, and the plasma is not produced. In the case of pure electron emission, the emission current is limited by the space charge effect[44]. With the increase of electron emission, the emitted electrons can accumulate near the emitting surface and form a space charge layer. This space charge layer shields the applied electric field and limits the emission current by creating a negative feedback near the emitting surface. The maximum current density of electron emission at the cathode surface depends on the local electric field and the total applied voltage, as expressed by the Child-Langmuir equation as follows:

$$J_c=\frac{4}{9B}\frac{F^2}{U^{1/2}},\ B=\frac{m_e^{1/2}}{\varepsilon_0(2e)^{1/2}} \tag{2-7}$$

where J_c is the maximum current density of electron emission at the cathode surface (in A/m^2); F is the local electric field (in V/m); U is the total applied voltage (in V); m_e is the electron mass (9.1×10^{-31} kg); ε_0 is the vacuum permittivity (8.854×10^{-12} F/m); e is the elementary charge (1.6×10^{-19} C).

Then the electron emission current density at each point on the cathode surface can be calculated by Equation (2-7). According to the characteristics of metals, at each point p on the cathode surface, the direction of the electric field is perpendicular to the surface, and the area element around point p can be treated as a tiny flat electrode, so that the electron emission current density on each area element can be calculated by using Equation (2-7) as follows:

$$J_c(p)=\frac{4}{9B}\frac{F(p)^2}{U^{1/2}} \tag{2-8}$$

the local electric field at each point is proportional to the total voltage of the gap,

$$F(p)=R(p)U \tag{2-9}$$

where $R(p)$ is the ratio of the electric field to the voltage (in 1/m), i.e. the electric field corresponding to an applied voltage of 1 V. Therefore, the equation (2-8) can be rewritten as

$$J_c(p)=\frac{4}{9B}R(p)^2U^{3/2} \tag{2-10}$$

Thus, considering the limitation of space charge effect, the maximum electron emission current I_c over the entire cathode surface can be obtained by area integration over the individual area elements as follows:

$$I_c=\int_S J_c\mathrm{d}A=\frac{4}{9B}U^{3/2}\int_S R(p)^2\mathrm{d}A=\frac{4}{9B}U^{3/2}H \tag{2-11}$$

where H is the integral of the square of $R(p)$ over the cathode surface, and this value is a dimensionless quantity whose magnitude depends on the distribution of the electric field. In the above equation, the direction of the current density is considered to be perpendicular to the local cathode surface, so the current value given in Equation (2-11) is a scalar, and H represents exactly the effect of the electrode geometry on the electron emission. Intuitively, if the calculated electrode system is a pair of flat electrodes, then $H = A/d^2$, where A denotes the area of the entire cathode and d denotes the gap length.

According to the electric field distribution of the tip-plane electrode structure shown in Figure 2-8 for the case of 1 V applied voltage, the maximum value of $R(p)$ over the cathode surface can be obtained and the value of H is calculated by integration, as shown in Table 2-4. Then, the maximum electron current I_c that can be emitted from the cathode surface under the limitation of space charge effect can be calculated using Equation (2-11). Figure 2-30 gives a comparison between the maximum electron emission current I_c and the experimentally measured gap current $i_g(t)$ for a 5 mm vacuum gap as an example. The waveforms in the figure are from the same breakdown as in Figure 2-10. The black curve in the figure represents the gap voltage, corresponding to the left vertical axis, while the red and blue curves represent the maximum electron emission current I_c calculated by Equation (2-11) and the experimentally measured gap current $i_g(t)$, respectively, corresponding to the right

vertical axis. It is clear that the experimentally measured current $i_g(t)$ exceeds the current upper limit I_c corresponding to pure electron emission shortly after the vacuum breakdown begins (t_0). The same phenomenon is observed for the other gap lengths covered in this chapter, 0.5 mm, 1 mm and 3 mm. This means that the gap current measured during the vacuum breakdown is not provided by the pure electron emission of the cathode. In other words, a more intense discharge process is initiated around the cathode, which allows the discharge current to exceed the limits of the space charge effect. In fact, soon after the start of vacuum breakdown, plasma forms around the cathode, and the presence of this plasma counteracts the space charge effect of pure electron emission, thus making the gap current of the breakdown process much larger than the upper limit of the pure electron emission.

Table 2-4 Maximum value of $R(p)$ and the integral of $R(p)^2$ over the cathode surface H for different vacuum gaps at an externally applied voltage of 1 V

Gap length / mm	$R(p)$ the maximum value on the cathode surface / m^{-1}	$R(p)^2$ integral H on the cathode surface
5	1.09×10^4	2.25
3	1.17×10^4	2.65
1	1.39×10^4	3.71
0.5	1.64×10^4	5.16

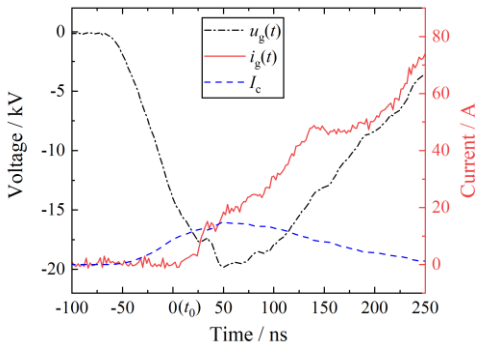

Figure 2-30 Variation of gap voltage $u_g(t)$, gap current $i_g(t)$ and maximum electron emission current I_c with time during vacuum breakdown

Based on the above discussion, it can be proven that cathode glow is not the black body radiation produced by the high temperature of the cathode itself, but the light radiation produced by the interaction of particles in the plasma around the cathode. Thus, immediately after the vacuum breakdown begins, the plasma (hereafter referred to as the cathode plasma) is established around the cathode, which is present throughout the vacuum breakdown process and constantly radiates outwards. The electrons and ions in cathode plasma will also expand to the anode under the action of electric field and density gradient, contributing to the improvement of gap conductivity.

Compared to the cathode glow, the anode glow does not last throughout the whole process of vacuum breakdown (see Figure 2-23, Figure 2-24 and Figure 2-25), it may disappear when the breakdown is in the vacuum arc stage (P2), meaning that the anode glow is not a necessary condition to maintain the vacuum arc.

In addition, the anode glow appears always after the cathode glow, and the delay is

positively correlated with gap length (see Table 2-2), which implies that the anode glow is not an independent process, but a secondary effect that depends on a certain premise or condition. The whole process of vacuum breakdown is accompanied by the generation of cathode plasma, and the current of the breakdown is mainly carried by the movement of the cathode-emitting electrons to the anode, so it can be inferred that the anode glow is the result of the movement of charged particles of the cathode plasma to the anode and/or the corresponding secondary effects.

2.5.2 RELATIONSHIP BETWEEN ESTABLISHEMENT OF LIGHT-RADIATION CHANNEL AND CONDUCTIVE CHANNEL

As can be seen from Figure 2-23 to Figure 2-25, the anode glow reaches the cathode surface after a period of expansion, creating a light-radiation channel connecting the gap. To analyze the relationship between the establishment of the light-radiation channel and the conductive channel, the instants for their occurrence were compared in Table 2-5. The instant of conductive channel formation is the instant when the gap voltage drops to zero and the vacuum breakdown enters the vacuum arc stage (t_{V0}), as discussed in Section 2.3. By comparing these two columns, it can be found that the formation of conductive channels is much earlier than that of the light-radiation channels. In addition, according to the instant of the appearance of the anode glow in the first column of Table 2-2, it can also be found that the conductive channel was formed shortly after the appearance of the anode glow, and most of the vacuum gap was still in darkness at that time (see frame 8 of Figure 2-23, frame 5 of Figure 2-24 and frame 7 of Figure 2-25). Therefore, it can be inferred that the expansion of anode glow does not have a major contribution to the formation of conductive channels in vacuum breakdowns. This discovery clarifies the non-necessity of the expansion of anode glow and the establishment of light-radiation channels in forming conductive channels. The subsequent chapters of this dissertation are more in-depth studies based on this discovery, with the aim of gaining a clear understanding of the physical processes involved in the construction of conductive channel in vacuum breakdown.

Table 2-5 Comparison of the formation instants of light-radiation channels and conductive channels in vacuum breakdown processes

Gap length/mm	Light-radiation channel / ns	Conductive channel / ns
5	2050	350
3	850	200
1	300	110
0.5	150	85

2.6 ELECTRODE MORPHOLOGY BEFORE AND AFTER VACUUM BREAKDOWN

Since vacuum arc is maintained by metal vapor supplied by metal electrodes, there

should be some changes on the electrode surfaces after the vacuum breakdown processes. The microscopic surface morphology of the cathode and the anode before and after breakdowns was observed and analyzed by SEM (Scanning Electron Microscope, Hitachi S-3000N).

2.6.1 MORPHOLOGICAL CHANGES OF THE CATHODE SURFACE

Figure 2-31 shows the microscopic surface condition of the cathode prior to breakdown experiments. Figure 2-31(a) and (b) corrspond to magnifications of 80x and 1000x, respectively, and clear machining traces can be seen on the surface of the tip cathode. The cone angle of the electrode is about 15°, and the top diameter of the tip is about 60 μm.

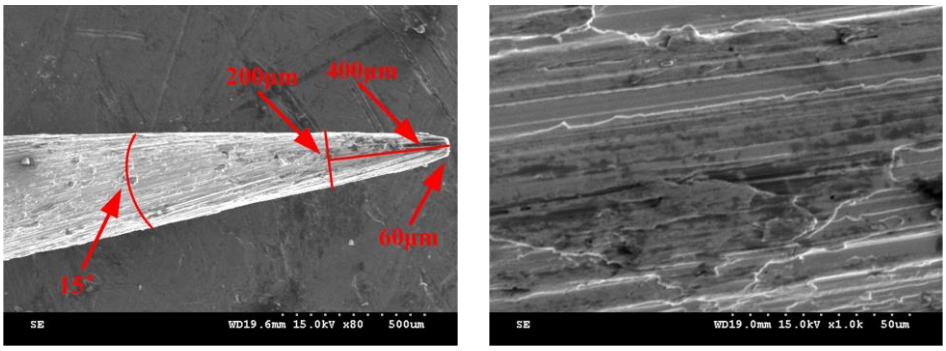

(a) 80 magnification (b) 1000 magnification

Figure 2-31 Cathode surface before breakdown experiments

Figure 2-32 shows the surface morphology of the cathode after 1000 breakdowns. Figure 2-32 from (a) to (d) show the resulting cathode tips after the experiments with gap lengths of 5 mm, 3 mm, 1 mm and 0.5 mm, respectively, which do not differ significantly. Comparing the cathode surface before and after breakdowns, the following changes can be seen: first, the cathode surface exhibits a large molten area, and the machining traces before the experiments mostly disappear; second, the shape of the top of the tip, instead of a sharp-edged round flat, become a hemisphere with a diameter of about 200-250 μm. From the comparison with Figure 2-31 it can be deduced that the tip of the cathode has shortened by about 300 μm. The above two changes suggest that the cathode surface is severely ablated during vacuum breakdown and there is some material loss, which is the result of the interaction between the cathode plasma and the cathode surface. It is also the material loss of the cathode that makes the development of vacuum breakdown and the maintenance of the vacuum arc possible.

A closer look at each SEM image in Figure 2-32 reveals that there is some variation in the degree of ablation in different parts of the cathode. From the tip toward the root of the needle, the degree of surface melting seems to be gradually decreasing. In order to observe the ablation at different locations on the cathode surface more clearly, the magnification of the electron microscope was set to 1000x, and the microscopic morphology of the local areas at the head (point A), middle (point B) and tail (point C) of the cathode in Figure 2-32(a) were observed, as shown in Figure 2-33. As can

be seen from the figure, the ablation at points B and C is actually a stacking of several craters on top of each other on the cathode surface, and the characteristic sizes of the craters in Figure 2-33(b) and (c) are about 50 μm and 3 μm, respectively. The intensity of ablation at point A shown in figure (a) is significantly stronger than points B and C, making it impossible to see a clear crater boundary in figure (a). In addition, traces of machining on the cathode surface prior to the breakdown experiment can be seen in some areas of figure (c). Therefore, during the vacuum breakdown in tip-plane gaps, the intensity of ablation on the cathode surface decreases gradually from the tip of the needle to its root. This indicates that cathode plasma is concentrated at the tip end of the cathode.

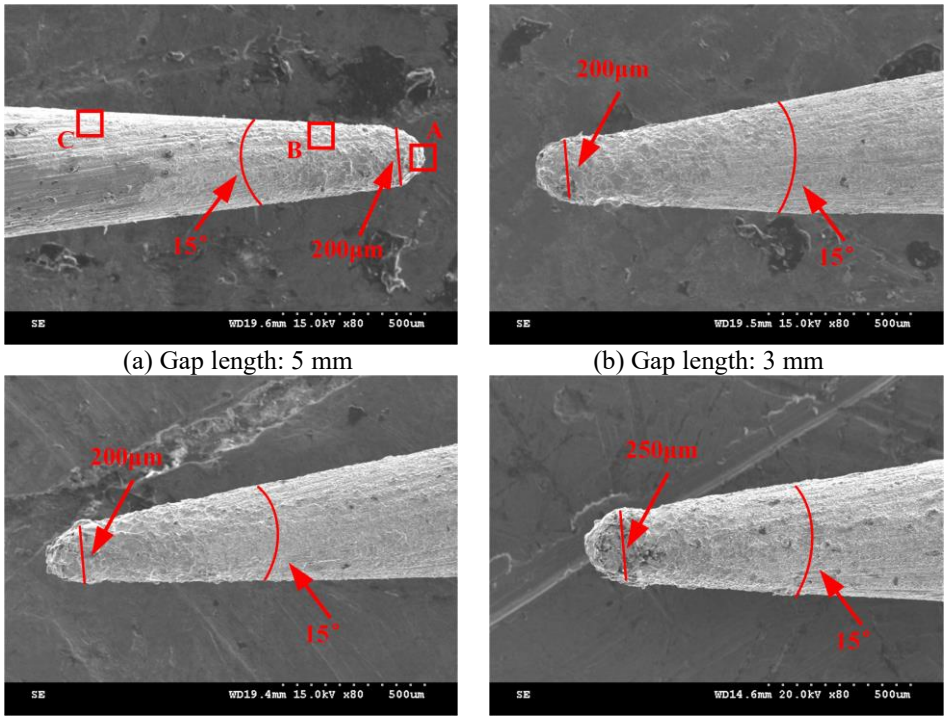

(a) Gap length: 5 mm (b) Gap length: 3 mm

(c) Gap length: 1 mm (d) Gap length: 0.5 mm

Figure 2-32 Cathode surface after 1000 times of breakdown experiments (80x)

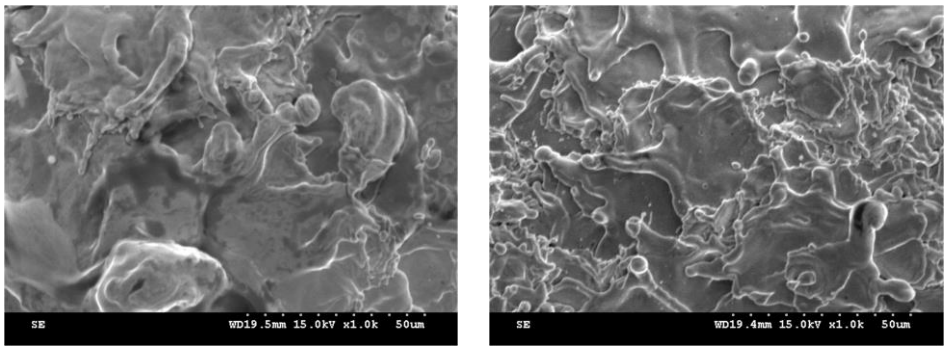

(a) A-head (b) B-middle

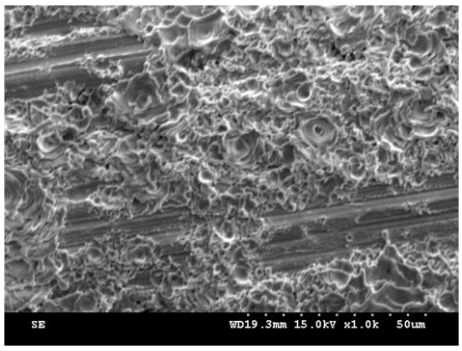

(c) C-tail

Figure 2-33 Local magnification of Figure 2-32(a) (1000x)

2.6.2 MORPHOLOGICAL CHANGES OF THE ANODE SURFACE

Since the anode surface is much larger than the cathode, the SEM cannot observe the entire anode surface at once even at minimal magnification. Therefore, the entire anode surface before and after breakdown experiments was first observed by an optical microscope, and then the area with significant changes was analyzed using SEM.

Figure 2-34 shows the anode surface before breakdown experiments, figures (a) and (b) are the entire anode surface obtained by the optical microscope and the local anode surface obtained by the SEM, respectively, where the anode surface is the surface of the replaceable anode plate in Figure 2-4(b). It can be found that the anode surface was very flat, with only some very small traces of machining.

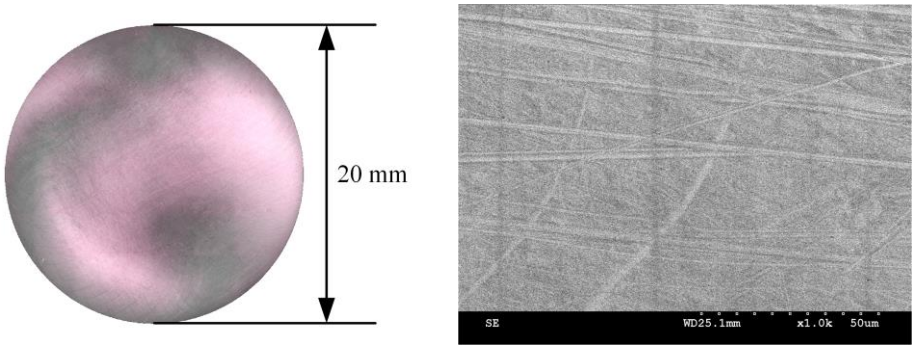

(a) Optical microscope View (b) SEM view

Figure 2-34 Anode surface condition before breakdown experiments

After 1000 breakdowns, the entire surface of anode was observed again by the optical microscope, as shown in Figure 2-35. Figure 2-35(a) is the result from a 5 mm gap, showing no significant change in surface condition, and Figure 2-35(b)-(d) corresponds to gaps of 3 mm, 1 mm and 0.5 mm, respectively, where a spot with a diameter of about 3 mm can be seen near the center of the anode surface.

To see more clearly the changes of the anode surface, the spot areas were magnified by the SEM, and the results are shown in Figure 2-36. Since the optical microscope does not observe significant changes in the anode surface when the gap length is 5 mm, Figure 2-36(a) is a typical result of the area near the surface center of Figure 2-35(a). In Figure 2-36(a)-(d), micron-sized spherical particles can be easily recognized on the anode surface, which are concentrated in the area near the center of

the anode surface, i.e. the spot area in Figure 2-35. With the decrease of the gap length, the density of these spherical particles on the anode surface shows an increasing trend. These spherical particles are the result of the migration of the molten droplets from the cathode to the anode during the breakdown process, and a specific verification will be given in the next chapter. In addition, looking closely at the individual images in Figure 2-36, the traces left by the machining process on the anode surface are still clearly present. Even in the cases with the most severe morphological changes (0.5 mm gap), machining traces can still be easily found. The very small traces on the anode surface (depths not exceeding a few microns, see Figure 2-34(b)), indicating that the vacuum breakdown process did not cause significant melting of the anode surface under the experimental conditions in this chapter. It can be further speculated that evaporation on the anode surface will not be particularly significant either. Under such conditions, it is unlikely that a high-temperature, high-density plasma will form near the anode surface, and the contribution of the anode to the formation of the conductive channel during breakdown will also be small. However, the formation of the conducting channel in the vacuum gap must be based on the premise that the plasma connects the entire gap. Therefore, although the cathode glow region does not expand significantly during vacuum breakdown, the formation of the conducting channel is probably the result of cathode plasma expansion. As to whether there is a cathode plasma expansion process in the dark gap and how the anode glow is formed without a high anode temperature will be discussed in more detail in the subsequent chapters.

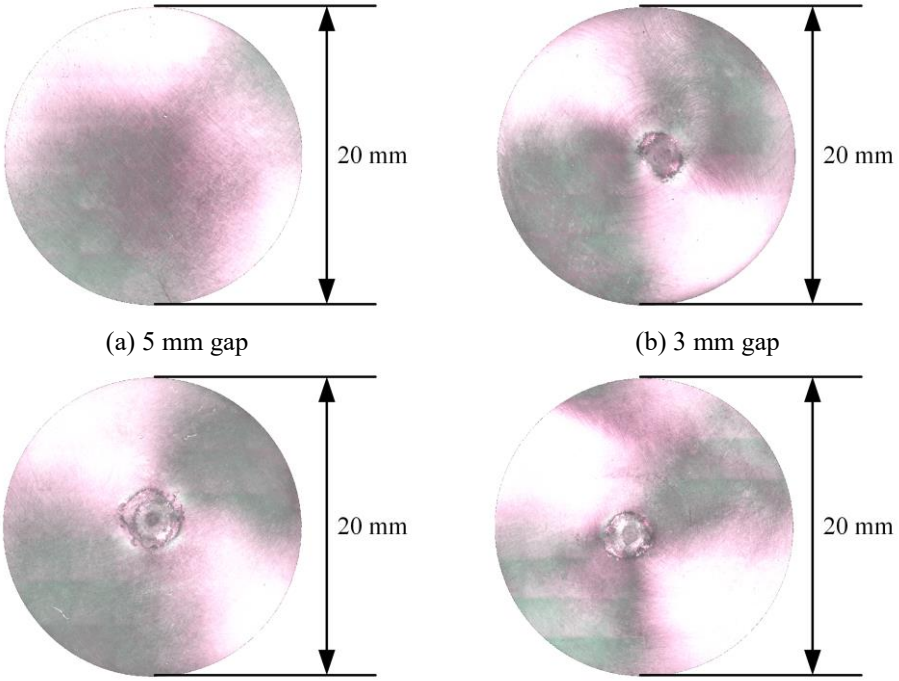

(a) 5 mm gap (b) 3 mm gap

(c) 1 mm gap (d) 0.5 mm gap

Figure 2-35 Anode surface after 1000 times of breakdown experiments (optical microscope)

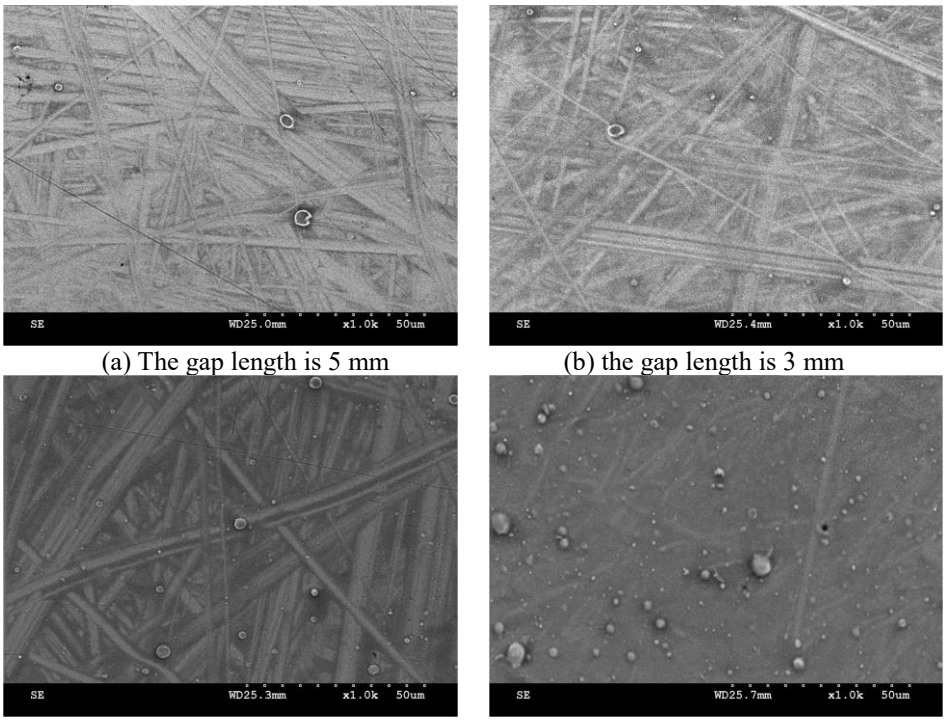

(a) The gap length is 5 mm (b) the gap length is 3 mm

(c) The clearance length is 1 mm (d) the gap length is 0.5 mm

Figure 2-36 Anode surface after 1000 times of breakdown experiments (SEM 1000x)

2.7 BRIEF SUMMARY

This chapter analyzes the electrical wavefroms, the spatio-temporal evolution of light radiation, and morphological changes of electrode surfaces during vacuum breakdown processes. Based on the results of this chapter and the corresponding discussion, the following conclusions can be obtained:

1) The vacuum breakdown process initiates when the electric field at the cathode surface reaches the breakdown threshold, and this result supports the theory of cathode-dominated breakdown. In the gap length range used in this chapter, the breakdown occurs when the electric field at the cathode surface reaches approximately 160 MV/m, which indicates that the breakdown is cathode-dominated. The whole process of vacuum breakdown consists of four stages: voltage rising stage (P0), conducting channel formation stage (P1), vacuum arc stage (P2) and arc extinction stage (P3). After the breakdown starts, the vacuum gap gradually changes from an insulated state to a conductive state, establishing a good conductive channel, and the time required for the channel to be established correlates positively with the gap length. Then, the breakdown enters a stable vacuum arc phase until the applied excitation disappears.

2) Cathode glow is produced by cathode plasma, and the establishment of cathode plasma is the necessary condition and indication for the start of vacuum breakdown evolution. Cathode glow appears immediately after the breakdown begins, accompanying the breakdown in the whole process. After theoretical calculation, it is confirmed that cathode glow is a result of the light radiation of plasma near the cathode.

The intensity and characteristic size of the cathode glow are relatively stable during breakdown and do not vary with gap size, which means that the burning of cathode plasma is a stable intrinsic process in a vacuum breakdown. The establishment of cathode plasma is a necessary condition for gap current to break through the limit of space charge effect, so the establishment of cathode plasma corresponds to the rapid rise of current and the beginning of breakdown.

3) The generation of anode glow is a secondary process in the vacuum breakdown process, its expansion towards the cathode is not a necessary condition for the conductive channel formation. This finding clarifies the non-necessity of the anode glow expansion and the light-radiation channel establishment in conductive channel formation of vacuum breakdown. The anode glow always appears later than the cathode glow, its emergence delay and the existence duration are affected by the gap length. Anode glow will expand towards the cathode after its appearance, and may establish a light-radiation channel in the gap. However, the formation of the light-radiation channel is much later than that of the conductive channel, and most of the gap is still in a dark state when the conductive channel is formed. Therefore, the expansion of the anode glow is not necessary for the formation of the conductive channel, the latter is likely to be attributed to the expansion of the cathode plasma.

4) During vacuum breakdown, the cathode surface is severely ablated while the anode surface shows no signs of melting. The maintenance of the current during breakdown relies on the burning of the cathode plasma, which leaves a huge number of molten craters on the cathode surface and causes a certain loss of the cathode material. On the contrary, no obvious melting traces are found on the anode surface, which also implies that the anode surface cannot produce plasma similar to the cathode side due to high temperature.

3 SPECTROSCOPIC ANALYSIS OF VACUUM BREAKDOWN PROCESS

3.1 OVERVIEW

It is well known that the establishment of a conductive channel relies on the formation of a plasma channel in the gap. In the previous chapter, it is found that the expansion of the anode glow does not contribute significantly to the conductive channel formation, so it is inferred that the expansion of the cathode plasma plays an important role in it. However, most regions of the vacuum gap have no optical radiation at the instant of the conductive channel formation, so the expansion of the cathode plasma cannot be directly observed. Then, attention is turned to the anode glow. The anode glow is a secondary process of cathode plasma expansion, and the cathode plasma can only build a conductive channel by expanding to the anode. Therefore, investigation of the particle composition in the anode glow region may provide some clues to understand the expansion behavior of the cathode plasma, and thus deepen the understanding of the mechanism of conductive channel formation during vacuum breakdown.

For the above purposes, this chapter will perform a spectroscopic analysis of the light radiation during vacuum breakdown, mainly focusing on the anode glow region. Several different electrode materials, including pure copper, brass (alloys of copper and zinc), aluminum, and tungsten, will be used in this chapter to distinguish between cathodes and anodes. Spectral information is obtained using a combination of a spectrometer and an ICCD camera. The micromorphology and composition of the anode surface were also analyzed using SEM and EDS (X-ray Energy Dispersive Spectrometer) after breakdown experiments. Based on the results of spectroscopic and microscopic analyses, the origins of the particle components in the anode glow region are clarified, and the expansion pattern of the cathode plasma and its role in the formation of conductive channels are revealed.

3.2 EXPERIMENTAL SETUP

Figure 3-1 shows the schematic diagram of the experimental setup. The observation equipment was changed to a combination of a spectrometer (Andor SR-500i) and an ICCD camera (Andor DH334T-18U-04) (indicated by N and E in the figure). The light radiation entering the slit of the spectrometer is transformed into a wavelength resolved image, which is finally captured by the ICCD camera. The spectrometer has a focal length of 500 mm and a best resolution of 0.05 nm at a slit width of 10 μm. The relevant settings of the spectrometer are performed via computer software and no additional trigger signal is required.

In this chapter, the tip-plane electrode structure shown in Figure 2-4 was still used. In

order to distinguish between different sources of the material in the anode glow and on the anode surface, the cathode and anode in the experiments were made of different materials. Cathode materials include tungsten (W), brass (alloys of copper and zinc, referred to below as BR) and aluminum (Al), while anode materials include pure copper (Cu) and aluminum (Al). The electrode combinations in the experiments are expressed in the way of "cathode material-anode material". For example, Al-Cu indicates the combination of aluminum tip cathode and pure copper plane anode. The gap length is uniformly set to 4 mm.

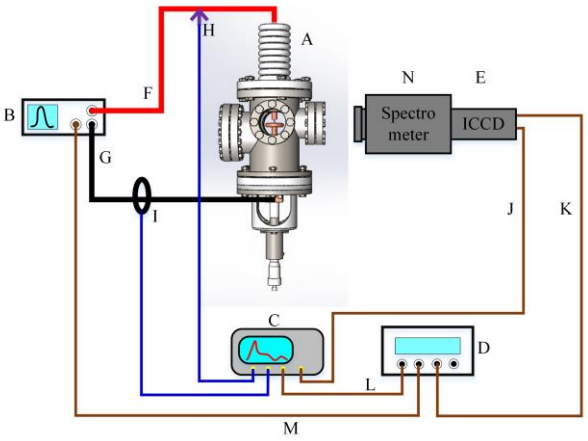

Figure 3-1 Schematic diagram of the vacuum breakdown test platform

In the experiment, the peak voltage and pulse width of the pulsed high-voltage source was set to -40 kV and of 5 μs. The corresponding steady-state arc current during the breakdown is 80 A, which is determined by the current limit resistance (R_1, 500 Ω). Typical voltage and current waveforms are shown in Figure 3-2. The starting point of the breakdown, t_0, is marked with a red arrow, which is the starting point for a rapid rise of current. The voltage and current waveforms in this diagram have the same pattern of evolution as Figure 2-10, so the waveforms are no longer discussed in this chapter. The delay between the spectral information recording and breakdown initiation is determined by the difference between the shutter monitoring signal of the ICCD camera and the breakdown instant t_0. When the exposure time of the camera is set to 7 μs, the shutter delay is set to negative, so that the shutter opens before breakdown starts, recording spectral information for the entire breakdown process.

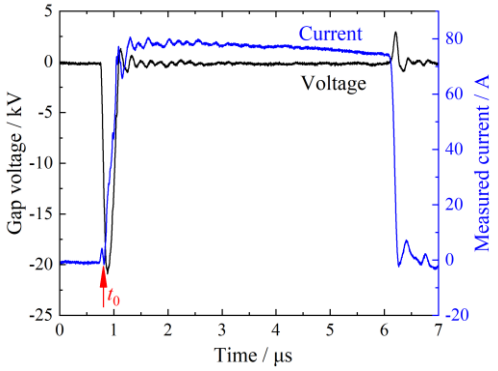

Figure 3-2 Typical voltage and current waveforms during the experiment (BR-Al)

3.3 SPECTRAL COMPOSITION OF LIGHT RADIATION DURING VACUUM BREAKDOWN

All possible spectral information about the vacuum breakdown process needs to be known before the spectra of specific wavelengths can be resolved in time and space. Therefore, the spectral information of the light radiation during vacuum breakdown is first observed without temporal resolution or spatial resolution. "No temporal resolution" means that the exposure time of the ICCD camera is set to 7 μs, covering the whole breakdown process (5 μs), and the light radiation of the whole process is accumulated on a single image. "No spatial resolution" refers to the vertical integration of the spectral image obtained by the ICCD camera. Since the transverse direction of the spectral image indicates the wavelength and the vertical direction indicates the spatial position, the vertical integration is to superimpose the light radiation of the same wavelength at all spatial positions. The spectral detection without spatial resolution is beneficial to improve the sensitivity and signal-to-noise ratio of the observation. The wavelength range of the observed spectra is set between 300 nm and 600 nm. The vacuum gap is imaged through the lens at the entrance slit of the spectrometer.

The experiment tested two different combinations of electrode material. One is the brass cathode to aluminum anode (BR-Al), and the other is the aluminum cathode to pure copper anode (Al-Cu). A gap length of 4 mm was used in both sets of experiments. The spectral results for both cases are shown in Figure 3-3. The top and bottom spectrum images in the figure correspond to the BR-Al and Al-Cu combinations, respectively, and the main spectral peaks are marked with corresponding atomic symbols. As can be seen, the spectral distribution is very different in both cases, with only two common Cu I spectral lines (324.8 nm and 327.4 nm) corresponding to the transition radiation of neutral copper atoms. In the case of BR-Al, only the spectra of cathode materials (brass, i.e. Cu and Zn) were observed in the wavelength range shown in Figure 3-3, but no significant anode material (Al) spectra were observed. Most of the spectra belong to Zn, and some of the lower-intensity spectra belonging to Cu ions (Cu II) have also been found. In the case of Al-Cu, by contrast, spectra from cathode material and anode material both exist, many of which correspond to aluminum ions (Al II, Al III).

What is intriguing in Figure 3-3 is the surprising absence of aluminum spectra in the case of BR-Al where the anode is aluminum (even for the aluminum atomic spectrum Al I, 394.4 nm and 396.1 nm). According to the results in the previous chapter, in all gaps from 0.5 mm to 5 mm, clear light radiation appears near the anode surface (see Figure 2-23 to Figure 2-25). Figure 3-4 also gives a light radiation image of the BR-Al electrode combination with a gap length of 4 mm taken directly by the ICCD camera after 500 ns from the onset of breakdown (50 ns exposure time), where the anode glow is indeed present. In addition, the expansion of the anode glow to the cathode also indicates that the anode surface is continuously providing the required atoms for the anode glow, so according to the intuitive analysis, some spectral lines of the anode material (Al) should be present in the spectrogram of the BR-Al

combination. In this sense, the spectrogram obtained in the case of Al-Cu contains both copper and aluminum spectra, which is more in line with the intuitive judgment. Since there are no spectra of anode material (Al) during the vacuum breakdown in the BR-Al case, the particle composition of the anode glow will be investigated by further experimental analysis in the following.

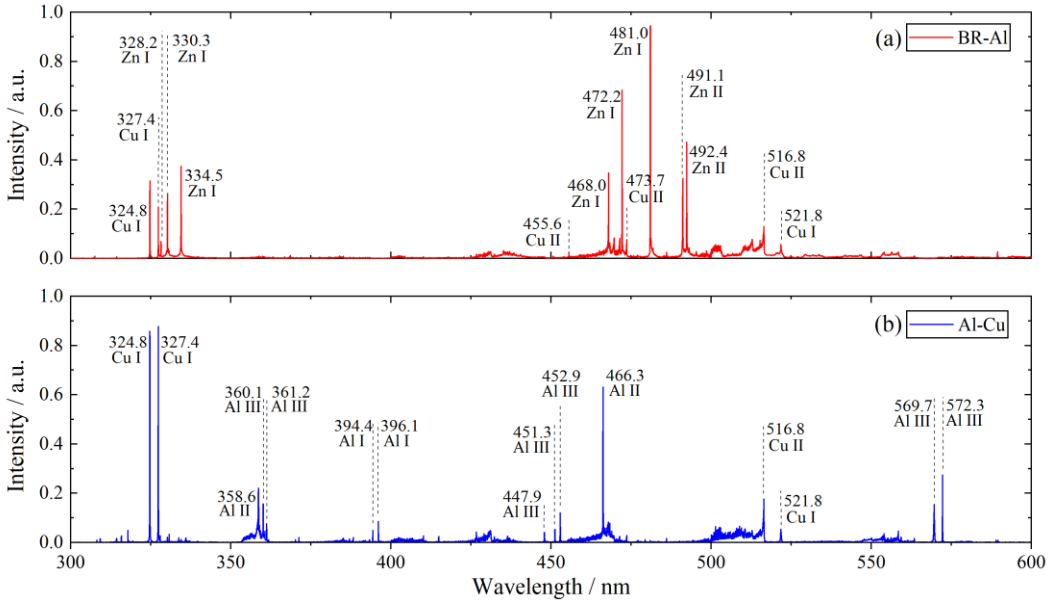

Figure 3-3 Spectral distribution of the light radiation during breakdowns in two different electrode combination (ICCD camera exposure time is 7 μs)

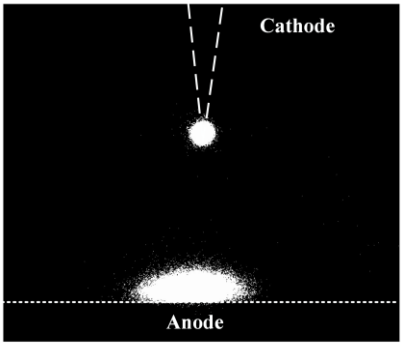

Figure 3-4 An image without spectral resolution at 500 ns after the onset of vacuum breakdown taken directly using ICCD

3.4 SPATIO-TEMPORAL RESOLVED SPECTRA OF VACUUM BREAKDOWN PROCESS

In order to analyze the particle composition in the anode glow region in the BR-Al case, the spectra during vacuum breakdown were spatially resolved. By adjusting the lens and 3D movable stage, the axis of the vacuum gap is imaged onto the entrance slit of the spectrometer. The shutter of the ICCD camera is then set to open between 300-500 ns after the breakdown initiation to observe the spatial distribution of the spectra within this time window. The major spectrum peaks in Figure 3-3 were all

captured and it is found that the distribution of all major spectra along the gap in the BR-Al case has the same characteristics. Two spectral lines (468.0 nm and 472.2 nm) of Zn I (neutral Zn atom) are shown in Figure 3-5 to illustrate the spatial distribution of the spectral lines. Since the intensity of the spectra is too weak and the signal-to-noise ratio of the spectrograms obtained from a single breakdown process is too poor, Figure 3-5 shows the results of 50 breakdown accumulations. The vertical positions of the cathode tip and the anode surface are indicated by dashed lines. It can be seen that the spectra on the cathode side are dominated by continuous radiation, mainly from the interaction between electrons and charged particles producing bremsstrahlung radiation and recombination radiation. It is well known that both radiation mechanisms decrease rapidly as density and temperature of plasma decrease[88, 89], which indirectly indicates that the plasma temperature and density in the cathode glow region are high and that the temperature and density decay very quickly in space. On the anode side, there are two distinct Zn I spectral lines in the anode glow region. When the recording range of the spectrometer is set within the wavelength range of the Al I spectra (394.4 nm and 396.1 nm), the relevant spectra are indeed absent in the case of BR-Al.

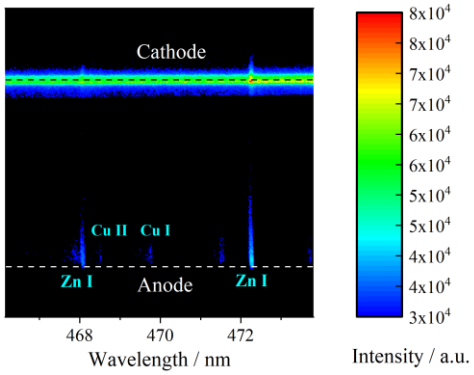

Figure 3-5 Spatial distribution of Zn spectra in BR-Al electrode combination (Zn I: 468.0 nm, 472.2 nm)

Figure 3-6 shows the spatio-temporal evolution of the Zn I spectra in the anode glow in the BR-Al case, where the position of the anode surface in the vertical direction is represented by a dashed line, and the images in the figure are still a cumulative result of 50 breakdowns. The red number above each image indicates the delay of the ICCD camera shutter relative to the start of the breakdown, and the camera exposure time is set to 50 ns. As can be seen from the figure, the Zn I spectra in the anode glow appear about 200 ns after the breakdown begins and gradually expand toward the cathode in the subsequent process. The instant the Zn I spectra appear and their expansion to the cathode coincides with those of the overall light radiation in Section 2.4 (see Figure 2-23 to Figure 2-25).

According to the spatial distribution and time evolution of the anode glow spectra shown in Figure 3-5 and Figure 3-6, in the case of BR-Al, most anode glow is produced by cathode material, i.e. copper and zinc, because there is no obvious spectral signal of aluminum. However, in the case of Al-Cu, cathode material spectra (Al I, 394.4 nm and 396.1 nm) and anode material spectra (Cu I, 324.8 nm and 327.4 nm) can be observed simultaneously in the anode glow. Figure 3-7 and Figure 3-8

display the spatio-temporal evolution of the Al I (cathode material) and Cu I (anode material) spectra in the Al-Cu case, respectively, each of which is the accumulative result of 50 breakdown experiments. As can be seen, the Al I and Cu I spectra are also gradually expanding toward the cathode in the pattern as in Figure 2-23.

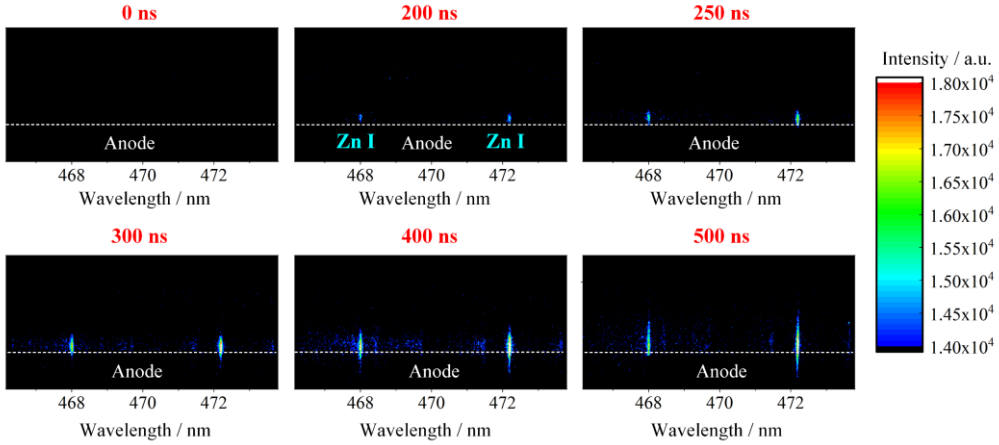

Figure 3-6 Spatio-temporal evolution of the Zn I spectra (468.0 nm，472.2 nm) in the anode glow in the BR-Al case

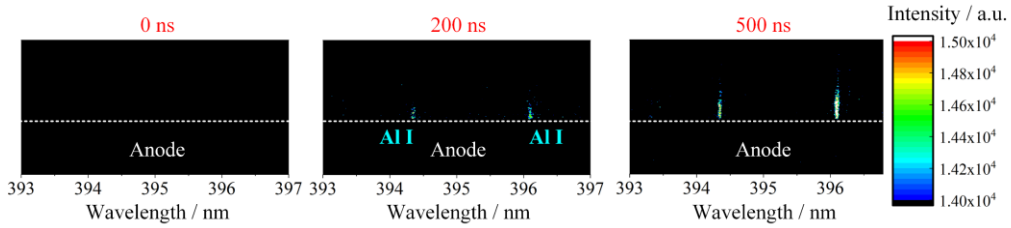

Figure 3-7 Spatio-temporal evolution of the Al I spectra (394.4 nm, 396.1 nm) in the anode glow in the Al-Cu case

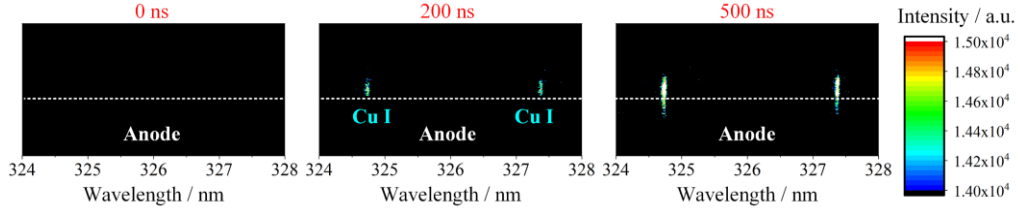

Figure 3-8 Spatio-temporal evolution of the Cu I spectra (324.7 nm, 327.4 nm) in the anode glow in the Al-Cu case

In this section, the spectra of two different combinations of electrode materials, BR-Al and Al-Cu, during vacuum breakdown are investigated. The main spectral signals are derived from the metal materials of cathode and anode, which also indicates that the vacuum arc is a metal vapor arc. The spectra contained in the anode glow may change due to changes in the experimental conditions. In both cases, the spectra of the corresponding cathode material were detected in the anode glow. In contrast, the spectra of the anode material appeared in the anode glow region only in the Al-Cu case, while the anode material spectra were not detected in the anode glow for the BR-Al case. It should be noted that the electrode system has been subjected to hundreds of breakdown experiments before all the spectral information was collected in this section.

3.5 ORIGIN ANALYSIS OF CATHODE MATERIAL SPECTRA IN ANODE GLOW

In the previous section, it was observed that there are cathode material spectra in the anode glow during vacuum breakdown. Understanding how the cathode material is involved in the anode glow is important for analyzing how the cathode plasma expands during breakdown and can also provide clues to the formation mechanism of the conductive channel. Therefore, this section will analyze the reason for the presence of cathode material spectra in the anode glow region during vacuum breakdown.

It is well known that there may be material transfer between the cathode and the anode during arc discharge. In particular, during vacuum breakdown, both electrons and ions from the cathode plasma have a directional motion velocity towards the anode[84, 86, 90-93]. Therefore, there are two possible explanations for the presence of cathode material spectra in anode glow, as shown in Figure 3-9. The small blue dots in the figure represent the atoms of the cathode material, including neutral atoms and ions, and the arrows indicate the direction of motion of the atoms. The mechanism illustrated in Figure 3-9(a) is called the contamination mechanism, where the cathode material transfers to the anode during multiple preceding breakdowns and forms a contamination layer of cathode material on the anode surface. This contamination layer provides atoms to the anode glow region during subsequent breakdown, thus resulting in the spectra of the cathode material in the anode glow. The mechanism demonstrated in Figure 3-9(b) is called the reflection mechanism, whereby the cathode material ions in the cathode plasma expanding toward the anode during the ongoing breakdown undergo charge neutralization and reflection at the anode surface. The reflected cathode material atoms enter the anode glow region, leading to the spectra of the cathode material in the anode glow. The two possible mechanisms will be discussed separately by experiments below.

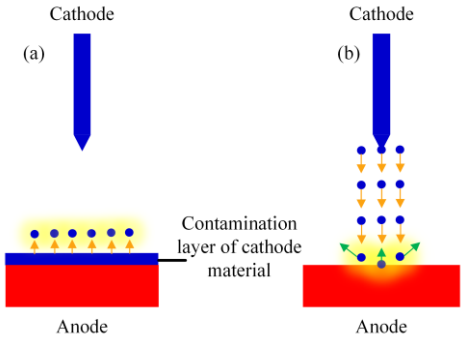

Figure 3-9 Possible mechanisms for the presence of cathode material spectra in anode glow, (a)-Contamination mechanism, (b)-Reflection mechanism

3.5.1 FORMATION OF CATHODE MATERIAL CONTAMINATION LAYER DUE TO PRECEDING BREAKDOWNS

Four sets of experiments were set up to verify the possibility of contamination mechanism, as shown in Table 3-1. The four sets of experiments in the table were

performed using combinations of cathodes and anodes with different materials and surface conditions, and then the spectral information in the anode glow was observed. The purpose of this experiment is to verify the contamination of the anode surface by the cathode material, so the main focus is on the cathode material spectra (Zn I and Zn II) in the anode glow.

The cathode in Group 1 was a needle electrode made of brass and the anode was an aluminum plate. This BR-Al electrode combination had been subjected to hundreds of breakdowns before recording the spectra, which is consistent with the experimental conditions of the BR-Al case in Section 3.3. In other words, assuming that the transfer of the cathode material to the anode during vacuum breakdown causes contamination of the anode surface, a significant contamination layer of brass (cathode material) was already present on the anode surface when the spectra recording started. In Group 2, a tungsten needle was used as the cathode instead of a brass needle, ruling out the possibility of further deposition of brass on the aluminum anode, but the anode was not replaced. At this time, the presence of a cathode material contamination layer on the anode surface and whether this contamination layer may provide atoms for anode glow can be determined by observing the presence of cathode material spectra in the anode glow. In Group 3, the cathode and anode were replaced with new tungsten needle and aluminum plate, respectively, for the purpose of comparison with Group 2. In Group 4, a brand-new brass needle was used as cathode and a brand-new aluminum plate was used as anode, and then the intensity change of the observed spectra was recorded as the cumulative number of breakdowns increases. For the convenience of the reader, the presence states of the observed zinc spectra in the anode glow for each set of experimental conditions are briefly given in the last column of Table 3-1.

Table 3-1 Verification experiments for the contamination mechanism shown in Figure 3-9(a)

Experiment group	Gap length/mm	Cathode material	Anode material	Anode Surface condition	Zinc spectra in anode glow
1	4	BR (Cu&Zn)	Al	After multiple discharges	Presnt
2	4	W	Al	After Experiment 1	Presnt
3	4	W	Al	brand new	Absent
4	4	BR (Cu&Zn)	Al	brand new	Gradually increasing

Figure 3-10 and Figure 3-11 show the presence of the main spectra of the cathode material, Zn I (468.0 nm, 472.2 nm) and Zn II (491.1 nm, 492.4 nm), in the anode glow for different experimental conditions in Table 3-1, respectively. All spectrograms were taken 600 ns after the onset of vacuum breakdown with an exposure time of 50 ns for ICCD. Each spectrogram is the result of the accumulation of 25 breakdown experiments, and the position of the anode surface in the vertical direction is indicated by a dashed line. The experiment group corresponding to each plot is marked in red font above the image, where groups 4-1, 4-2 and 4-3 are all part of Group 4,

demonstrating the variation of the measured spectral intensity with increasing number of breakdowns. The three images corresponding to the labels 4-1, 4-2, and 4-3 in Figure 3-10 record the cumulative spectra of the 51st-75th, 76th-100th, and 601-625th breakdowns of Group 4, respectively. The cumulative spectra of the 1st-25th, 101st-125th and 626th-650th breakdowns of Group 4 are recorded in the three images labelled by 4-1, 4-2 and 4-3 in Figure 3-11, respectively.

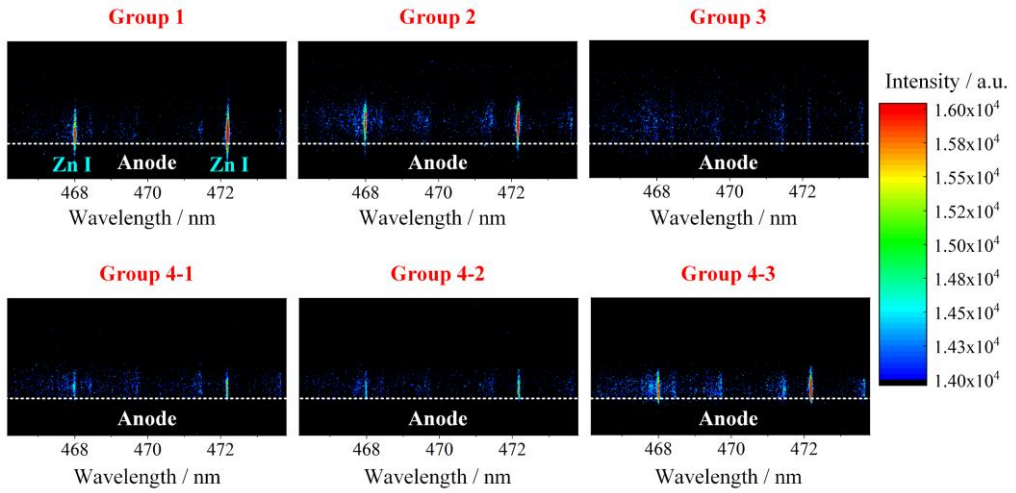

Figure 3-10 Cathode material spectra in anode glow during vacuum breakdown for different experiment groups in Table 3-1 (Zn I: 468.0 nm, 472.2 nm; ICCD shutter opens during 600-650 ns)

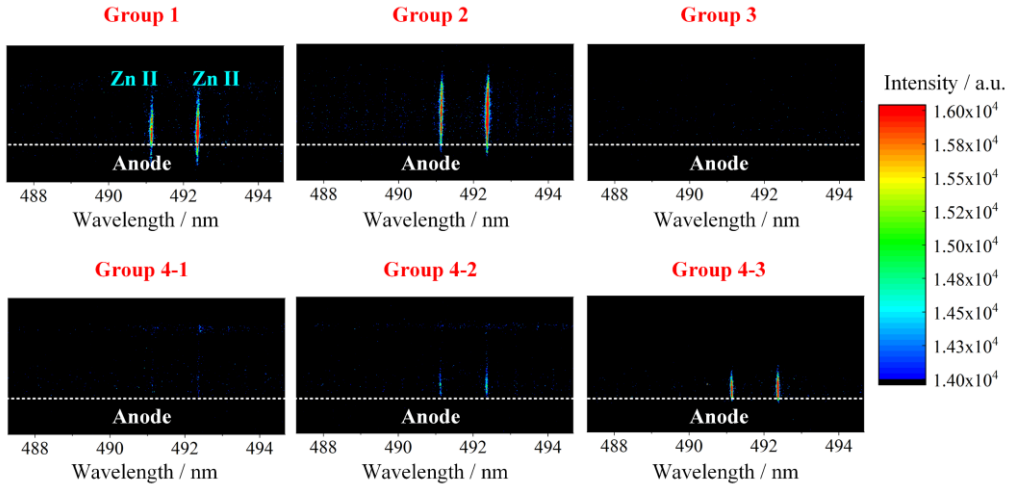

Figure 3-11 Cathode material spectra in anode glow during vacuum breakdown for different experiment groups in Table 3-1 (Zn II: 491.1 nm, 492.4 nm; ICCD shutter opens during 600-650 ns)

By observing Figure 3-10 and Figure 3-11, it can be found that four spectral signals of the cathode material, Zn I (468.0 nm, 472.2 nm) and Zn II (491.1 nm, 492.4 nm), are present in the anode glow under the experimental conditions in Group 1, which is consistent with the results in Figure 3-5. In Group 2, the spectra corresponding to Zn I and Zn II were still present in the anode glow. Since the brass cathode has been replaced by a tungsten cathode in Group 2, there is no longer any Zn present in the cathode, so the spectra of Zn observed at this time could only come from the anode surface. This means that there is indeed a contamination layer on the surface of the aluminum anode consisting of the previous cathode material (brass), and this

contamination layer will provide light-emitting atoms to the anode glow region in the process of vacuum breakdown. In addition, the results of the second group of experiments also indicate that the anode surface has an important contribution to the formation of anode glow, although the contributing atoms do not necessarily come from the native material of the anode (aluminum).

The results of the Group 3 and 4 further confirm the above conclusions. In Group 3, the four zinc spectra disappeared completely when the cathode and anode were replaced with brand-new tungsten needle and aluminum plate, respectively. In the Group 4, a brass cathode were reinstalled, and the spectral intensity of zinc increased with the number of breakdowns, and finally the spectral intensity became similar to that of Group 1.

In order to confirm more directly the contamination mechanism described in Figure 3-9(a), microscopic analysis of the anode surface after the breakdown experiment was carried out. After the breakdown experiments, the electrodes were removed from the vacuum chamber and the elemental composition of the anode surface was examined with a scanning electron microscope (SEM) equipped with an EDS analyzer. Three electrode material combinations including BR-Al, Al-Cu and W-Cu were tested and the results are shown in Figure 3-12. Figures (a) and (b) correspond to BR-Al; (c) and (d) correspond to Al-Cu; (e) and (f) correspond to W-Cu. Each subplot contains a main plot and an inset. The inset shows the microscopic morphology of the anode surface (the scale bar corresponds to 20 μm), while the main plot shows the energy spectrum at a sample point on the anode surface. The location of the sample point is marked by a red circle in the inset and by a distinctive white arrow near the sample point. The horizontal axis of the energy spectrum plot indicates the X-ray energy and the vertical axis indicates the corresponding energy spectrum intensity.

The microscopic morphology of the anode surface in the inset shows the presence of a large number of spherical particles on the anode surface after breakdown experiments, and the size of the particles is about a few microns. The sample points for the energy spectrum analysis in Figure 3-12(a), (b), (c) and (e) are all in the vicinity of spherical particles with the aim of determining the origin of the spherical particles. In Figure 3-12(a), (c) and (e), the energy spectrum results show that the composition at the sample points is mainly cathode material, which is due to the large size of the particles at the sample points in these three figures, so that the energy spectrum data obtained from the sampling are almost all from the particles. This also indicates that these spherical particles on the anode surface are indeed from the cathode. In Figure 3-12(b), the particle size near the sample point is smaller, and the sampled energy spectrum data also includes the nearby anode surface, so the energy spectrum data shows that both anode and cathode materials are present. In Figure 3-12(d) and (f), the sample point was set at the smoother region of the anode surface, where the energy spectrum signals of both cathode and anode materials were detected. Based on these SEM and EDS analysis results in Figure 3-12, it can be concluded that there is indeed a transfer of cathode material to the anode during vacuum breakdown, and the cathode material reaching the anode may exist as micron-sized particles or may be smoothly condensed on the anode surface in the form of vapor.

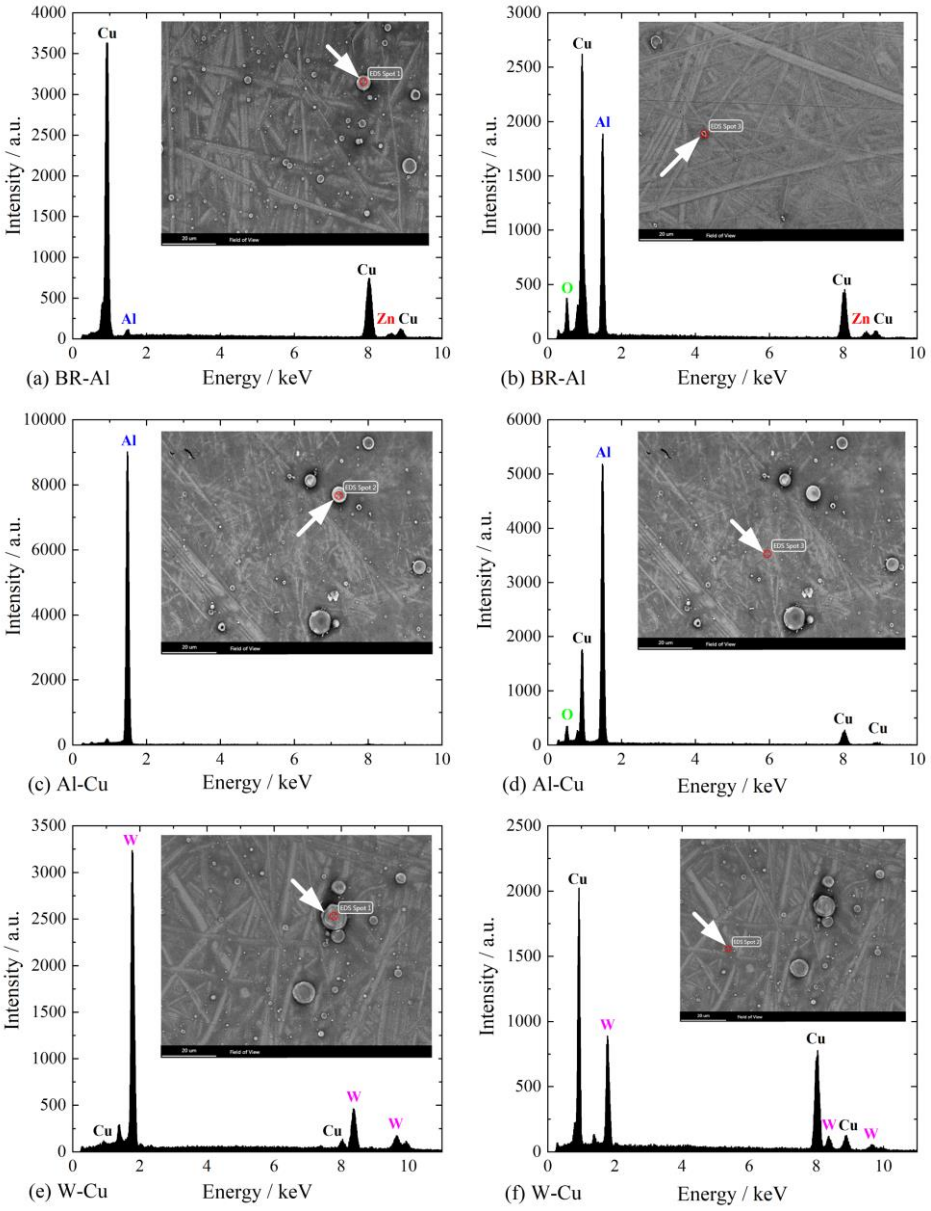

Figure 3-12 Composition analysis of the anode surface after vacuum breakdown experiments

Through the four sets of experiments in Table 3-1 and the microscopic analysis of the anode surface after breakdown, it can be demonstrated that the cathode material gradually transfers to the anode during vacuum breakdown and deposits on the anode surface in the form of vapor or particles, forming a contamination layer of cathode material. The contamination layer can provide atoms for the anode glow region in the subsequent breakdown processes, which makes an important contribution to the anode glow. Thus, the contamination mechanism in Figure 3-9(a) is confirmed and one of the reasons for the presence of the cathode material spectra in the anode glow during vacuum breakdown is the contamination of the anode surface by the cathode material during the preceding breakdowns.

3.5.2 EXPANSION AND REFLECTION OF CATHODE PLASMA DURING ONGOING BREAKDOWN

Next, the existence of the reflection mechanism shown in Figure 3-9(b) will be experimentally verified. As mentioned earlier, the reflection mechanism refers to the charge neutralization and reflection of the cathode material ions in the expanding cathode plasma at the anode surface during the ongoing breakdown process. The reflected atoms of the cathode material may accumulate in the vicinity of the anode surface, hence, giving rise to spectral signal of the cathode material in the anode glow.

To rule out the effects on the spectral measurements of the possible contamination by the cathode material on the anode surface, only the spectra of the first few breakdowns with brand-new electrodes were collected in the following experiments. In addition, the time period for spectrum recording was adjusted to the beginning of the anode glow. According to the evolution of the light emission during breakdowns with different gap lengths in Section 2.4 and the evolution of the spectra in Figure 3-6 to Figure 3-8, the anode glow appears at about 200-250 ns in a 4 mm gap, so the shutter of the ICCD camera is set to open at about 250 ns from the breakdown initiation. The effect of anode contamination during breakdown can be minimized using the above two measures.

Figure 3-13 shows the spatial distribution of the cathode material and anode material spectra for the first two breakdowns of the brand-new electrodes. Two electrode material combinations, BR-Al and Al-Cu, were used for the experiments. In these images, the distributions of Cu I (324.7 nm and 327.4 nm) or Al I (394.4 nm and 396.1 nm) spectra are provided, respectively. Each spectrogram is the result of a single vacuum breakdown, so that only two breakdown experiments were performed for each case, which ensures that the contamination layer of the cathode material on the anode surface is not sufficient to affect the results of the spectral analysis. During the first breakdown of each case, the observation range of the spectrometer is set to cover the cathode material spectra, while the second breakdown allows the spectrometer observation range to cover the anode material spectra. In the BR-Al case, Figure 3-13(a) and (b) show the distribution of the Cu I spectra at the first breakdown and the distribution of the Al I spectra at the second breakdown. In the Al-Cu case, Figure 3-13(c) and (d) show the distribution of the Al I spectra at the first breakdown and the distribution of the Cu I spectra at the second breakdown. The shutter of the ICCD camera opens between 300-500 ns after the onset of breakdown in Figure 3-13(b), and opens between 250-350 ns in the remaining three figures to ensure that the period for spectrum recording is at the initial stage of anode glow. The increase in shutter delay and exposure time in Figure 3-13(b) is due to the fact that the spectral signal of aluminum in this case is too weak between 250-350 ns for observation. The positions of the electrodes are marked by dashed lines in each spectrogram, and the corresponding atomic symbols of each spectrum are marked in blue font nearby.

According to Figure 3-13(a) and (c), the spectra of the cathode material (i.e., Cu I in the case of BR-Al and Al I in the case of Al-Cu) can still be observed near the anode surface even at the initial stage of the anode glow during the first breakdown of the brand-new electrodes. Under such experimental conditions, the contamination of the

anode surface is negligible, so this result implies that the cathode of the ongoing breakdown process also supplies atoms to the anode glow region. This also means that the reflection mechanism described in Figure 3-9(b) for explaining the presence of the cathode material spectra in the anode glow is plausible. Furthermore, the fact that atoms from the cathode are involved just at the beginning of the anode glow suggests that the cathode plasma can indeed expand toward the anode without emitting light and has already reached the anode before the anode glow appears. Since the cathode plasma has already reached the anode when the anode glow appears, the conductive channel in the vacuum gap has basically been established at this time. Therefore, the expansion of the cathode plasma has an important role in the establishment of the conductive channel during vacuum breakdown, confirming the inference in Chapter 2.

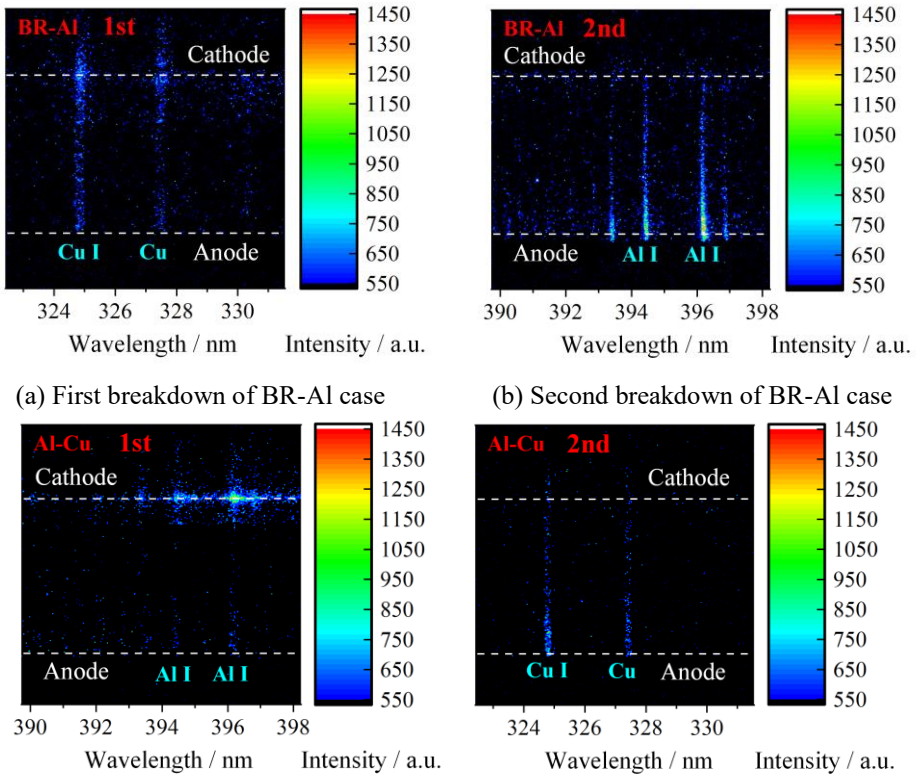

(a) First breakdown of BR-Al case (b) Second breakdown of BR-Al case

(c) First breakdown of Al-Cu case (d) Second breakdown of Al-Cu case

Figure 3-13 Spatial distribution of cathode material and anode material spectra during the first two breakdowns of new electrodes (Cu I-324.7 nm, 327.4 nm; Al I-394.4 nm, 396.1 nm)

A closer look at the spatial distribution of the spectra in Figure 3-13(a) and (c) reveals that the intensities of these cathode material spectra near the cathode and anode are higher than those in the middle of the gap. The cathode material in the anode glow comes from the cathode glow region by expansion through the gap, so the higher intensity of the spectra near the anode than the gap indicates that the atoms of the cathode material will interact with the anode surface after reaching the anode which makes its density rise. The rise in density of the cathode atoms near the anode may be due to a decrease in velocity after emission from the anode surface or due to charge neutralization of ions with higher valence at the anode surface, but the specific interaction process and the mechanism of the density rise need to be studied in more detail.

Next, attention is turned to Figure 3-13(b) and (d), which show the spatial distribution of the anode material spectra during the second breakdown of the two cases. It is clear from the figures that the spectra of the anode material are also present near the anode surface. For the Al-Cu case, the anode material spectra (Cu I, 324.7 nm and 327.4 nm) shown in Figure 3-13 are consistent with those in Figure 3-3(b) and Figure 3-8. However, for the BR-Al case, there are spectra of anode materials (Al I, 394.4 nm and 396.1 nm) present in the anode glow as shown in Figure 3-13(b), which is inconsistent with the absence of the aluminum spectra in Figure 3-3(a).

As mentioned above, hundreds of breakdown experiments have been performed between the electrodes before the spectra were collected for the BR-Al case in Figure 3-3. According to the discussion on the contamination mechanism in the previous section, the anode surface could have already been contaminated by the transferred cathode material. To investigate whether the absence of the Al I spectra in Figure 3-3(a) (BR-Al electrode combination) is related to the contamination of the anode surface, 598 breakdown experiments were further performed on the BR-Al electrode combination used in Figure 3-13, and then the Al I spectra were collected again.

Figure 3-14 shows the spectral distribution in the wavelength range of the Al I spectra (394.4 nm and 396.1 nm) after 600 breakdowns of the new BR-Al electrode. To ensure that any Al I spectral signal that may be present can be observed, this spectrogram accumulates all signals from the 601st to 650th vacuum breakdowns. However, there is hardly any signal of Al I in Figure 3-14, a result that is in perfect agreement with Figure 3-3(a). This phenomenon indicates that the contribution of the native anode material to the anode glow decreases or even disappears with the increase of breakdown times in the case of BR-Al electrode combination.

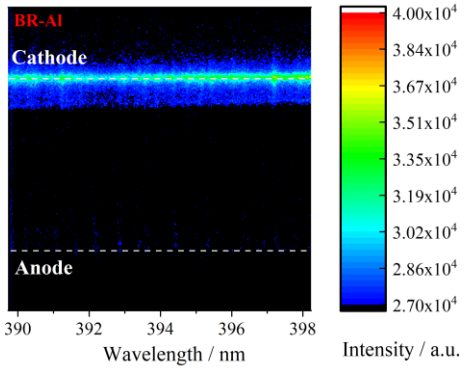

Figure 3-14 Spectral distribution in the wavelength range of Al I spectra (394.4 nm and 396.1 nm) after 600 breakdowns of the new BR-Al electrode

Of course, the disappearance of the spectra of the native anode material in the anode glow does not mean that the anode no longer contributes atoms to the anode glow. According to the contamination mechanism in the previous subsection, the contamination layer of cathode material formed on the anode surface will also provide atoms to the anode glow region during the breakdown. In other words, the anode is always an important atom source for the anode glow, only that as the degree of contamination on the anode surface increases, the atoms provided by the anode for the anode glow region may gradually change from the native anode material to the cathode

material deposited on the anode surface.

3.6 DISCUSSION

Before the appearance of the anode glow, the expansion process of the cathode plasma has already started, although most of the gap is still dark. When the anode glow starts to appear, a large number of atoms and ions of the cathode material have already reached the anode and been involved in the anode glow. This result is consistent with the model of plasma expansion proposed by Ni and Anders[91, 94]. According to this model, the dense cathode plasma expands toward the anode at supersonic speed right from the beginning of vacuum breakdown. The front of the expanding plasma is the front of ion motion, and the region between this front and the cathode is occupied by a plasma composed of electrons and ions, while only electrons are present in the region between the front and the anode. Therefore, the potential difference between the plasma front and the cathode is very small, and most of the gap voltage is applied to the region between the plasma front and the anode to accelerate the electrons in this region. According to the delay of the anode glow in this work, the expansion velocity of the cathode plasma is on the order of 10^4 m/s, which is consistent with the results obtained by Shmelev and Barengolts through PIC simulations[84]. The cathode plasma does not produce optical radiation during the expansion process, making it impossible to observe it directly[1, 94]. However, when the expanding cathode plasma reaches the anode, it interacts strongly with the anode surface. The results of the interaction are the reflection of atoms from the cathode and the emission of atoms from the anode surface, which interact with electrons near the anode surface to produce the anode glow.

The atomic stream from the cathode does not emit light during the expansion process, while the interaction with the anode produces a significant luminescence. This indicates that the reflection of the cathode atomic stream on the anode surface causes a significant increase in the cathode atom density in the vicinity of the anode. This may be caused by the decrease of the atom velocity after reflection or by the fact that a large number of ions with higher valence become atoms after charge neutralization. However, the reason for the absence of luminescence during cathode plasma expansion and the specific process of cathode atom-anode surface interaction still need further experimental and theoretical studies.

As the results in section 3.5 show, the anode always supplies atoms to the anode glow region during breakdown, but these atoms may come from the native anode material or from a contaminated layer of cathode material on the anode surface. In new electrode systems, the spectra of the native anode material can be clearly detected in the anode glow. As the number of breakdowns increases, more and more cathode material is deposited on the anode surface, and the contribution of this deposited contamination layer to the anode glow gradually increases. In some cases, such as the BR-Al electrode combination, the contamination of the anode surface by the cathode material may even lead to the complete disappearance of the spectral signal of the

anode material from the anode glow. The different attenuation behaviors of the aluminum and copper spectra in the BR-Al and Al-Cu cases may be due to the different properties of the corresponding electrode materials, which need to be further investigated.

3.7 BRIEF SUMMARY

In Chapter 2, it was found that the expansion process of the anode glow to the cathode contributes marginally to the formation of the conductive channel during vacuum breakdown, and it was speculated that the expansion of the cathode plasma is the main reason for the formation of the conductive channel. In order to confirm whether the cathode plasma can expand through the gap to reach the anode surface without light emission, this chapter conducted a spectroscopic analysis of the anode glow during vacuum breakdown using a spectrometer, and a microscopic morphological analysis and elemental composition analysis of the anode surface after the breakdown experiment using SEM and EDS. The analyses of the experimental results lead to the following conclusions:

1) The cathode plasma can expand through the dark vacuum gap to reach the anode and play a major role in the establishment of the conductive channel. After breakdown occurs, the cathode plasma forms near the cathode surface and produces the cathode glow in a localized region. Although the expansion of the cathode glow region is very limited, leaving most of the gap in a dark state, the cathode plasma is expanding toward the anode and reaches the anode surface before the anode glow appears. The expansion of the cathode plasma makes the conductivity of the gap gradually increase and the voltage gradually decrease, playing a major role in the formation of the conductive channel.

2) The anode glow contains not only atoms from the anode, but also atoms provided by the cathode plasma. This finding updates the conventional view that the anode glow must come from the anode. During each breakdown, ions in the expanding cathode plasma participate in the anode glow by charge neutralization and reflection at the anode surface. The atoms on the anode surface also leave the anode surface and participate in the anode glow, and these atoms may belong to the native anode material or to the cathode material contamination layer. The cathode material contamination layer is formed as a result of material transfer in preceding breakdowns and includes both smooth atomic deposits condensed in the form of vapor and micron-sized spherical particles.

4 ANODE PHYSICAL PROCESSES IN VACUUM BREAKDOWN AND THEIR ROLE IN CONDUCTIVE CHANNEL FORMATION

4.1 OVERVIEW

The results of the spectral analysis show that the light radiation during the vacuum breakdown comes from the electrode material, so the physical processes on the cathode and anode surfaces determine the nature of the corresponding light radiation and its role in the formation of the conductive channel. The physical processes on the cathode surface and its role in the conductive channel formation have been analyzed in the previous sections. According to the discussion in Sections 2.5.1 and 2.6.1, there are a large number of thermal instability processes on the cathode surface during vacuum breakdown, and a luminous cathode plasma is formed near the cathode. The expansion process of the cathode plasma in the vacuum gap plays a major role in the formation of the conductive channel. This chapter focuses on the analysis of the physical processes on the anode surface and their relation to the conductive channel formation.

The results of the previous chapter show that the anode glow comes from the transition radiation of the atoms from the cathode and the anode. The atoms from the cathode belong to the cathode material and participate in the anode glow after charge neutralization and reflection at the anode surface. The atoms from the anode may belong to the native anode material or to the cathode material contamination layer on the anode surface, but the physical processes leading to the emission of these atoms from the anode surface have not been determined. There are two possible mechanisms for atoms from the anode surface to enter the anode glow region, one is the evaporation of the anode surface under the heating effect of the cathode plasma, which is the conventional view on the mechanism of anode glow generation, and the other is the sputtering of the anode surface under the impact of the cathode plasma.

In addition, through the study in Chapter 2, it was found that the expansion of the anode glow does not play a decisive role in the conductive channel formation during vacuum breakdown, and it was inferred that the expansion of the cathode plasma is the main cause of the conductive channel formation. In Chapter 3, the spectral analysis of the anode glow confirmed that the cathode plasma can indeed expand to reach the anode without glowing and play a major role in the conductive channel formation. However, comparing the instant of the onset of the anode glow in Table 2-2 and the instant of the formation of the conductive channel in Table 2-5, it is found that the conductive channel is formed a short time after the onset of the anode glow. This leads to a new question, whether the emergence of the anode glow is necessary in the formation of the conductive channel.

Therefore, the objective of this chapter is to reveal the physical mechanisms leading to the entry of atoms on the anode surface into the anode glow region and to elucidate the relationship between the appearance of the anode glow and the formation of the conductive channel during vacuum breakdown. The main observations are the instants for the anode glow appearance and the conductive channel formation. In order to improve the accuracy of the measurements, a streak camera with continuous time resolution at the picosecond level is used as the observation device. In order to investigate the physical processes on the electrode behind the anode glow, a comparative study of the results for six different anode materials, three different gap lengths and two applied voltages was carried out.

4.2 EXPERIMENTAL SETUP

Figure 4-1 shows the schematic diagram of the experimental setup. The experimental system in this chapter is basically the same as the previous two chapters. The observation equipment for the experiments in this chapter is changed to a streak camera (Model XIOPM-2200, denoted by O in the figure). Unlike the ICCD camera, the streak camera can obtain the light radiation evolution of vacuum breakdown in a single breakdown experiment, without the need of stitching multiple results. In addition, the image obtained by the streak camera reflects the continuous time evolution of the light radiation and has a resolution of up to picosecond level, which can accurately obtain the the instant of the onset of the anode glow during each vacuum breakdown.

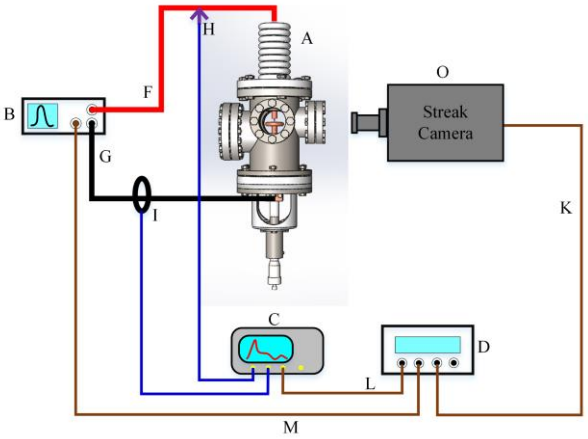

Figure 4-1 Schematic diagram of experimental setup

Figure 4-2 is a schematic diagram of the structure and working principle of the streak camera used in the experiment, whose function can be briefly described as to image the continuous time evolution of a one-dimensional space with a temporal resolution of up to a few picoseconds. The streak camera consists of a slit, a photocathode, a scanning circuit, a pair of deflection electrodes, a microchannel plate (MCP), a fluorescent screen, and a CCD (Charge-Coupled Device) camera. The slit is used to select the area to be observed (a narrow area of tens of microns, i.e., a one-dimensional (actually narrow two-dimensional) observation object), and its width can be adjusted.

As shown in Figure 4-2, the light radiation of the observed object is imaged at the slit of the streak camera through a lens. Due to the selective effect of the slit, only photons that can pass through the slit are finally imaged on the CCD camera. The light blue plane with a grid is used to represent the plane through the slit and parallel to the optical axis of the streak camera, hereinafter referred to as the main plane. As shown in the coordinate axis on the main plane on the left side of the slit, the horizontal direction of the main plane indicates the time t. The direction perpendicular to the page indicates the spatial position along the direction of the slit x, while the direction perpendicular to the main plane is indicated by y. The three round dots on the main plane represent photons, and their colors indicate the different light intensities. The different positions of the three round dots on the main plane grid indicate the differences in the time sequence and spatial location for the arrival of the three photons at the slit, as shown in the coordinate diagram in the upper left corner. Photons passing through the slit irradiate onto the photocathode and produce photoelectrons which are represented by triangles due to the photoelectric effect. The temporal, spatial and intensity information of the incident photons is transformed into the instant of emission, the position of emission and the number of photoelectrons emitted, respectively, where the difference in the number of emissions is indicated by the color of the triangle. These photoelectrons emitted from the photocathode then move toward the microchannel plate (MCP) under the effect of an accelerating voltage. Before the photoelectrons reach the MCP, they have to pass through a pair of deflection electrodes. The scanning circuit applies a scanning voltage to the deflection electrodes, thus forming an electric field E between the scanning electrodes with the direction perpendicular to the main plane. The photoelectrons passing through the deflection electrodes will have a velocity and displacement along the y-direction under the action of the deflection electric field. Due to the different magnitudes of the scanning voltage at different instants, the electrons passing through the deflection electrodes at different instants will have different velocities and displacements in the y-direction. As shown in the figure, the electrons passing through the deflection electrode are distributed in three different planes along the y-direction. The deflection electrodes and the scanning circuit are the most important components that distinguish the streak camera from ordinary cameras. The function of the two is to convert the temporal information of the measured light radiation into spatial information. By changing the magnitude of the scanning voltage, the displacement of electrons along the y-direction when they reach the MCP can be controlled, i.e., the temporal information is converted into displacement in the y-direction. The variation of the scanning voltage with time is linear, with its maximum and minimum values corresponding to the arrival of electrons at the upper and lower boundaries of the MCP, respectively. Electrons are multiplied after passing through the MCP, making the measured signal significantly enhanced, which helps to improve the sensitivity of the streak camera. After multiplication, the electrons are accelerated by the electric field to bombard the fluorescent screen and produce visible light, which reaches the CCD camera through the coupled optical path. Finally, the CCD camera converts the light signal into an electrical signal and gets a digital image of the measured object through analog-to-digital conversion at the computer side, and the image obtained by the streak camera

is called the streak image in the following. The *x*-direction of the streak image still represents the spatial position along the slit, while the *y*-direction represents the time *t*, as shown in the coordinate diagram in the upper right corner. The total length of the streak image along the *y*-direction corresponds to the time from the minimum to the maximum of the scanning voltage, i.e., the scanning time. The shorter the scanning time, the shorter the time represented by each pixel point, i.e., the higher the temporal resolution. Therefore, the temporal resolution of the streak camera can be adjusted by changing the scanning time. Naturally, the size of the slit also affects the temporal resolution of the streak camera. The streak camera used in this work can detect wavelengths in the range of 200-850 nm, and its spatial resolution is better than 20 μm. The streak camera has five scanning times, namely 10 μs, 1 μs, 100 ns, 10 ns, and 1 ns. The operating mode of the streak camera described above is called dynamic mode. The streak camera can also turn off the scanning circuit and leave the slit completely open, which is called the static mode. The image obtained in the static mode is identical to that of a normal camera and is a 2D image without time resolution.

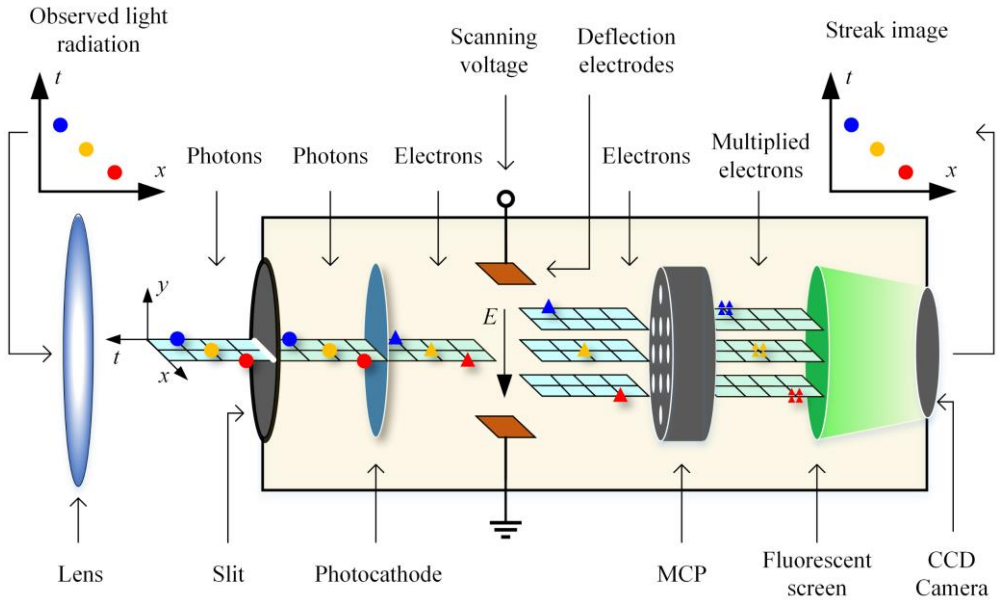

Figure 4-2 Schematic diagram of the structure and working principle of the streak camera

The experiments in this chapter still use the tip-plane electrode shown in Figure 2-4. In order to study the influence of the anode material on the instant of the anode glow appearance, six metals with very different physical properties were chosen as anodes, including aluminum (Al), chromium (Cr), copper (Cu), molybdenum (Mo), nickel (Ni) and tungsten (W), while brass was used uniformly as the cathode material. The relevant parameters of the anode materials are shown in Table 4-1. The gap lengths were chosen as 2.5 mm, 5 mm and 10 mm. The peak voltage was -40 kV or -30 kV with a pulse width of 5 μs. The corresponding steady-state arc current during breakdown was 80 A or 60 A, which was determined by the current limiting resistor (R_1=500 Ω). During the experiments, different anode materials, different gap lengths and different peak voltages were combined to obtain a total of 36 sets (6 × 3 × 2) of experiments with different conditions. Before the start of each set of experiments, the electrodes were replaced with brand new ones to exclude the influence of anode

surface contamination on the experimental results.

Table 4-1 Physical parameters of different anode materials relevant to the experiments in this chapter

	Al	Cr	Cu	Mo	Ni	W
Melting point / K	933	2133	1356	2890	1728	3643
Boiling point / K	2792	2944	2835	4912	3186	6173
Heat of fusion / $J \cdot g^{-1}$	386.9	293	204.8	293	305.6	184.2
Heat of vaporization / $J \cdot g^{-1}$	9462	5945	5234	5610	5862	4477
Specific heat capacity / $J \cdot kg^{-1} \cdot K^{-1}$	900	461	385	217	460	134
Thermal conductivity / $W \cdot m^{-1} \cdot K^{-1}$	210	69	398	138	60.7	163
Density / $kg \cdot m^{-3}$	2.69×10^3	7.18×10^3	8.96×10^3	1.02×10^4	8.90×10^3	1.93×10^4

Before the start of each vacuum breakdown experiment, a focusing operation is performed, during which the streak camera is set to the static mode. Figure 4-3 shows an image of a 5 mm tip-plane gap obtained in static mode, and the bright area in the image is the open slit, through which the electrode gap can be seen. The tip cathode is at the top, while the plane anode is at the bottom, and the spatial position of its surface is indicated by a white dashed line. Then, the slit is gradually reduced and the position of the streak camera is fine-tuned so that the tip cathode is always in the center of the slit. Eventually, the slit is reduced to 100 μm, in order to ensure both sufficient input light intensity and the highest possible temporal resolution. After the slit is adjusted, the streak camera is set to dynamic mode and the evolution of the light radiation during vacuum breakdowns is observed. The scanning time of the streak camera used are 10 μs and 1 μs. The total number of transverse pixels in the streak image is 2160, so the time resolution is 46 ns and 4.6 ns for scanning times of 10 μs and 1 μs, respectively.

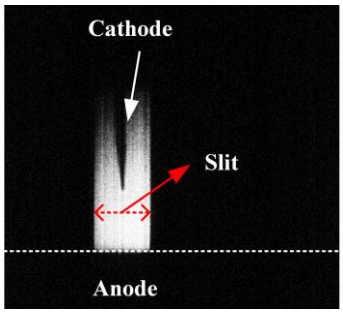

Figure 4-3 Image of the tip-plane gap obtained by the streak camera in static mode (5 mm gap length)

4.3 A WAVEFORM AND STRIPED IMAGE OF THE VACUUM BREAKDOWN PROCESS

Figure 4-4 shows the typical voltage and current waveforms of a vacuum breakdown a 5 mm gap. The anode material is copper, and the peak voltage is -40 kV. Figure 4-4(a) is the waveforms of the full breakdown process, while Figure 4-4(b) is a magnification of the initial breakdown stage. The gap voltage $u_g(t)$ and the measured current $i(t)$ are

represented by blue and red curves, respectively. The instant of breakdown onset is denoted by t_0 and is defined as a zero point, then the instants of the anode glow appearance and the conductive channel formation mentioned in this chapter are actually the delays with respect to the instant of breakdown initiation. The conductive channel is formed at t_{V0}, and the pulsed high-voltage source is turned off at t_E. The time duration of the current pulse in Figure 4-4(a) is about 5 μs, which corresponds to the pulse width set by the voltage source.

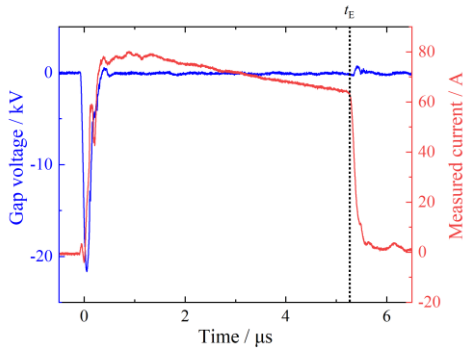

(a) Waveforms of the entire breakdown process

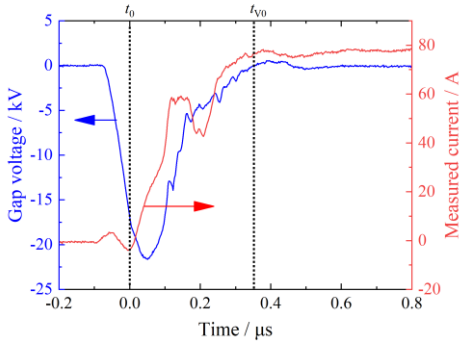

(b) Waveforms of the initial stage

Figure 4-4 Typical waveforms of the vacuum breakdown process

Figure 4-5 shows the current waveforms under different experimental conditions. To see more clearly the effect of the experimental conditions on the current waveform, only the waveforms during 0-1200 ns are shown. The variation trend of the current waveforms during this period can reflect the development of conductive channels. During the experiments, the current waveforms under all the experimental conditions were compared. However, for the sake of simplicity and intuitiveness, only partial results are given in Figure 4-5. The conditions include two gap lengths (2.5 mm and 10 mm), two peak voltages (-30 kV and -40 kV), and all anode materials (Al, Cr, Cu, Mo, Ni, and W). As shown in the figure, gap length and peak voltage have a significant effect on the trend of current waveforms in the initial stage of vacuum breakdown. The current rising in small gaps is significantly faster than that in large gaps, which means that conductive channels are established relatively quickly in small gaps. However, after the current rising phase, the current stabilizes at a value determined by the peak voltage and the current limiting resistor R_1, regardless of the gap length. That is, the gap current in the vacuum arc stage (P2, see Figure 2-10) is not affected by the gap size. On the other hand, by comparing the current waveforms corresponding to different anode materials, it can be found that the effect of the change of anode material

on the breakdown current waveforms can be ignored. Specifically, in the same gap length and the same pulse voltage, the current waveforms corresponding to all the different anode materials change almost exactly in the same trend. Considering significant differences in material properties (see Table 4-1), this means that anode materials have a very small impact on the establishment of conductive channels during vacuum breakdown.

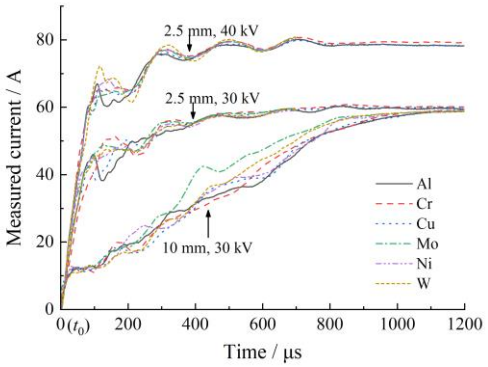

Figure 4-5 Current waveforms in the initial stage of vacuum breakdown under different conditions

Figure 4-6 shows a streak image of the vacuum breakdown process shown in Figure 4-4. The horizontal axis of the streak image represents the lapse of time rather than the spatial position, as shown by the principle of operation of the streak camera in Figure 4-2. In order to observe the evolution of the whole breakdown process, the scanning time of the streak camera is chosen to be 10 μs. Therefore, the total observation time corresponding to the full width of the image is 10 μs. The corresponding voltage and current waveforms are also attached, and the zero point of the time axis indicates the onset of the vacuum breakdown at t_0. The vertical axis of the streak image represents the spatial position along the gap axis, with the cathode tip and the anode surface at 0 mm and -5 mm, respectively. A schematic diagram of the tip-plane electrode structure and two dashed lines are also attached to the streak image to indicate the positions of the cathode and anode.

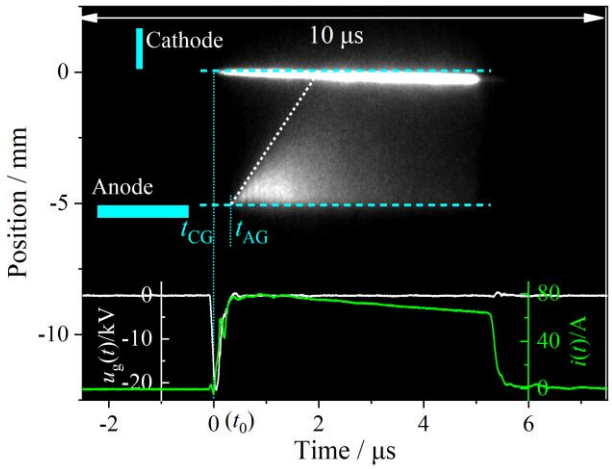

Figure 4-6 Streak image of the vacuum breakdown process in Figure 4-4 (10 μs scanning time, 5 mm gap, -40 kV peak voltage, copper anode)

As shown in Figure 4-6, the cathode glow appears at t_{CG}, which is almost identical to

t_0, meaning that the cathode glow appears immediately after the start of the vacuum breakdown. This is consistent with Figure 2-23 showing the development of the breakdown captured by the ICCD camera. The instant of the anode glow appearance in Figure 4-6 is defined as t_{AG}, which has a delay of about 300 ns with respect to t_{CG} (or t_0). That is, the instant of the anode glow appearance during the breakdown in a 5 mm vacuum gap is around 300 ns, which is also in agreement with the ICCD camera results (see Figure 2-23). Naturally, the expansion of the anode glow was also observed with the streak camera, and the variation of the anode glow boundary with time is marked with a white dashed line in the figure. According to the slope of the white dashed line, the expansion rate of the anode glow to the cathode can be roughly estimated at about 4000 m/s. The intensity of the anode glow also decays after a period of time, while the cathode glow is always present until the breakdown process ends after t_E. As can be seen in Figure 4-6, the duration of the cathode glow is also about 5 μs, which is consistent with the duration of the voltage pulse.

4.4 ANALYSIS OF THE PHYSICAL PROCESSES AT THE ANODE SURFACE

In the previous section, the electric waveforms and the streak image during the vacuum breakdown of a vacuum gap with a gap length of 5 mm and an anode material of copper were shown as an example. There is no doubt that these results are in perfect agreement with those obtained using the ICCD camera in Chapter 2. In the following, the physical process of the electrode corresponding to the anode glow during vacuum breakdown will be analyzed by comparing the delay of the anode glow at different gap lengths, anode materials, and peak voltages.

4.4.1 EFFECTS OF GAP LENGTH ON ANODE GLOW

Figure 4-7,Figure 4-8 and Figure 4-9 show the streak images when breakdown occurs in 2.5 mm, 5 mm and 10 mm gaps, respectively, and the waveforms are attached to the figures. The anode material is copper, and the peak voltage and pulse width are -40 kV and 5 μs. The positions of the cathode and the anode are marked with sketches and dashed lines in the figures. In order to improve the temporal resolution as much as possible, the scanning time of the streak camera was set to 1 μs when the gap length was 2.5 mm and 5 mm, as shown in Figure 4-7 and Figure 4-8. When the gap length is 10 mm, the instant of the anode glow may be close to or more than 1 μs. Therefore, the scanning time of the streak camera is set to 10 μs to ensure the accuracy of the obtained instant of emergence of the anode glow, as shown in Figure 4-9. In the three figures, the instants of the cathode glow appearance t_{CG} all coincides with the onset instants of vacuum breakdown t_0, while the anode glow always appears later than the cathode glow. When the gap length is 2.5 mm, 5 mm and 10 mm, the corresponding instants of the emergence of the anode glow t_{AG} are 171 ns, 331 ns and 972 ns. In other words, the delay of the anode glow relative to the cathode glow increases with the increase of the gap, which is consistent with the results in Table 2-2.

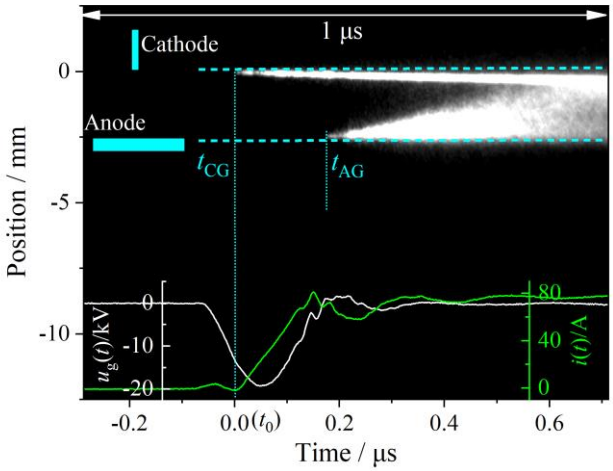

Figure 4-7 Streak image of the initial stage of vacuum breakdown: t_{AG}-t_{CG}=171 ns (1 μs scanning time, 2.5 mm gap, -40 kV peak voltage, copper anode)

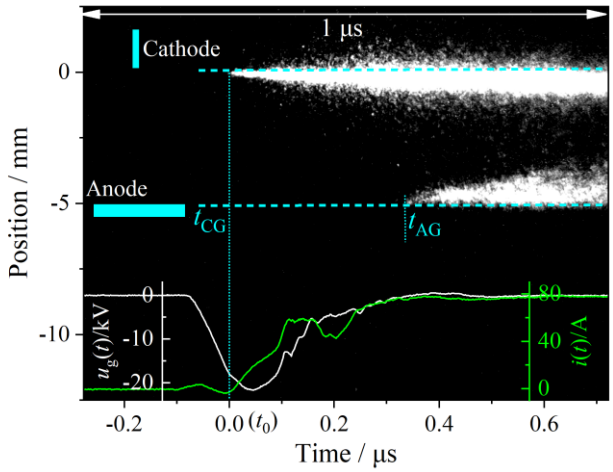

Figure 4-8 Streak image of the initial stage of vacuum breakdown: t_{AG}-t_{CG}=331 ns (1 μs scanning time, 5 mm gap, -40 kV peak voltage, copper anode)

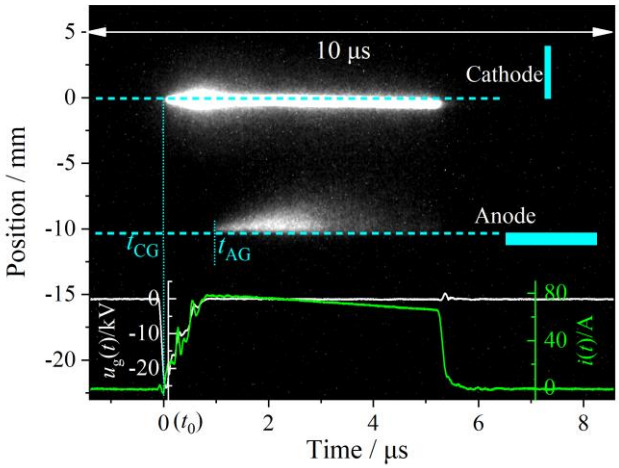

Figure 4-9 Streak image of the initial stage of vacuum breakdown: t_{AG}-t_{CG}=972 ns (10 μs scanning time, 10 mm gap, -40 kV peak voltage, copper anode)

Figure 4-7, Figure 4-8 and Figure 4-9 show the results of only one breakdown

experiment under the corresponding experimental conditions, respectively. In fact, due to the random nature of the vacuum breakdown process, there are some differences between the breakdown experiments even under the same conditions. The differences are reflected in the current waveform, the voltage waveform, the breakdown voltage, the instant of the cathode glow appearance, the instant of the anode glow appearance and the instant of the conductive channel formation. While illustrating the repeatability of the vacuum breakdown process, Figure 2-20, Figure 2-21 and Figure 2-22 also show the randomness of the breakdown process. In order to exclude the influence of randomness on the analysis of the results, the breakdown experiments were repeated 30 times under each experimental condition and then the results were statistically analyzed.

4.4.2 STATISTICAL ANALYSIS OF THE INSTANTS OF THE ANODE GLOW APPEARANCE UNDER DIFFERENT EXPERIMENTAL CONDITIONS

Figure 4-10 provide a comprehensive overview of the instants of the anode glow appearance for different anode materials under different experimental conditions. As mentioned earlier, the instant of the anode glow emergence is the delay of the anode glow relative to the cathode glow (or the onset of vacuum breakdown), t_{AG}-t_{CG}, which is calculated from a streak image similar to that in Figure 4-7. In Figure 4-10, all experimental conditions include combinations of six anode materials (Al, W, Cr, Cu, Mo, and Ni), two peak voltages (-30 kV and -40 kV), and three gap lengths (2.5 mm, 5 mm, and 10 mm), for a total of 36. The breakdown experiments were repeated 30 times for each experimental condition, and the results obtained were statistically analyzed to obtain the mean and standard deviation of the instants of the anode glow appearance. The data points in the figure indicate the mean value, while the error bars indicate the corresponding standard deviations. 2.5 mm, 5 mm and 10 mm gaps are represented by squares, circles and triangles, respectively. The solid and hollow symbols correspond to pulse voltages of -30 kV and -40 kV, respectively.

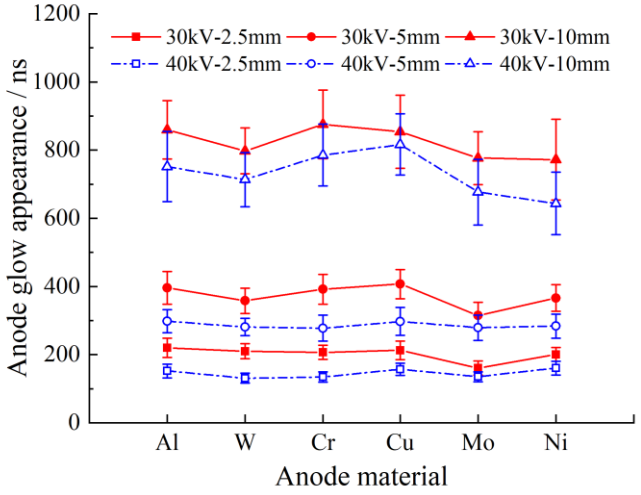

Figure 4-10 Comparison of the appearance of the anode glow under different experimental conditions

By comparing the instants of the anode glow emergence at different peak voltages, it can be found that the increase of the pulse voltage significantly reduces the delay of the anode glow relative to the cathode glow. This is because the higher voltage corresponds to a stronger gap current, and the stronger current is more favorable to the generation of the anode glow as the number of various microscopic particles moving with the cathode plasma toward the anode is higher. In addition, the effect of the change in the gap length on the instant of the appearance of the anode glow is more significant. With the increase of the gap length, the delay of the anode glow increases almost linearly.

However, the results in Figure 4-10 are somewhat surprising when comparing the instants of the anode glow for different anode materials. The unexpected thing is that the change in anode material does not have any significant effect on the instant of appearance of the anode glow. In fact, for the same gap length and applied voltage, the change in the average anode glow delay due to the change of the anode material is about 3% to 10%. In comparison, the ratio of the standard deviation of the anode glow delay to the mean value can reach between 8% and 15% even for 30 replicate experiments with the same material and the same experimental conditions. This means that the variation of the anode glow delay due to the change of the anode material does not exceed the fluctuation of the anode glow delay due to the randomness of the vacuum breakdown process. Intuitively, it can be seen from Figure 4-10 that the range of variation of the mean value of the instant of the anode glow appearance corresponding to various anode materials is within the error bars when the gap length and the externally applied voltage are kept constant. Therefore, from the experimental results in Figure 4-10, it can be concluded that the choice of the anode material has no significant effect on the anode glow delay. According to Table 4-1, the six anode materials used in the experiments have very large differences in parameters such as melting point and boiling point, and it is the differences in these parameters that make the results in Figure 4-10 appear somewhat unexpected.

As described in the beginning of this chapter, there are two possible mechanisms by which the atoms on the anode surface leave the anode and participate in the anode glow, including evaporation and sputtering mechanisms. The evaporation mechanism refers to the evaporation of the material on the anode surface because of the heating effect by the cathode plasma, while the sputtering mechanism refers to the sputtering caused by the heavy ions in the cathode plasma hitting the anode surface. The possibility of both mechanisms occurring on the anode surface under the current experimental conditions will be discussed separately below.

4.4.3 ROLE OF EVAPORATION AND SPUTTERING IN THE PROCESSES AT THE ANODE SURFACE

4.4.3.1 Evaporation mechanism

The evaporation mechanism has been considered in many studies as the main

mechanism for the appearance of the anode glow during vacuum breakdown [1, 36, 76, 81]. In the initial stage of vacuum breakdown, only a part of the vacuum gap is occupied by the expanding cathode plasma, while the remaining part of the gap still has a high potential difference, in this region with high voltage only electrons continuously moving toward the anode under the accelerating effect of the electric field. After the electrons reach the anode, their kinetic energy is converted into thermal energy, which heats the anode and makes the atoms on the anode surface evaporate, and the evaporated atoms are involved in the subsequent anode glow process. Taking a 5 mm gap and a gap voltage of 20 kV as an example, assuming constant acceleration of electrons in the gap, it can be estimated that the time required for electrons to reach the anode from the cathode is only 0.12 ns. In other words, the heating effect of electrons on the anode goes through the whole process of vacuum breakdown, especially before the formation of the conductive channel, the very high gap voltage makes the heating effect of electrons on the anode particularly obvious. In contrast, heavy particles (mainly ions) from the cathode can only strike the anode surface and produce sputtering when the expansion front of the cathode plasma reaches the anode, which takes several hundred nanoseconds. Therefore, the appearance of anode glow during vacuum breakdown is often considered to be the result of the evaporation of the anode surface under the heating effect of the electron flux from the cathode.

However, the comparative study of the different anode materials shown in Figure 4-10 do not seem to support evaporation mechanism for appearance of the anode glow. According to Table 4-1, the six anode materials used for the experiments in this chapter differ significantly in terms of their thermophysical parameters, and the delay of the anode glow relative to the cathode glow must exhibit a correlation with the choice of anode material if the main mechanism by which the atoms on the anode surface enter the anode glow region is evaporation. Therefore, the fact that the anode glow delay is not substantially affected by anode material change is intuitively contradictory to the evaporation mechanism.

In order to discuss more objectively whether the evaporation mechanism can explain the contribution of the atoms on the anode surface to the anode glow, the temperature of the anode surface and the density of metal vapor produced by the evaporation process will be estimated by solving the heat conduction equation in the following. Before solving the heat conduction equation for the anode, the energy density (in $W \cdot m^{-3}$) injected into the anode needs to be obtained first, i.e., the total power (in W) and the spatial distribution of the energy flux injected into the anode needs to be determined. The reason why the energy density units here use the power per unit volume is that the spatial distribution of the energy flux considers not only the radial (along the anode surface) distribution, but also the longitudinal distribution (perpendicular to the anode surface inward). Therefore, the energy flux injected into the anode is present in the form of a volumetric heat source in the heat transfer calculation of the anode.

The total power injected into the anode during vacuum breakdown can be estimated from the voltage and current waveforms. In the initial stage of vacuum breakdown, the conductive channel is not fully established, and most of the gap voltage is distributed between the cathode plasma boundary and the anode surface, causing the

electrons in this region to accelerate toward the anode. In this stage, the conduction current flowing through the gap is carried by the flow of electrons reaching the anode, so it can be assumed that most of the energy supplied to the gap by the external circuit is transferred to the anode by the electrons. In other words, in the initial stage of vacuum breakdown before the formation of the conductive channel, the total heat power of the electrons to the anode is approximately equal to the input power of the external circuit to the vacuum gap, i.e., the product of the gap voltage and the gap current ($u_g(t)\times i_g(t)$).

Figure 4-11 shows the voltage waveform of the vacuum breakdown and the corresponding input power of the external circuit to the gap, and the data in the figure are from the same breakdown experiment as in Figure 4-4. The input power to the gap is calculated using the gap voltage $u_g(t)$ and the gap current $i_g(t)$, and the gap current is calculated by Equation (2-1). As can be seen from the figure, after the start of vacuum breakdown, the input power of the external circuit to the gap undergoes a rising phase and a falling phase with a peak power of about 800 kW. After the formation of the conductive channel at t_{V0}, the vacuum breakdown enters the vacuum arc stage, where the input power to the gap is basically negligible compared to the previous peak power due to the significant reduction of the gap voltage. Strictly speaking, according to the vacuum arc theory, the gap voltage of the vacuum arc is mainly concentrated in the cathode sheath, and the energy provided by the external circuit to the gap is also mainly concentrated at the cathode spot, which is used to maintain the continuous generation of cathode plasma. The energy input from the arc to the anode is much smaller at this point. However, given that the total input power to the gap during the vacuum arc stage is also much less than the previous peak power, the power input to the anode during this stage (after t_{V0}) is not strictly calculated in the following, but the total input power to the gap is used as an approximation of the power input to the anode. Therefore, the total power injected into the anode is calculated using the following equation:

$$P(t)= u_g(t)\times i_g(t) \tag{4-1}$$

where $P(t)$ is the total power injected into the anode (in W); $u_g(t)$ is the gap voltage (in V); $i_g(t)$ is the gap current (in A), calculated by Equation (2-1).

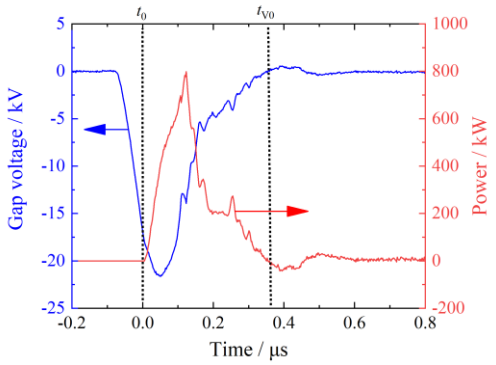

Figure 4-11 Gap voltage waveform and the input power of the external circuit to the gap corresponding to the vacuum breakdown process shown in Figure 4-4(copper anode, 5 mm gap, -40 kV peak voltage)

Both the radial (along the anode surface) and longitudinal (perpendicular to the anode surface inward) distributions of the energy flow into the anode during vacuum breakdown need to be considered. When estimating the radial distribution, the anode glow spot size on the anode surface is used as a reference. According to the images of the light radiation of the vacuum breakdown process shown in Figure 2-23 to Figure 2-25, the spot size on the anode surface and the gap length are approximately equal when the anode glow has just appeared. For example, the spot size at the anode surface in a 5 mm gap is 5.7 mm. Assuming that the energy flow into the anode satisfies a two-dimensional Gaussian distribution in the radial direction:

$$f(x,y)=\frac{1}{2\pi\sigma_1\sigma_2}\exp\left[-\frac{1}{2}\left(\frac{(x-\mu_1)^2}{\sigma_1^2}+\frac{(y-\mu_2)^2}{\sigma_2^2}\right)\right] \tag{4-2}$$

where (x, y) is spatial coordinates on the anode surface; $f(x, y)$ is the distribution function of the energy flow on the anode surface, whose two-dimensional spatial integration equals to 1; σ_1 is the distribution radius in the x direction, i.e. the standard deviation; σ_2 is the distribution radius in the y direction, i.e. the standard deviation; (μ_1, μ_2), is the spatial coordinates of the location for the peak power, i.e. the center point of the two-dimensional Gaussian distribution, which is also the center of the anode glow spot on the anode surface, and the position of the center will have some randomness during different breakdowns, see Figure 2-23. It is considered that the distribution of the energy flow in the x and y directions is exactly the same, i.e., $\sigma_1=\sigma_2=\sigma$, σ is referred to as the distribution radius below. According to the properties of Gaussian distribution, the probability that the values are distributed within [μ-3σ, μ+3σ] is 99.74%. Therefore, it is assumed that 6σ=5.7 mm≈ 6 mm for a gap length of 5 mm, i.e., the distribution radius σ of the energy flow is assumed to be 1 mm. Next, the value of this distribution radius (1 mm) will be used to calculate and demonstrate the distribution of the energy flow into the anode, while the reasonable range of the distribution radius σ will be discussed after the complete anode heat conduction model is introduced. Thus, the peak power density of the energy injected into the anode (i.e., the peak of the surface power density, $W(t)$, in W·m^{-2}) can be expressed by the following equation:

$$W(t)=P(t)f(\mu_1,\mu_2)=\frac{u_g(t)\times i_g(t)}{2\pi\sigma^2} \tag{4-3}$$

where $W(t)$ is actually the power density at the center (μ_1, μ_2) of the anode glow spot on the anode surface. Figure 4-12 gives the peak surface power density injected into the anode as a function of a time during the breakdown corresponding to Figure 4-4. The waveform of the gap voltage is still included in the figure to provide a temporal reference. The peak surface power density in this figure is calculated for a distribution radius σ of 1 mm, resulting in a maximum value of 1.27×10^{11} W·m^{-2} in time evolution.

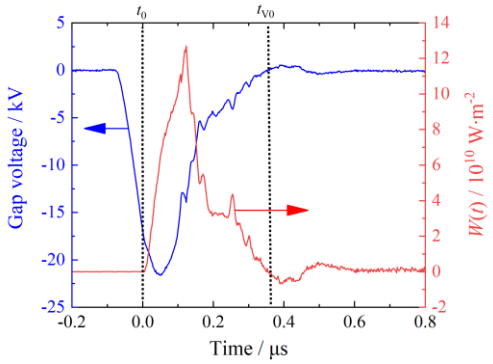

Figure 4-12 Gap voltage waveform and peak surface power density $W(t)$ of the energy flow into the anode corresponding to the vacuum breakdown process in Figure 4-4 (copper anode, 5 mm gap, -40 kV peak voltage, distribution radius σ being 1 mm)

As mentioned above, the energy injected into the anode comes mainly from the kinetic energy carried by the electrons entering the anode. As shown in Figure 4-11, before the formation of the conductive channel, the electrons are accelerated by the gap voltage towards the anode, so that the kinetic energy of the electrons reaching the anode surface can reach several tens of keV. The electrons with such high energy do not just reside on the anode surface, but can carry kinetic energy with them at a certain penetration depth inside the anode (hereinafter referred to as electron penetration depth, z_d), slowly dissipating the energy in the process of penetration into the anode, which causes heating of the anode. Therefore, the energy flow into the anode is considered as a volumetric heat source in the heat conduction calculation of the anode, and the corresponding unit is W·m^{-3}. Furthermore, in the following calculations, the rate of dissipation of the kinetic energy of electrons inside the anode is considered to be uniform, i.e., the loss of kinetic energy of electrons per unit penetration depth is constant. The electron penetration depth (zd) is estimated according to the Continuous Slowing Down Approximation (CSDA), and the corresponding results can be found in the ESTAR database[95]. Figure 4-13 shows the electron penetration depth (z_d) for different anode materials when the incident electron energy is in the range of 0-100 keV. It can be seen that the electron penetration depth in metals gradually increases with electron energy. In the gap voltage range covered in this paper, the electron penetration depths are in the order of microns. To ensure the stability of the numerical calculation, the penetration depth is forced to be 100 nm for electron energies below 1000 eV. The variation of the gap voltage and electron penetration depth z_d with time during a vacuum breakdown is given in Figure 4-14. The voltage waveform is taken from the breakdown process in Figure 4-4. The electron penetration depth is positively correlated with the magnitude of the gap voltage, which reaches a maximum of 1.86 μm during the breakdown process. Before the start of vacuum breakdown ($t<t_0$), the gap voltage is already high, but the electron current reaching the anode is very small, and the electron penetration depth at this stage is shown in the figure as 100 nm. It has no effect on the subsequent calculation of the anode heat conduction. This is because the total power $P(t)$ of the energy flow into the anode before t_0 is zero, and the adjustment of the penetration depth does not affect the density of the energy flow into the anode.

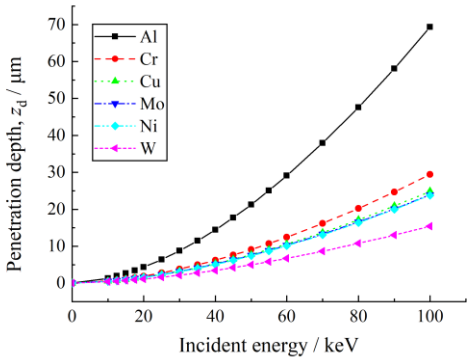

Figure 4-13 Variation of electron penetration depth z_d with incident energy for different anode materials

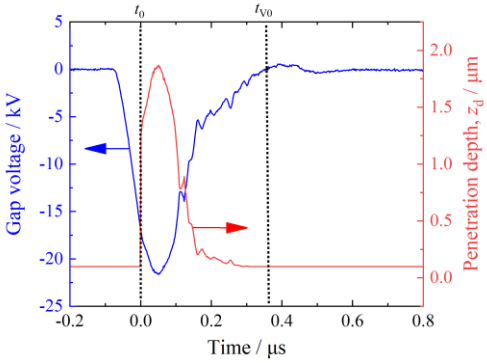

Figure 4-14 Voltage waveform and electron penetration depth z_d during vacuum breakdown corresponding to Figure 4-4

Through the above discussion, the peak surface power density $W(t)$ of the energy flow into the anode, i.e., the power density (in W·m^{-2}) at the center of the anode glow spot ($\mu1$, $\mu2$), and the electron penetration depth z_d (in m) have been obtained. Thus, the energy flow density on the axis through the spot center ($\mu1$, $\mu2$) can be calculated by the following equation:

$$Q(t)=\frac{W(t)}{z_d(t)}=\frac{P(t)}{2\pi\sigma^2 z_d(t)}=\frac{u_g(t)\times i_g(t)}{2\pi\sigma^2 z_d(t)} \tag{4-4}$$

where $Q(t)$ is the energy flow density on the axis through the center of the anode glow spot (μ_1, μ_2) (in W-m^{-3}), referred to as the central axis energy flux in the following. The variation of gap voltage and $Q(t)$ with time for a vacuum breakdown is given in Figure 4-15. The voltage waveform is taken from the breakdown in Figure 4-4. As can be seen from the figure, $Q(t)$ peaks at 2.81×10^{17} W·m^{-3} between t_0 and t_{V0}. After the formation of the conductive channel ($t>t_{V0}$), $Q(t)$ appears negative due to the oscillation of the gap voltage, but it is practically impossible for the electrons to deliver negative energy to the anode. Therefore, during the calculation, the negative energy injected into the anode is forced to be 0.

To intuitively illustrate the several physical quantities related to the energy flow into the anode mentioned above, including the total power $P(t)$ (in W) of the injected energy, the peak surface power density $W(t)$ (in W·m^{-2}) and the central axis energy flux $Q(t)$ (in W·m^{-3}), a schematic diagram of the anode heating process during vacuum

breakdown is given in Figure 4-16. As shown in Figure 4-16(a), $P(t)$ is basically equal to the input power of the external circuit to the vacuum gap $u_g(t) \times i_g(t)$. This energy flow is not uniformly distributed on the anode surface, but satisfies the two-dimensional Gaussian distribution as in Equation (4-2). The surface power density reaches its maximum $W(t)$ at the center of the two-dimensional Gaussian distribution ($x=\mu_1$, $y=\mu_2$), as shown in Figure 4-16(b). Since the high-energy electrons have a certain penetration depth z_d in the anode, the energy flow reaching the anode surface is in turn distributed in the direction perpendicular to the surface to a certain depth range ($0<z<z_d$) inside the anode, as shown in Figure 4-16(c).

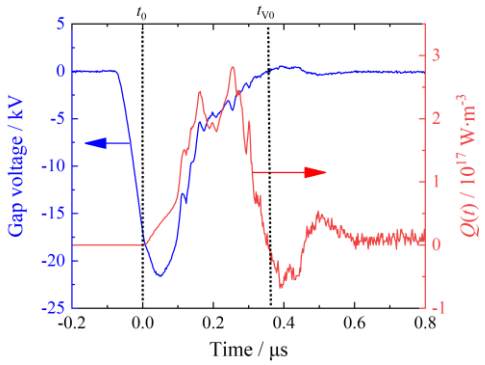

Figure 4-15 Voltage waveforms and central axis energy flux Q(t) during vacuum breakdown corresponding to Figure 4-4 (copper anode, 5 mm gap, -40 kV peak voltage, distribution radius of the injected energy σ being 1 mm)

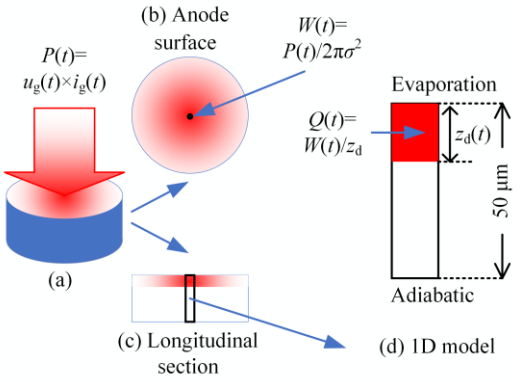

Figure 4-16 Schematic diagram of the anode heating process during vacuum breakdown: (a) three-dimensional illustration of the anode heating; (b) energy flow distribution on the anode surface; (c) energy flow distribution on the anode longitudinal section; (d) one-dimensional anode heat conduction model obtained by abstracting from the central axis of the energy flow

As can be seen from Figure 4-14, the electron penetration depth z_d inside the anode during vacuum breakdown does not exceed a few microns, while the distribution radius σ of the heat flow on the anode surface is in the order of millimeters. This suggests that the anode heat conduction process is more significant in the direction perpendicular to the anode surface, so the process can be abstracted as a one-dimensional model along the vertical direction, as shown in Figure 4-16(d). Since the purpose of solving the anode heat conduction equation is to obtain the maximum temperature and maximum vapor density on the anode surface, the location of the one-dimensional heat conduction model is chosen to be on the central axis of the injected

energy, i.e., a line through ($x=\mu_1$, $y=\mu_2$) and perpendicular to the anode surface. The one-dimensional heat conduction equation can be written in the following form:

$$\rho C_v \frac{\partial T}{\partial t} = \kappa \frac{\partial^2 T}{\partial z^2} + p(z) \tag{4-5}$$

where ρ is the density of anode material (in $kg \cdot m^{-3}$); C_v is the heat capacity of anode material (in $J \cdot kg^{-1} \cdot K^{-1}$); T is temperature of anode (in K); t is the time variable (in s); z is the depth from the anode surface (in m); κ is the thermal conductivity of anode material (in $W \cdot m^{-1} \cdot K^{-1}$); $p(z)$ is the energy flow density deposited inside the anode as a function of the depth z (in $W \cdot m^{-3}$). When $0<z<z_d$, $p(z)=Q(t)=W(t)/z_d$, while for $z>z_d$, $p(z) = 0$.

As shown in Figure 4-16, the length of the computational region of the one-dimensional heat conduction model for the anode is 50 μm, with the anode surface (z=0) at the upper end and a point inside the anode (z=50 μm) at the lower end. The model considers the volumetric heat source $p(z)$, heat conduction, latent heat of melting, and energy loss due to evaporation. The upper boundary of the model uses a heat flux boundary to describe the energy loss due to evaporation, and the lower boundary is set as an adiabatic boundary (the rationality for the adiabatic boundary will be explained later). The heat flux removed by evaporation from the anode surface is calculated using the equation:

$$q_{ev} = \frac{L_{ev}}{N_A} \phi \tag{4-6}$$

where q_{ev} is the energy loss of evaporation (in $W \cdot m^{-2}$); L_{ev} is evaporative heat (in $J \cdot mol^{-1}$); N_A is Avogadro constant, 6.02×10^{23} mol^{-1}; ϕ is evaporation rate (in $m^{-2} \cdot s^{-1}$) calculated as follows:

$$\phi = \frac{p_{sat}}{\sqrt{2\pi k m T}} \tag{4-7}$$

where k is Boltzmann constant, 1.38×10^{-23} $J \cdot K^{-1}$; m is atomic mass (in kg); p_{sat} is saturated vapor pressure of anode material (in Pa), calculated by the Clausius-Clapeyron equation as follows:

$$p_{sat} = p_{atm} \exp\left[-\frac{L_{ev}}{R}\left(\frac{1}{T} - \frac{1}{T_b}\right)\right] \tag{4-8}$$

where p_{atm} is atmospheric pressure, 1.01×10^5 Pa; R is ideal gas constant, 8.314 $J \cdot mol^{-1} \cdot K^{-1}$; T_b is boiling point of material (in K).

The heat conduction model in Equation (4-5) was solved using Comsol software. The grid size of the model is 100 nm, which is consistent with the minimum electron penetration depth. The initial temperature of the anode is set to 300 K. The model calculates the temperature change of the anode during 700 ns from the breakdown onset instant t_0, and the time step is set to 1 ns. Since the input power of the external circuit to the gap and the gap voltage are time-dependent, as in Figure 4-11, the electron penetration depth z_d and the central axis energy flux $Q(t)$ need to be obtained

according to Figure 4-13 and Equation (4-4), respectively, before each calculation step.

Figure 4-17 gives the anode temperature distribution as a function of time during a vacuum breakdown obtained by the above one-dimensional heat conduction model. The input data for the model are taken from the voltage and current waveforms in Figure 4-4, corresponding to the experimental conditions: 5 mm vacuum gap, -40 kV peak voltage, 5 μs pulse width and copper anode. The results of this figure were obtained under the assumption that the distribution radius σ of the energy flow on the anode surface is equal to 1 mm. The horizontal axis of Figure 4-17 represents the distance of the position inside the anode from the anode surface, with position 0 being the anode surface, while the vertical axis shows the temperature values at each spatial position. The temperature distribution at different instants (with respect to the start of breakdown at t_0) is shown in five different curves. Before the start of breakdown, the temperature of the anode is equal to the ambient temperature (300 K). After the onset of breakdown, the energy flow into the anode increases rapidly (see Figure 4-15), causing the temperature near the anode surface to rise rapidly. About 300 ns after the onset of breakdown, the temperature at the anode surface reaches a maximum value of 1400 K. Since then, the energy flow into the anode starts to drop (see Figure 4-15), and the energy gradually expands from the anode surface to the anode interior, causing the temperature at the anode surface to gradually decrease while the temperature inside the anode gradually increases. As the energy expands inside the anode, the spatial distribution of temperature tends to flatten out, as shown in the curve at 700 ns in Figure 4-17. The temperature gradient at the lower boundary of the model (50 μm position) is always zero during the 700 ns calculation time, which means that the heat flux through this boundary is zero. Therefore, it is a reasonable assumption to set the lower boundary of the 1D heat conduction model as an adiabatic boundary condition (see Figure 4-16(d)).

According to Figure 4-17, although the temperature distribution inside the anode changes with time, the temperature at the anode surface is always the highest. That is, the center of the distribution of the energy flow at the anode surface ($x=\mu_1$, $y=\mu_2$) is where the maximum anode temperature is located. Knowing the anode surface temperature, the evaporated atom number density (n^{ev}) near the anode surface can be calculated from the saturation vapor pressure and the ideal gas equation, as follows:

$$p_{sat}=n^{ev}kT_s \tag{4-9}$$

where T_s is the temperature of the anode surface (in K).

Before calculating the evaporated atom number density near the anode surface under different experimental conditions, a reasonable range of the distribution radius σ of the energy flow is discussed. According to the microscopic morphology of the anode surface after the experiment in Section 2.6.2, the copper anode did not melt significantly during the breakdown of the 0.5 mm-5 mm gap. Therefore, a reasonable range of the distribution radius σ can be estimated by calculating the maximum temperature of the anode surface at different distribution radii σ. Figure 4-18(a) and (b) shows the variation of the maximum temperature at the anode surface with the

distribution radius σ of the energy flow for gap lengths of 2.5 mm and 5 mm, respectively. The solid line in the figure indicates the maximum temperature at the anode surface and the dashed line indicates the melting point of copper (1356 K). As the distribution radius decreases, the density of energy flow into the anode increases, resulting in a corresponding increase in the temperature of the anode surface. Based on the fact that the anode surface has not melted, it can be deduced that: at 2.5 mm gap, the distribution radius must not be less than 0.9 mm, and at 5 mm gap, the distribution radius must not be less than 1 mm. According to the observation of the anode glow in Chapter 2, the spot size of the anode glow on the anode surface increases linearly with the gap length (see Figure 2-23, Figure 2-24 and Figure 2-25). Therefore, it is reasonable to believe that the distribution radius of the injected energy into the anode will also increase significantly with the increase of the gap length. In other words, for a gap length of 5 mm, the distribution radius on the anode surface is likely to reach 2 mm (greater than 2 × 0.9 mm). In addition, according to the results in Section 2.6.2, no significant melting is observed on the anode surface even at a gap length of 0.5 mm, which indicates that the above estimates of the distribution radius in the 2.5 mm and 5 mm gaps may still be lower than the actual value. In other words, the actual distribution radius of the injected energy flow may be larger.

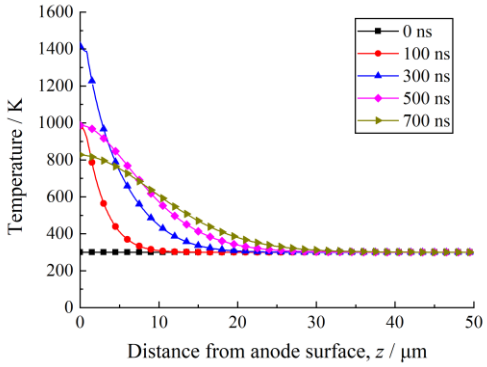

Figure 4-17 Variation of anode temperature distribution with time during vacuum breakdown (copper anode, 5 mm gap, -40 kV peak voltage, distribution radius σ being 1 mm)

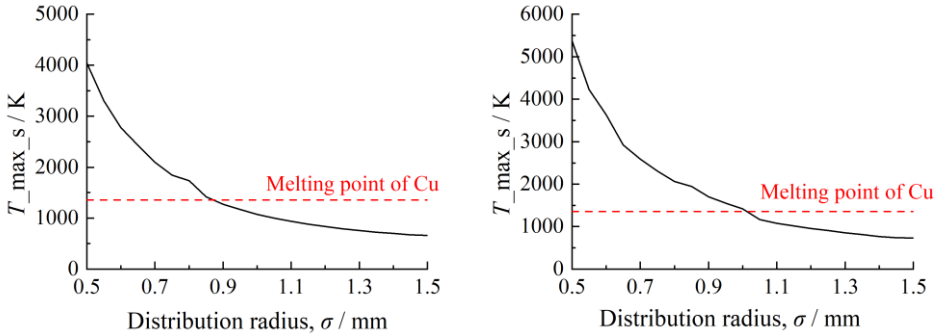

(a) 2.5 mm gap (b) 5 mm gap

Figure 4-18 Maximum temperature of the anode surface for different distribution radii σ (copper anode, -40 kV peak voltage)

Next, the maximum surface temperature and the evaporated atom number density n^{ev} for the anodes of different materials during vacuum breakdown will be discussed under one of the experimental conditions in this chapter (5 mm gap and -40 kV peak

voltage). Figure 4-19(a)-(d) present the variation of the maximum surface temperature of the anode and the evaporated atom number density n^{ev} with time for the distribution radius σ of 1 mm and 2 mm, respectively, with the time zero indicating the onset instant of vacuum breakdown t_0. Each subplot contains six curves representing six different anode materials, each obtained by averaging the results of 30 experiments under the same conditions. As shown in Figure 4-19(a) and (b), both the maximum anode surface temperature and the evaporated atom number density n^{ev} rise to their peak 200-300 ns after the onset of breakdown when the distribution radius σ=1 mm, after which both values start to decrease rapidly. In both plots, a strong correlation is observed for the anode surface temperature and the evaporated atom number density with the choice of material. The value of the maximum surface temperature is smaller compared to the other materials when the anode material is copper, which is due to the better thermal conductivity of copper, allowing a faster conduction of heat to the inside of the anode. The differences in the evaporated atom number density corresponding to the different anode materials are even more pronounced: the chromium (Cr) anode has the highest evaporated atom number density (4.83×10^{22} m^{-3}), which is about 11 orders of magnitude higher than that of the tungsten (W) anode (6.03×10^{11} m^{-3}). In addition, the maximum evaporated atom number densities are 6.03×10^{11} m^{-3} and 3.17×10^{16} m^{-3} for tungsten (W) and molybdenum (Mo) anodes, respectively, which are even lower than the atom number density of the residual gas in the vacuum chamber where the experiments were conducted (gas density of about 6.04×10^{16} at a pressure of 2.5×10^{-4} Pa and a temperature of 300 K).

According to Figure 4-19(c) and (d), when the distribution radius σ is set to a more reasonable value of 2 mm, the maximum anode surface temperature and the evaporated atom number density n^{ev} both undergo a significant decrease. The maximum evaporated atom number density corresponding to all anode materials at this time does not exceed 1×10^{7} m^{-3}, and such a low evaporated atom number density is unlikely to produce anode glow. Even if the distribution radius is as small as 1 mm, the evaporated atom density of tungsten and molybdenum still does not support the generation of anode glow. However, the anode glow phenomenon was observed near the anode surface when all the different anode materials were used. Furthermore, if all atoms in the anode glow region are evaporated from the anode surface, the large differences in the number density of evaporated atoms corresponding to different materials would also lead to large and stable differences in the anode glow delay. This is in contradiction with the small differences in anode glow delays for different anode materials in Figure 4-10. Based on these two contradictions between the experimental and computational results, the process of atoms leaving the anode surface and participating in the anode glow cannot be reasonably explained by the evaporation mechanism. In other words, under the experimental conditions of this dissertation, the bombardment and heating of the anode surface by the electron flow from the cathode cannot explain the phenomenon of a large number of atoms leaving the anode surface and participating in the anode glow.

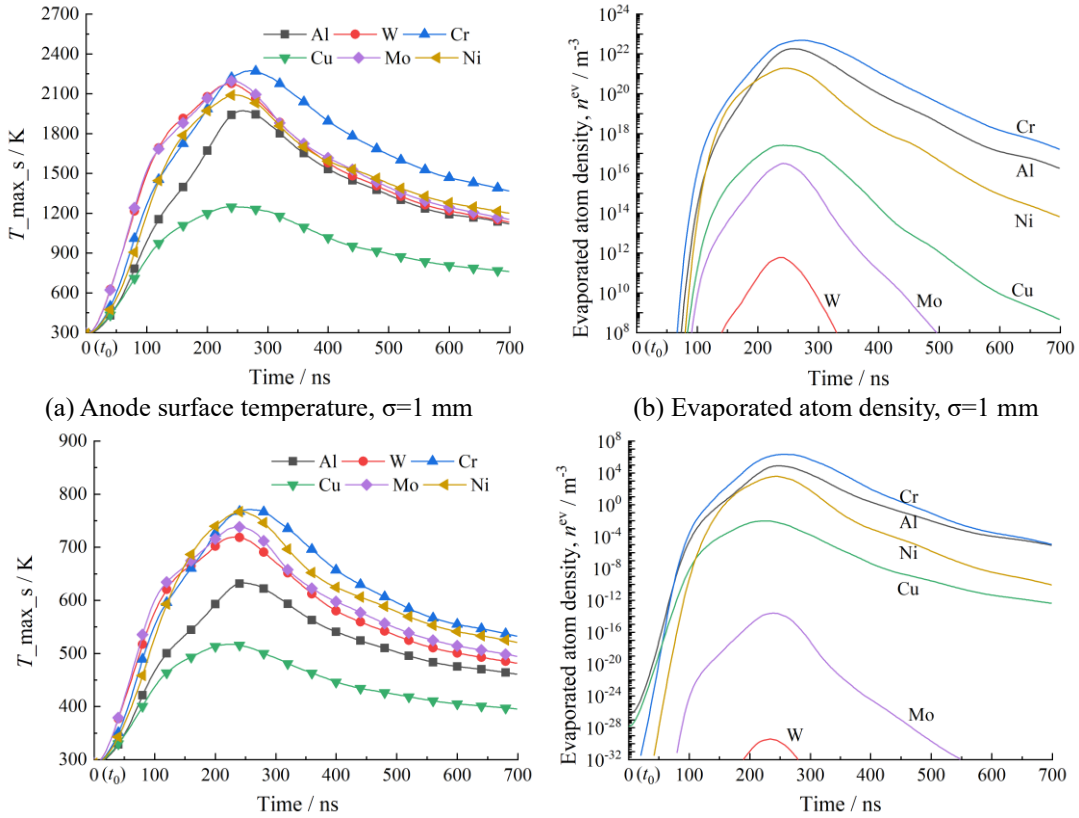

(a) Anode surface temperature, σ=1 mm (b) Evaporated atom density, σ=1 mm

(c) Anode surface temperature, σ=2 mm (d) Evaporated atom density, σ=2 mm

Figure 4-19 Maximum anode surface temperature and evaporated atom number density n^{ev} as a function of time during vacuum breakdown (5 mm gap, -40 kV peak voltage)

4.4.3.2 Sputtering mechanism

Since the evaporation mechanism cannot reasonably account for the anode composition in the anode glow, the next step is to discuss whether the sputtering mechanism is feasible. The sputtering of atoms on the anode surface requires bombardment by heavy particles from the cathode, where the main heavy particles considered are the positive ions in the cathode plasma. Since the cathode used in the experiments of this chapter is a brass needle, the ions incident on the anode surface are mainly copper ions. According to the spectral results of the anode glow in Chapter 3, both the atoms from the cathode and the atoms from the anode contribute to the anode glow during the breakdown, and the anode glow already contains the spectral components of the cathode material just as it appears. This indicates that ions from the cathode material have already reached the anode surface by the time the anode glow appears, and these cathode ions that reach the anode surface may then bombard the anode surface and produce sputtering of atoms from the anode material. In order to verify the sputtering mechanism, the following parameters need to be obtained: the velocity of the cathode material ions moving toward the anode, the sputtering yield of the cathode ions bombarding the anode material, the cathode ion flux, and the distribution of the cathode ion flux on the anode surface.

Firstly, the velocity of ions moving from the cathode to the anode is estimated.

According to Figure 4-10, there is an approximately linear relationship between the anode glow delay and the gap length, indicating that the motion of the ions from the cathode to the anode is essentially at a constant speed. This has also been confirmed in the work of other researchers[84, 86, 90-93]. Based on the ratio between the gap length and the instant of the anode glow appearance, the velocity of the ions can be roughly estimated to be between 12000 m/s and 20000 m/s. In some experimental and theoretical studies, the ion velocity also reached this range[84, 86, 90-93]. Such a high ion velocity corresponds to a high enough kinetic energy which can cause the neutral atoms on the anode surface to sputter and leave the anode surface. The bombardment of the anode surface by cathode ions was simulated using the Binary Collision Approximation (BCA) code SRIM[96], and the sputtering yield and the average energy of the sputtered atoms were calculated for different anode materials. Since the appearance of the anode glow requires the accumulation of particles to a certain concentration, the instant of the arrival of the cathode ions at the anode must be earlier than the instant of the anode glow appearance (under the assumption of the sputtering mechanism). Therefore, in all simulations, the velocity of copper ions is set to 20000 m/s, corresponding to an incident energy of 132 eV. The calculated sputtering yield, average energy ($\langle E\rangle_{sp}$) and average velocity of sputtered atoms ($\langle v\rangle_{sp}$) are shown in Table 4-2.

Table 4-2 Sputtering rate (Y), average energy of sputtered atoms ($\langle E\rangle_{sp}$) and average velocity of sputtered atoms ($\langle v\rangle_{sp}$) for different anode materials

Anode material	Al	W	Cr	Cu	Mo	Ni
Sputtering yield Y	0.12	0.44	0.21	0.62	0.4	0.35
Average energy $\langle E\rangle_{sp}$/ eV·atom^{-1}	4	22.9	6.5	7.7	21.4	7.4
Average speed $\langle v\rangle_{sp}$/ m·s^{-1}	5349	4904	4912	4836	6562	4933

According to previous measurements, the ion current corresponding to the flow of ions from the cathode to the anode during the steady-state vacuum arc accounts for 8%-12% of the total gap current[97, 98]. In the experiments of this chapter, the evolution of vacuum breakdown is close to the vacuum arc stage when ions from the cathode reach the anode (or when the anode glow appears) (see Section 4.5), so the ion current reaching the anode surface is assumed to be 10% of the total gap current $i_g(t)$. When the peak pulse voltage is set to -40 kV, the gap current in the vacuum arc stage is 80 A. Then the ion current I_{ion} can be roughly estimated as 8 A. Assuming that the distribution of the ion flow on the anode surface is the same as the distribution of the electron flow, i.e., it satisfies the two-dimensional Gaussian distribution in Equation (4-2). Still taking a vacuum gap of 5 mm as an example, the distribution radius σ of the ion current is taken as 1 mm or 2 mm. the maximum ion flux reaching the anode surface can be estimated by the following equation:

$$F_{ion}=\frac{I_{ion}}{Ze}\frac{1}{2\pi\sigma^2} \tag{4-10}$$

where F_{ion} is the maximum flux of the cathode ion flow reaching the anode surface (in m^{-2}·s^{-1}); Z is the average charge of the ions, about 2 in the vacuum arc; σ is the distribution radius of cathode ion flow on the anode surface, 1 mm or 2 mm.

For a gap current of 80 A and a distribution radius of 1 mm, $F_{ion}=3.98\times10^{24}$ $m^{-2}\cdot s^{-1}$. The density of sputtered atoms produced on the anode surface, n^{sp} (in in m^{-3}), can be further calculated by the following equation:

$$n^{sp}=\frac{F_{ion}Y}{v_{sp}} \tag{4-11}$$

Where Y and v_{sp} are the sputtering yield and average velocity of the sputtered atoms as shown in Table 4-2.

In order to produce detectable anode glow, as shown in Figure 4-6, the atom number density near the anode must be sufficiently high. The time required to establish a high atom number density will determine the delay of the anode glow with respect to the cathode glow.

Table 4-3 compares the sputtered atom number density (n^{sp}) and evaporated atom number density (n^{ev}) produced for different anode materials with one of the experimental conditions (5 mm gap and -40 kV peak voltage) as an example. When the distribution radius of the ion and electron flows on the anode surface is 1 mm, the sputtered atom number density (n^{sp}) from the anode surface of different materials are all around 10^{20} m^{-3}, with a small difference of not more than one order of magnitude from each other. Under this condition (σ=1 mm), the evaporated atom number density has a higher value when the anode materials are Al, Cr and Ni, while the sputtered atom number density has a higher value for W, Cu and Mo anodes. When the distribution radius is increased from 1 mm to 2 mm, the sputtered atom number density decreases to 1/4 of the original one, which is due to the fact that the maximum flux of the ion flow on the anode surface is reduced to 1/4 of the original one, as shown in Equation (4-10). In contrast, the decrease in the evaporated atom number density is dramatic, with that corresponding to the tungsten anode even decreasing to 10^{-30} m^{-3}. According to the relevant discussion in Figure 4-18, reasonable values of the distribution radius of the electron and ion streams on the anode surface are likely to be above 2 mm (5 mm gap), in which case the value of the evaporated atom number density is unlikely to produce anode glow, while the density level of the sputtered atoms (three orders of magnitude higher than the residual gas density of the vacuum cavity) is still within the range where anode glow can be produced. In addition, the sputtered atom number density produced by the different anode materials is essentially of the same order of magnitude, a fact that is also consistent with the proximity of the instants of the anode glow appearance for the various materials in Figure 4-10. Thus, sputtering from the anode surface under the bombardment of cathode ions is the main mechanism for the escape of anode atoms from the anode surface, and this mechanism provides a large number of atoms for the production of the anode glow. This finally results in the presence of significant spectral signals from the anode surface material (both the native anode material and the material in the contamination layer of the cathode material) in the anode glow, as shown by the results in Chapter 3.

Table 4-3 Comparison of sputtered atom number density (n^{sp}) and evaporated atom number density (n^{ev}) produced by different anode materials (5 mm gap and -40 kV peak voltage, assuming that both electron and ion flows on the anode surface satisfy the Gaussian distribution in Equation (4-2) with a distribution radius of 1 mm or 2 mm)

Anode material	Al	W	Cr	Cu	Mo	Ni
$n^{sp}_{\sigma=1mm}$ / m^{-3}	8.93×10^{19}	3.57×10^{20}	1.70×10^{20}	5.10×10^{20}	2.43×10^{20}	2.82×10^{20}
$n^{ev}_{\sigma=1mm}$ / m^{-3}	1.82×10^{22}	6.03×10^{11}	4.83×10^{22}	2.58×10^{17}	3.17×10^{16}	1.91×10^{21}
$n^{sp}_{\sigma=2mm}$ / m^{-3}	2.23×10^{19}	8.93×10^{19}	4.25×10^{19}	1.27×10^{20}	6.07×10^{19}	7.06×10^{19}
$n^{ev}_{\sigma=2mm}$ / m^{-3}	7.82×10^{4}	3.90×10^{-30}	2.15×10^{6}	9.62×10^{-3}	2.41×10^{-14}	3.81×10^{3}

4.5 RELATIONSHIP BETWEEN ANODE GLOW APPEARANCE AND CONDUCTIVE CHANNEL FORMATION

As shown in Figure 4-4 and Figure 4-6, the evolution of the vacuum breakdown process is accompanied by the continuous change of the electrical and optical radiation signals, both of which reflect the state of the vacuum breakdown in terms of the gap conductivity and the particle spatial distribution, respectively. Once the vacuum breakdown starts ($t>t_0$), the gap current gradually rises and the voltage gradually decreases, reflecting the transition of the gap from an insulating to a conducting state. When the gap voltage drops to zero ($t=t_{V0}$), a complete conductive channel is established in the gap. The establishment of the conductive channel requires in turn particles from the cathode and anode as the medium, so there is a close connection between the electrical and optical radiation signals during breakdown. For example, the emergence of the cathode glow and the onset of the breakdown process are essentially synchronized ($t_0\approx t_{CG}$), implying that the initiation and development of breakdown requires the establishment of the cathode plasma as a prerequisite. On the issue of the relationship between the anode glow and breakdown development, many previous researchers have observed that the instant when the gap voltage drops completely coincides with the instant when the anode glow conjoins the entire gap[1, 53, 76, 81]. Therefore, they believe that the appearance of the anode glow and its expansion toward the cathode during vacuum breakdown is a necessary condition for the formation of a fully conductive channel in the gap. However, after the study in Chapter 2, it is found that the expansion of the anode glow does not play a decisive role in the formation of the conductive channel. In other words, the expansion of the anode glow and its connection across the gap is not a necessary condition for the conductive channel formation, and the establishment of the conductive channel is most likely the result of the cathode plasma expansion. The discussions in Chapters 3 and 4 indicate that ions from the cathode are indeed able to expand across the dark gap

toward the anode before the anode glow appears. Both electrons and ions in the cathode plasma move toward the anode, indicating that the cathode plasma is expanding toward the anode. The discussion in the previous section illustrates that the emergence of the anode glow is the result of the interaction of the ions in the cathode plasma with the anode surface. Since the formation of the conductive channel during breakdown and the appearance of the anode glow are both the result of the expansion of the cathode plasma to the anode, what relationship exists between the two?

Based on the light radiation signal obtained by the ICCD camera, the second and fourth columns of Table 2-2 compare the instants of the anode glow appearance and the conductive channel formation. According to this comparison, the anode emission appears earlier than the formation of the conductive channel, but the time difference is comparable to the exposure time of the camera. In addition, due to the frame rate limitation of the ICCD camera, there are only a few images near the instant of the anode glow emergence. Therefore, the comparison in this table does not reflect well the relationship between the anode glow appearance and the conductive channel formation in terms of time. The streak camera used in this chapter records the continuous time evolution of the breakdown process, and there are 30 results for each experimental condition. The statistical analysis of the experimental results obtained in this chapter can reflect more accurately the relationship between the appearance of the anode glow and the formation of the conductive channel.

Figure 4-20 shows the comparison between the instants of the anode glow appearance and the conductive channel formation under different experimental conditions. Figure (a) shows the results for a peak voltage of -30 kV, while Figure (b) shows the results for a peak voltage of -40 kV. Both figures use hollow symbols and dashed lines to indicate the instant of the anode glow appearance (the delay t_{AG}-t_0) and use the solid symbols and solid lines to indicate the instant of the conductive channel formation (the delay t_{V0}-t_0). The data points in the graph are the mean of the 30 results for each experimental condition, while the error bars indicate the corresponding standard deviations. As shown in the figure, the appearance of the anode glow and the establishment of the conductive channel are very close in time. At higher applied voltages and shorter gaps, the appearance of the anode glow is slightly earlier than the formation of the conductive channel, i.e., $t_{AG}<t_{V0}$ (see the time delay corresponding to the gaps of 2.5 mm and 5 mm in Figure 4-20(b)). When the applied voltage is small, as in the delay corresponding to the gaps of 2.5 mm and 5 mm in Figure 4-20(a), the appearance of the anode glow tends to be later than the establishment of the conductive channel.

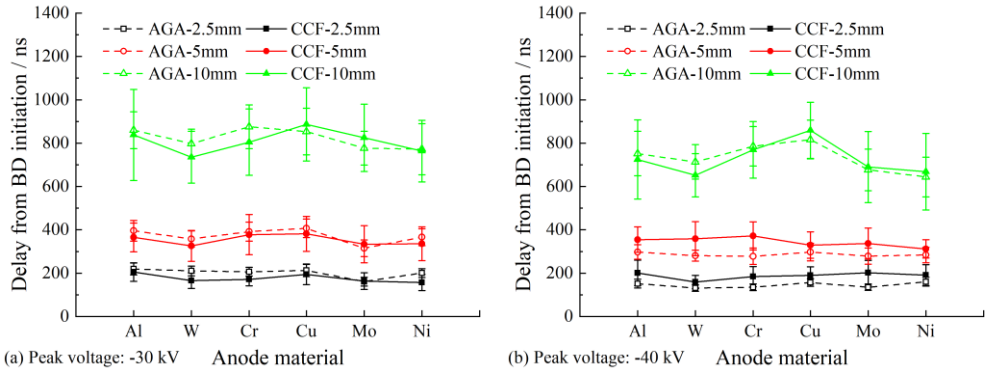

Figure 4-20 Comparison of the instants of the anode glow appearance and the conductive channel formation under different experimental conditions

Then, the data in Figure 4-20 were regrouped and replotted in Figure 4-21 and used to analyze the effects of the peak voltage on the instants of the anode glow appearance (Figure 4-21(a)) and the conductive channel formation (Figure 4-21(b)). Analysis of the data in the figure shows that increasing the peak voltage (i.e., increasing the gap current) significantly reduces the delay in the appearance of the anode glow, but has little effect on the delay required for the formation of the conductive channel. This phenomenon is more pronounced in the 2.5 mm and 5 mm gaps. The increases in pulse voltage and gap current imply a rise in the flux of charged particles in the vacuum gap, which has a facilitating effect on both the anode glow appearance and the conductive channel formation. However, according to the comparison in Figure 4-21, the dependence of the anode glow on the particle flux is more significant. This is because the appearance of the anode glow requires the particle density near the anode surface to accumulate to a certain threshold, while the formation of the conductive channel only requires the expanding cathode plasma to reach the anode surface. This also shows once again that the anode glow is a secondary effect of the cathode plasma expansion, while the appearance of the anode glow does not contribute significantly to the construction of the conductive channel. In addition, the result that the delay required for the conductive channel formation is less affected by the pulse voltage and the gap current also indicates that the expansion velocity of the cathode plasma is little dependent on the magnitude of the gap current, which is also consistent with the results in the literature[91].

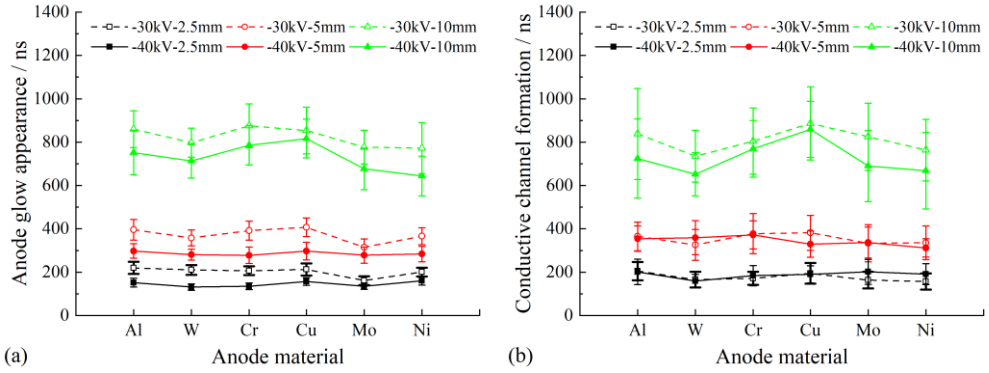

Figure 4-21 Effect of applied pulse voltage on the instants of the anode glow appearance (a) and the conductive channel formation(b)

Finally, the data obtained under all experimental conditions in this chapter (6 materials, 2 voltages, 3 gap lengths, 30 repetitions of each experiment, 1080 experiments in total) were used to analyze the correlation between the instant of the anode glow appearance and the instant of the conductive channel formation. The data of the 1080 experiments were plotted in the form of scattered points in Figure 4-22, using the instant of the conductive channel formation as the x coordinate and the instant of the anode glow appearance as the y coordinate. The data for different gap lengths are indicated by different symbols, and it can be seen that both the anode glow and the conductive channel require a longer delay to form in longer gaps. Next, the Pearson correlation coefficient was calculated for the x-coordinate (conductive channel formation) and the y-coordinate (anode glow appearance) of the data points in Figure 4-22, as follows:

$$\rho_{X,Y}=\frac{\mathrm{cov}(X,Y)}{\sigma_X\sigma_Y} \tag{4-12}$$

where X is the set consisting of x-coordinates of data points; Y is the set consisting of y-coordinates of data points; $\rho_{X,Y}$ is the Pearson correlation coefficient; $\mathrm{cov}(X,Y)$ is the covariance of X and Y; σ_X is the standard deviation of X; σ_Y is the standard deviation of Y. The covariance and standard deviation are calculated as follows:

$$\mathrm{cov}(X,Y)=\frac{\sum_{i=1}^{n}(X_i-E(X))(Y_i-E(Y))}{n} \tag{4-13}$$

$$\sigma_X=\sqrt{\frac{\sum_{i=1}^{n}(X_i-E(X))^2}{n}} \tag{4-14}$$

$$\sigma_Y=\sqrt{\frac{\sum_{i=1}^{n}(Y_i-E(Y))^2}{n}} \tag{4-15}$$

where X_i is the i-th element of the data set X; $E(X)$ is the mean of the data set X; Y_i is the i-th element of the data set Y; $E(Y)$ is the mean of the data set Y; n is the element number sets X and Y. The covariance represents the overall error of two variables, which is different from the variance that represents the error of only one variable. The variance is a special case of covariance, i.e., when the two variables are identical. The covariance between two variables is positive if they have the same trend, that is, if one of them is greater than its own expectation (the mean) and the other is also greater than its own expectation. If the two variables have opposite trends, i.e., if one is greater than its own expectation and the other is less than its own expectation, then the covariance between the two variables is negative. The Pearson correlation coefficient $\rho_{X,Y}$ is a quantity that examines the degree of linear correlation between variables, and it has a value between -1 and 1. The larger the absolute value of the Pearson coefficient, the greater the degree of correlation between the two data sets X and Y. When the absolute value of Pearson coefficient is equal to 1, there is a linear correlation between the data sets X and Y, i.e., the relationship between the two can be described by $Y=aX+b$. When the Pearson coefficient is equal to -1, a is negative and X and Y are negatively correlated; when the Pearson coefficient is equal to 1, a is positive and X

and Y are positively correlated. However, note that the Pearson coefficient $\rho_{X,Y}$ is not equal to the slope a.

After calculation, the Pearson correlation coefficient for the data in Figure 4-22, $\rho_{X,Y}$=0.937, implies a strong linear correlation between the instant of the conductive channel formation and the instant of the anode glow appearance. Then, a fitting straight line obtained by linear fitting of the data in Figure 4-22 is plotted in black with the slope and intercept of a=0.945 and b=18.83, respectively. This indicates that the appearance of the anode glow and the formation of the conductive channel are very close in time. These results reflected quantitatively that the appearance of the anode glow and the formation of the conductive channel are both the result of the expansion of the cathode plasma to the anode.

However, according to the distribution characteristics of the data points in the figure, it can be found that the sequential order of the two events is somewhat random, which means that there is no interdependent or causal relationship between the appearance of the anode glow and the establishment of the conductive channel. At the same time, it also means that the conductive channel can be formed without the anode glow at all. In another experiment published by the authors using a larger vacuum gap (30 mm)[99], it was found that the formation of the conductive channel could be 1 μs ahead of the appearance of the anode glow and that the anode glow was essentially negligible in time and space at that stage. These all demonstrate a fact that the anode glow is not a necessary condition for the formation of the conductive channel.

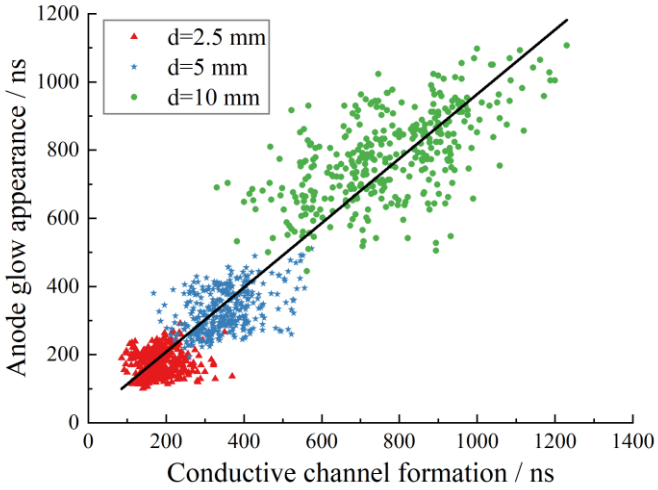

Figure 4-22 Correlation analysis between the instant of the anode glow appearance and the instant of the conductive channel formation based on all the experimental results in this chapter (Pearson correlation coefficient $\rho_{X,Y}$=0.937, slope and intercept of the linear fit are a=0.945 and b=18.83, respectively)

4.6 DISCUSSION

In this chapter, the mechanism by which the atoms on the anode surface leave the anode and participate in the anode glow is analyzed by comparing the instants of the anode glow appearance under different experimental conditions. According to the

analysis of the heat transfer process inside the anode, the evaporation mechanism does not explain the experimental results well for the following reasons:

(1) There are differences of several orders of magnitude in the density of evaporated atoms between different anode materials, while the instants of the emergence of the anode glow are very close (see Figure 4-10 and Figure 4-19).

(2) For some anode materials, the density of evaporated atoms is not sufficient for glowing, while the occurrence of the anode glow is experimentally observed near the anode surface for all materials (see Figure 4-19).

(3) The estimated evaporated atom number density n^{ev} is extremely sensitive to the variation of the chosen value of the electron beam distribution radius σ. Based on the ablation of the anode surface after breakdown experiments, the distribution radius of the electron beam in a 5 mm vacuum gap is likely to be above 2 mm. With such a distribution radius, the evaporated atom number density corresponding to all anode materials does not reach the level that would produce anode glow (see Figure 4-19(d)).

On the other hand, the analysis of the sputtering process on the anode surface reveals that (refer to

Table 4-3):

(1) The sputtered atom number densities corresponding to different anode materials are all around the same order of magnitude, and such atom densities reach the level that could produce the anode glow.

(2) The change of the ion beam distribution radius has a small effect on the sputtered atom number density. At a distribution radius of 2 mm (for a gap length of 5 mm), the sputtered atom number density is still much higher than the atom density corresponding to the vacuum conditions used in the experiments and meets the conditions for producing the anode glow.

Therefore, under the experimental conditions of this chapter, the main mechanism by which the atoms on the anode surface leave the surface is the sputtering mechanism.

By analyzing the correlation between the instant of the anode glow appearance and the instant of the conductive channel formation, it is found that there is a strong linear correlation between the two events, and the instants of their occurrence are close to each other. This further indicates that both the appearance of the anode glow and the formation of the conductive channel depend on the same process, i.e., the expansion of the cathode plasma. However, the randomness of the sequential order of the two events also suggests the non-necessity of the anode glow for the formation of the conductive channel.

The spectral analysis in Chapter 3 shows that the cathode plasma can expand to reach the anode, and the results in this chapter in turn show that the conductive channel can be formed with no light emission from the anode at all. These two results imply that

the conductive channel can be established with only the expansion of the cathode plasma. That is, the generation and expansion of the cathode plasma is a sufficient condition for the formation of the conductive channel. On the other hand, the establishment of the conductive channel needs to be predicated on the smooth start of vacuum breakdown and the filling of the gap by the plasma. As discussed in Chapter 2, the necessary condition for the start of vacuum breakdown is the generation of the cathode plasma. The rise of the current and the filling of the gap by the plasma during breakdown depend on the further expansion of the cathode plasma. These two facts show that the generation and expansion of the cathode plasma is a necessary condition for the formation of the conductive channel. Therefore, the necessary and sufficient condition for the formation of the conductive channel during vacuum breakdown is the generation and expansion of the cathode plasma.

It should be noted that the above analysis regarding the anode glow is based on the experimental conditions of this dissertation. The high dependence of the atom number density resulting from the evaporation by electron heating on the electron beam distribution radius σ in

Table 4-3 indicates that the intensity of the evaporation process on the anode surface increases significantly with the increase of the energy density carried by the electron beam. If the gap current is sufficiently high or the electron beam distribution radius is sufficiently small (e.g. in short gaps), the evaporation of the anode surface due to electron beam heating is likely to overtake the sputtering of the anode surface due to ion beam bombardment as the dominant mechanism for generating anode glow. In such a case, the local high temperature on the anode surface may also produce an anode plasma. The expansion process of the anode plasma to the cathode will definitely accelerate the process of conductive channel establishment[1, 100, 101]. When the anode plasma and the cathode plasma meet, the vacuum gap is filled with plasma and a conductive channel is formed. Inada *et al*[76] used two 1 mm diameter rod electrodes to form a vacuum gap of 3 mm, and such a gap structure resulted in a more concentrated distribution of the electron beam on the anode surface. In addition, the gap current during their experiments reached 700 A. These two conditions led to a significant increase in the energy flow density of the electron beam input to the anode, which resulted in the intense evaporation from the anode surface and the formation of an anode plasma. According to their observations, the anode glow appears 50 ns after the onset of breakdown, and it is impossible for the expanding cathode plasma to reach the anode in such a short time (an expansion rate of 20000 m/s only covers 1 mm in 50 ns, while the gap length is 3 mm). Therefore, the anode glow in this case can only be the result of evaporation from the anode surface because of electron beam heating. This means that the contribution of the evaporation mechanism on the anode surface to the anode glow exceeds that of the sputtering mechanism. Chalmers *et al*[81] observed the anode glow in a 0.5 mm tip-plane gap to appear 10-20 ns after the onset of breakdown, but no specific gap current values were given. Based on the anode glow

delay, it can be inferred that the anode glow in their experiments is also the result of the evaporation of the anode under the effect of electron beam heating. In both experiments, the appearance of the anode glow is due to the formation of an anode plasma at high local temperatures on the anode surface. The expansion of the anode plasma (anode glow) eventually contributed to the formation of the conductive channel in the vacuum gap, which is the reason why some researchers consider the expansion of the anode glow and the establishment of the light-radiation channel as a necessary condition for the formation of the conductive channel.

In summary, the necessary and sufficient condition for the formation of conductive channels during vacuum breakdown is the generation and expansion of the cathode plasma, while the anode glow is a secondary phenomenon caused by the expansion of the cathode plasma. The mechanism for the generation of the anode glow may vary with the electrode structure, gap length, current magnitude, electrode material and other factors, making it possible for the anode glow to play a role in promoting the establishment of the conductive channel under some specific experimental conditions. However, it must be clearly recognized that the appearance and expansion of the anode glow are not necessary for the construction of the conductive channel as we clearly see in our experiments.

5 THEORETICAL ANALYSIS OF CONDUCTIVE CHANNEL FORMATION PROCESS IN VACUUM BREAKDOWN

5.1 OVERVIEW

Through the experimental studies in the previous chapters, a clear understanding of the important physical processes such as the cathode glow, the anode glow, and the cathode plasma expansion involved in the conductive channel formation stage of vacuum breakdown and their effects on the conductive channel formation have been achieved. The necessary and sufficient condition for the establishment of the conductive channel during vacuum breakdown has been proposed, i.e., the generation and expansion of the cathode plasma.

In this chapter, a simulation model of the vacuum breakdown process based on Particle In Cell-Monte Carlo Collision (PIC-MCC) is established to analyze the evolution of particle distribution, electric field distribution and voltage-current waveforms during the formation of the conductive channel. The simulation results visualize the construction of the conductive channel in the vacuum gap and verify the sufficiency and necessity of the generation and expansion of the cathode plasma for the conductive channel formation. Finally, based on the results of experimental and simulation studies, the physical processes related to the conductive channel formation stage of vacuum breakdown is summarized.

5.2 MODELING OF CONDUCTIVE CHANNEL FORMATION PROCESS IN VACUUM BREAKDOWN

5.2.1 INTRODUCTION TO PIC-MCC METHOD WITH EXTERNAL CIRCUIT

In this chapter, the development process of vacuum breakdown is simulated using the VSim software[102] based on the PIC-MCC method[103].The PIC method is widely used for simulating the interaction between charged particles and electromagnetic fields. In this method, the spatial electromagnetic field is discretized onto a mesh and the actual particles are represented by macro-particles with certain weights. The MCC method is used to simulate the interaction among particles during their motion. The method guarantees the reaction among particles with a certain collision probability by random sampling. VSim software also supports self-consistent simulation of plasma by coupling the solution of the electromagnetic field with that of the external circuit through a custom field approach. For the vacuum breakdown problem, the spatial electromagnetic field is solved using an electrostatic model, i.e., only Poisson's equation is solved to analyze the spatial electric field.

Figure 5-1 gives the flowchart for the PIC-MCC method with an external circuit, which is illustrated as follows:

(1) Simulation system initialization, including the initialization of various relevant physical fields and particles;

(2) Moving time one step forward and inject corresponding number of particles (atom evaporation and electron emission) into the calculation domain;

(3) Accumulation of the charge carried by the particles in the calculation domain onto the surrounding grid nodes to obtain the distribution of the charge density;

(4) Based on the charge exchange between the calculation domain and the external circuit, the external circuit is updated one step forward to obtain the latest boundary conditions for the calculation domain. For breakdown and discharge problems, the voltage across the gap is generally updated by the external circuit and used as the boundary condition;

(5) Solving Poisson's equation according to the charge density distribution and boundary conditions of the calculation domain to obtain the potential distribution and electric field distribution in the gap;

(6) Calculating the force on charged particles from the electric field and updating the velocity and position of the particles according to Newton's law;

(7) Determining whether a collision process has occurred according to the MCC method. If there is, the particle type and velocity information is updated according to the corresponding reaction; if not, the next step is performed;

(8) Checking whether the preset number of calculation steps has been reached. If it has been reached, end the calculation; if not, repeat steps (2)-(7).

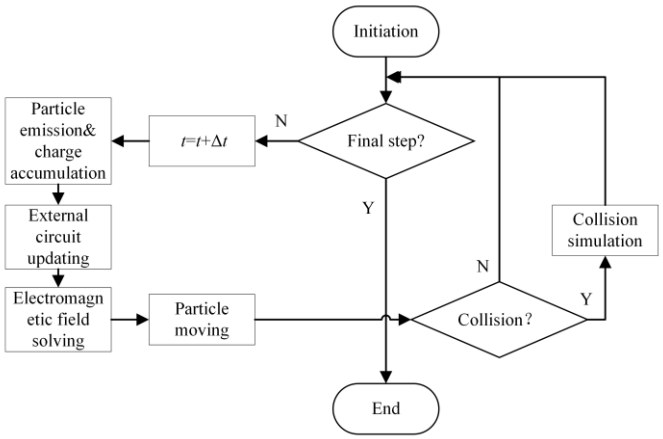

Figure 5-1 Calculation flow chart of PIC-MCC method in VSim software

5.2.2 PHYSICAL MODEL AND SIMULATION SETUP OF CONDUCTIVE CHANNEL FORMATION PROCESS IN VACUUM BREAKDOWN

The PIC-MCC method is an extremely demanding method in terms of computational resources, and the simulation of breakdown processes in millimeter-scale vacuum

gaps with this method is still a worldwide challenge. Therefore, the simulations in this chapter set the computational region within the range allowed by the computational efficiency and aim to describe the generation and expansion of the cathode plasma, and the establishment of the conductive channel during vacuum breakdown from a qualitative point of view. Figure 5-2 shows the physical model of the conductive channel formation process in vacuum breakdown. This chapter calculates the breakdown process in a vacuum gap formed by two paralleled circular electrodes (copper material) with a radius of 1000 nm and a gap length of 250 nm. Because of the axisymmetric nature of the electrode structure and the subsequent physical process of vacuum breakdown, a two-dimensional axisymmetric model is used for the simulation. As shown in the figure, the horizontal direction z represents the symmetry axis, and the vertical direction indicates the radial direction r. The left electrode is the cathode and the right electrode is the anode. The two electrodes are connected through an external circuit containing a voltage source U_{ext} and a resistor R_{ext}.

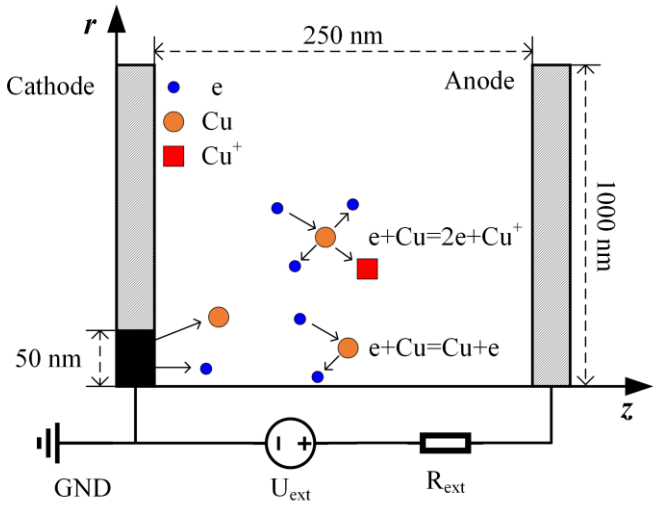

Figure 5-2 Physical model of the conductive channel formation process in vacuum breakdown

According to the results of the previous chapters, the generation and maintenance of the cathode plasma is the key to drive the development of vacuum breakdown. Therefore, the simulation of the conductive channel formation process must be based on the premise that cathode plasma can be generated in the calculation domain. In vacuum breakdown, cathode plasma is generated by cathode spots[104], and the formation of cathode spots is the result of a thermal instability process occurring in localized regions (microprotrusions) on the cathode surface. According to the vacuum arc theory, the size of a single cathode spot is of the order of microns and the lifetime is of the order of nanoseconds; a large number of cathode spots are continuously generating and extinguishing during vacuum breakdown, and their averaging over time and space makes it possible for plasma to be generated on the cathode surface all the time. The specific process of cathode spots involves complex interactions between the cathode surface material and the cathode plasma, while the goal of this chapter is to simulate the expansion of the cathode plasma after its formation and the establishment of the conductive channel, so the specific mechanism of metal vapor generation from cathode spots is ignored. During the simulation, an equivalent cathode

surface temperature is set and atoms are emitted into the vacuum gap according to the corresponding evaporation rates (see Equation (4-7) and (4-8)) to simulate the atomic supply from the cathode spot. The electron emission from the cathode spot is also simplified to consider only the field-induced emission, which is described by using the Fowler-Nordheim formula[33, 34] as follows:

$$J_{\mathrm{FN}}=1.54\times10^{-6}\frac{E_{\mathrm{Loc}}^{2}}{\phi_{\mathrm{w}}}\exp\left(-6.83\times10^{9}\frac{\phi_{\mathrm{w}}^{1.5}}{E_{\mathrm{loc}}}\right) \tag{5-1}$$

$$E_{\mathrm{Loc}}=\beta_{\mathrm{FN}}E_{\mathrm{mac}} \tag{5-2}$$

where J_{FN} is the field electron emission current density (in $\mathrm{A\cdot m^{-2}}$); E_{Loc} is the local electric field (in $\mathrm{V\cdot m^{-1}}$) at the electron emission point; ϕ_{w} is the work function of the material (4.5 eV for copper); β_{FN} is the enhancement factor of the electric field at the emission point, which indicates the gain of electric field due to surface microstructure, usually ranges from tens to hundreds, and is set to 75 in this chapter; E_{mac} is the macroscopic electric field at the emission point (in $\mathrm{V\cdot m^{-1}}$), for planar parallel electrodes

$$E_{\mathrm{mac}}=u_{\mathrm{gs}}/d_{\mathrm{g}} \tag{5-3}$$

where u_{gs} is the gap voltage (in V); d_{g} is the gap length (in m). In this chapter, the initial value of the macroscopic electric fieldin the gap is uniformly set to 200 MV/m, and the initial value of the gap voltage can be calculated to be 50 V according to Equation (5-3). Therefore, the potential of 0 V and 50 V is used as the initial boundary conditions for the cathode and the anode, respectively. The upper and lower boundaries are then set to zero electric field conditions, i.e., the potential gradient is zero. The emission region of electrons and atoms is set as a circular region with a radius of 50 nm. Only elastic collisions and primary ionization (production of single charged copper ions) are considered for the interactions between electrons and copper atoms in the gap, as shown in Figure 5-2. The particles traveling through the calculation domain are absorbed when they reach the boundaries.

The voltage source of the external circuit, U_{ext}, has the same value as the initial voltage of the gap, being 50 V. That is, the gap capacitor is already charged to its maximum voltage before the start of the simulation, and no current flows in the external circuit. After the start of the simulation, the electron emission from the cathode and the absorption of charged particles by both electrodes will change the charge stored on the gap and the voltage across the gap. This will in turn cause a conduction current in the external circuit. The specific algorithms for external circuit updates are as follows:

(1) Initializing the charge stored in the gap capacitance. The charge of the gap can be calculated from the capacitance and voltage of the gap as follows:

$$C_0=\frac{\varepsilon_0 S}{d_{\mathrm{g}}}=\frac{8.854\times10^{-12}\times\pi r^{2}}{d_{\mathrm{g}}}=1.11\times10^{-16}\ \mathrm{F} \tag{5-4}$$

$$Q_{\text{tot}}^{0}=C_0 u_{\text{gs}}^{0}=5.56\times10^{-15}\ \text{C} \tag{5-5}$$

where C_0 is the capacitance of the gap; S is the area of the electrode (in m^2); Q_{tot}^{0} is the initial charge stored in the gap;

(2) For the calculation of step n, evaluate the external circuit current of step n-1 first:

$$I_{\text{ext}}^{n\text{-}1}=\frac{U_{\text{ext}}-u_{\text{gs}}^{n\text{-}1}}{R_{\text{ext}}}=\frac{U_{\text{ext}}-\frac{Q_{\text{tot}}^{n\text{-}1}}{C_0}}{R_{\text{ext}}} \tag{5-6}$$

where I_{ext} is the current flowing through the external circuit (in A);

(3) Calculating the total current corresponding to the electron emission and particle absorption at the cathode surface at step n-1:

$$I_{\text{cathode}}=I_{\text{Cu1\_ab\_c}}+I_{\text{e\_ab\_c}}-I_{\text{e\_em\_c}} \tag{5-7}$$

where I_{cathode} is the total current from the gap to the cathode (in A), a positive value indicates a decrease in the number of negative charges stored at the cathode, a negative value indicates an increase in the number of negative charges stored at the cathode; $I_{\text{Cu1\_ab\_c}}$ is the copper ion current absorbed by the cathode (in A); $I_{\text{e\_ab\_c}}$ is the electron current absorbed by the cathode (in A); $I_{\text{e\_em\_c}}$ is the electron current emitted by the cathode (in A). The electron current is negative and the ion current is positive.

(4) Calculating the total current corresponding to the absorption of electrons and ions at the anode surface at step n-1:

$$I_{\text{anode}}=-I_{\text{Cu1\_ab\_a}}-I_{\text{e\_ab\_a}} \tag{5-8}$$

where I_{anode} is the total current from the anode to the gap (in A), positive value indicates a decrease in the number of positive charges stored by the anode, a negative value indicates an increase in the number of positive charges stored by the anode; $I_{\text{Cu1\_ab\_a}}$ is the copper ion current absorbed by the anode (in A); $I_{\text{e\_ab\_a}}$ is the electron current absorbed by the anode (in A). The electron current is negative, while the ion current is positive.

(5) Calculating the total charge stored in the gap at step n and the corresponding gap voltage:

$$Q_{\text{tot}}^{n}=Q_{\text{tot}}^{n\text{-}1}+I_{\text{ext}}^{n\text{-}1}\Delta t-\frac{I_{\text{cathode}}+I_{\text{anode}}}{2}\Delta t \tag{5-9}$$

$$u_{\text{gs}}^{n}=\frac{Q_{\text{tot}}^{n}}{C_0} \tag{5-10}$$

where Q_{tot}^{n} is the total charge of the gap at step n (in C). According to Equation (5-9), when the vacuum gap is fully conductive (entering steady vacuum arc phase), the cathode current, the anode current and the external circuit current are all equal, and at this time the charge stored on the gap no longer changes.

(6) Solving Poisson's equation with knowing the gap voltage u_{gs}^{n} and the charge density distribution in the calculation domain:

$$\nabla^2\varphi=-\frac{\rho}{\varepsilon_0},\ u_c=0,\ u_a=u_{gs}^{n} \tag{5-11}$$

where φ is electric potential (in V); ρ is charge density (in $C\cdot m^{-3}$); u_c is the potential boundary at the cathode (in V); u_a is the potential boundary at the anode (in V).

(7) Determining the electric field strength from the spatial distribution of electric potential:

$$E=-\nabla\varphi \tag{5-12}$$

Repeating steps (2)-(7) above, the electric field distribution is obtained for each time step, and the force on the charged particles in the gap is obtained and used for the subsequent particle moving.

When simulating plasma using the PIC-MCC method, the determination of the spatial grid size and time step requires consideration of the characteristic scales of the plasma in space and time. The characteristic spatial scale of the plasma is represented by the Debye length λ_D. The Debye length, also called the Debye radius, is used to describe the action scale of the charges in the plasma. The Debye length was first proposed by the Dutch physicist Peter Debye and reflects an important property in plasma, the charge shielding effect. When the scale under discussion is larger than the Debye length, the plasma can be considered as overall electrically neutral and, conversely, as charged. In the PIC-MCC model, the grid size Δx needs to be smaller than the Debye length λ_D, i.e.

$$\Delta x<\lambda_D \tag{5-13}$$

$$\lambda_D=\sqrt{\frac{\varepsilon_0 k_B T_e}{n_e e^2}} \tag{5-14}$$

where k_B is the Boltzmann constant, 1.38×10^{-23} J/K; T_e is the electron temperature (in K); n_e is the electron density (in m^{-3}). When the estimated electron temperature (k_BT_e) is 5 eV and the electron density is 10^{26} $m^{-3,}$ the Debay length can be calculated to be 1.66 nm. Setting the grid size equal to the Debye length (Δx=1.66 nm), the number of grids in the simulation domain along the r and z directions are:

$$NR=\frac{1000\text{ nm}}{1.66\text{ nm}}=600 \tag{5-15}$$

$$NZ=\frac{250\text{ nm}}{1.66\text{ nm}}=150 \tag{5-16}$$

The characteristic time scale of a plasma is expressed by the plasma frequency ω_p. When some kind of perturbation (e.g. thermodynamic rise and fall) occurs within the plasma, it triggers the separation of positive and negative charges, causing the plasma particles to oscillate collectively, and the corresponding oscillation frequency is called

the plasma frequency, which can be calculated by the following equation:

$$\omega_p = \sqrt{\frac{n_e e^2}{\varepsilon_0 m_e}} \tag{5-17}$$

where ω_p is the plasma frequency (in rad/s); m_e is the electron mass, 9.1×10^{-31} kg. When the plasma density is 10^{26} m^{-3}, the time step needs to satisfy the following equation:

$$\Delta t < \frac{2\pi}{\omega_p} = 1.12\times10^{-14} \text{ s} \tag{5-18}$$

In addition, the VSim software requires that the particle cannot move more than one grid in each time step. The maximum energy that an electron can obtain under the effect of electric field acceleration is eu_{gs}^0=50 eV, and this energy corresponds to an electron velocity of 4.2×10^6 m/s. Therefore, the time step should also satisfy the following relation:

$$\Delta t < \frac{\Delta x}{4.19\times10^6 \text{ m/s}} = 3.96\times10^{-16} \text{ s} \tag{5-19}$$

According to Equations (5-18) and (5-19), the time step for the vacuum breakdown simulation was chosen to be $\Delta t=3\times10^{-16}$ s. The simulation started from a complete vacuum, and was performed for a total of 1 million steps, i.e. 300 ps.

5.3 SIMULATION RESULTS OF CONDUCTIVE CHANNEL FORMATION PROCESS IN VACUUM BREAKDOWN

5.3.1 PARTICLE DISTRIBUTION

Figure 5-3, Figure 5-4 and Figure 5-5 show the evolution of the spatial distribution of electrons, atoms and ions, respectively, during a breakdown simulation. To ensure that the cathode surface can produce enough metal vapor to initiate and sustain the vacuum breakdown process, the cathode surface temperature is set to 7000 K, which is within the temperature range of the vacuum arc cathode spot[83, 105]. R_{ext} is set to 20 kΩ. The horizontal axis (r=0) represents the symmetry axis, while the positions z=0 nm and z=250 nm represent the cathode and the anode, respectively.

Under the acceleration of the initial electric field in the gap, the electrons can reach the anode with a maximum kinetic energy of about 50 eV, resulting in a maximum axial velocity of 4.2×10^6 m/s, which allows the electrons to move from the cathode to the anode in less than 120 fs. Therefore, the electrons can fill the entire gap along the axial direction immediately after the simulation starts, as shown in Figure 5-3. The expansion velocities of atoms and ions towards the anode are much smaller in comparison with the electrons. As shown in Figure 5-4, atoms are emitted from the cathode surface with a velocity distribution corresponding to the temperature of the cathode surface and expand toward the anode with such a velocity of about 2000-3000

m/s.

As can be seen from the ion distribution in Figure 5-5, no ions are yet produced at the 15 ps, and the earliest ionization process occurs between 15 and 30 ps, resulting in copper ion generation by 30 ps. In addition, copper ions appear first near the position 50 nm from the cathode surface, which is related to the condition under which the primary ionization process of copper atoms occurs. The first ionization energy of copper atoms is 7.7 eV/atom, and the collision cross section for primary ionization of copper atoms is larger at electron energies of about 10 eV[106-108]. According to the initial electric field distribution of the vacuum gap, the electron energy at 50 nm from the cathode surface reaches exactly around 10 eV, thus allowing the ionization process to occur. Between 30 and 60 ps, more electrons and ions are produced due to collisional ionization between electrons and atoms, as shown in the third images of Figure 5-3 and Figure 5-5. Then, the ions continuously expand toward the anode and occupy more and more space in the gap, with the electrons also expanding in the radial direction. At about 120 ps, the front of the expanding ions reaches the anode surface. After that, the whole gap is bridged by a channel consisting of electrons and ions.

Figure 5-6 shows the variation of the number of electrons and ions with time during the simulation. As the graph shows, the numbers of electrons and ions rise from 50 ps, which is consistent with Figure 5-3 and Figure 5-5. This rapid increase of charged particles implies the initiation of a breakdown process. In the calculation domain used in this chapter, the numbers of both electrons and ions reach more than 20000. In the later stages of breakdown development, the number of ions is slightly more than the number of electrons due to the presence of a cathode sheath layer in the region close to the cathode where the ion density is higher than the electron density, which will be shown in Figure 5-11 and Figure 5-13.

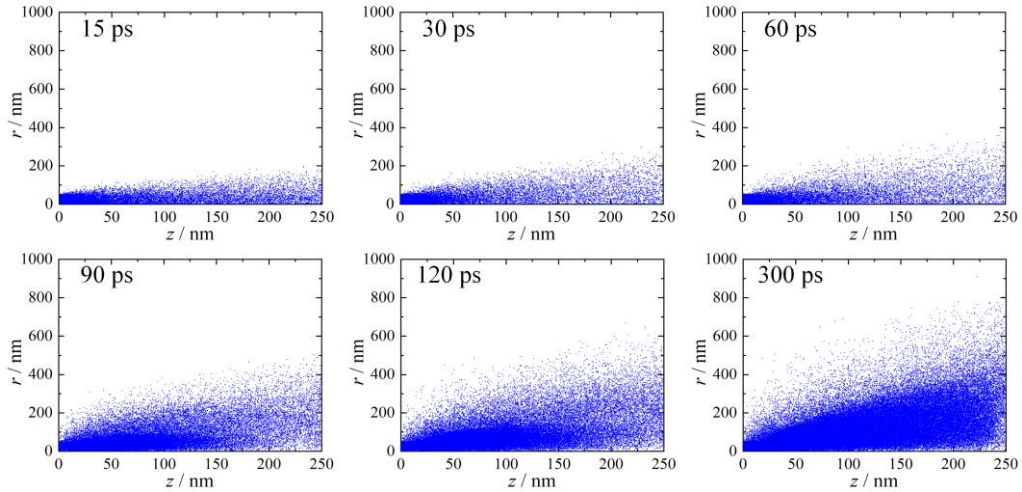

Figure 5-3 Evolution of the spatial distribution of electrons (R_{ext}=20 kΩ, cathode temperature=7000 K)

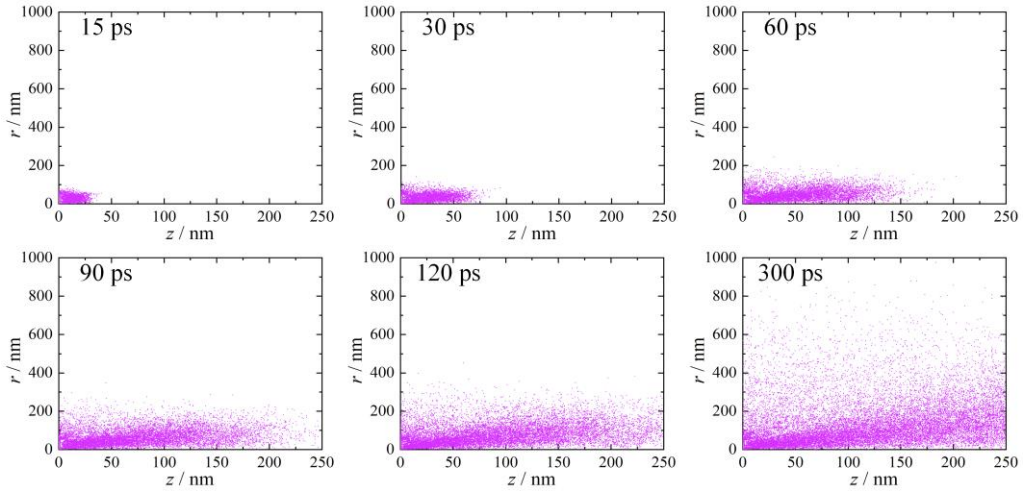

Figure 5-4 Evolution of the spatial distribution of atoms (R_{ext}=20 kΩ, cathode temperature=7000 K)

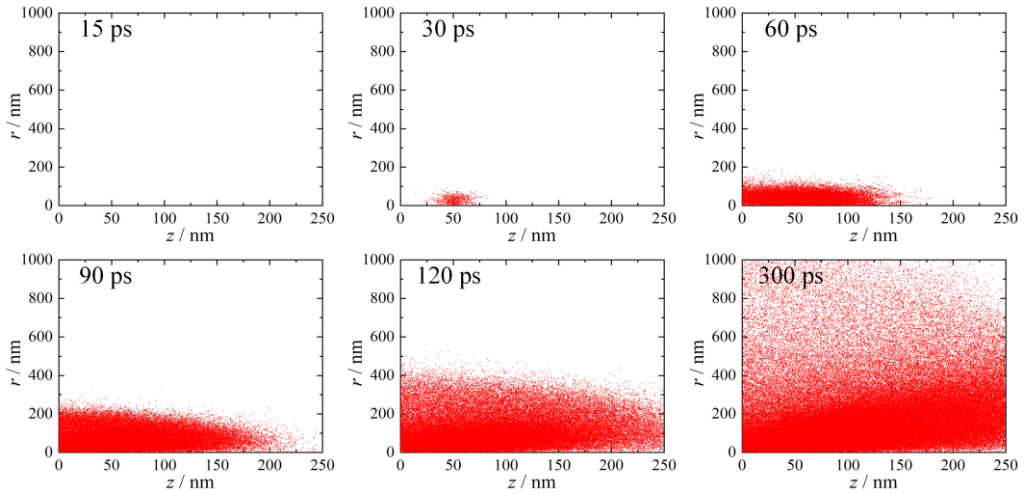

Figure 5-5 Evolution of the spatial distribution of ions (R_{ext}=20 kΩ, cathode temperature=7000 K)

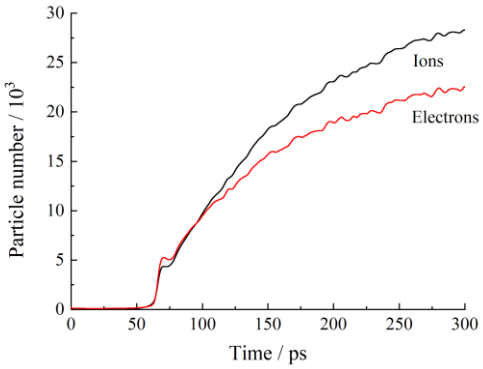

Figure 5-6 Variation of electron and ion numbers with time during vacuum breakdown (R_{ext}=20 kΩ, cathode temperature=7000 K)

In order to check whether the electrons and ions form plasma, the number densities of them were averaged over a 25 nm band along the axis of the simulation domain, and shown in Figure 5-7 for six instants from 60 ps to 135 ps. The positions z=0 nm and z=250 nm represent the cathode and the anode, respectively. From 75 ps on, there is always a region where the electron density equals the ion density, exhibing quasi-neutral characteristics. These quasi-neutral regions are exactly plasma according to its

definition. It can also be seen that the plasma originating from the cathode (i.e. cathode plasma) expands towards the anode, with its front reaching the anode at about 120 ps, which is in line with the expansion pattern of the copper ions as shown in Figure 5-5. Therefore, the expansion front and expansion velocity of the cathode plasma is determined by the ions from the cathode. After 120 ps, most of the gap is occupied by the plasma, indicating the formation of a conductive channel. At 60 ps, there is some difference between the densities of electrons and ions, because ions were just produced for a short time and the quasi-neutral region is still small. However, we can see that the ion density exceeds the electron density, which makes it possible for the electron emission to break the limitation of space charge effect. Combining the fact that both the particle numbers (see Figure 5-6) and gap current (see Figure 5-14) start rising between 50-60 ps, we can recognize the instant of 50 ps as the initiation point of the cathode plasma generation and the vacuum breakdown process.

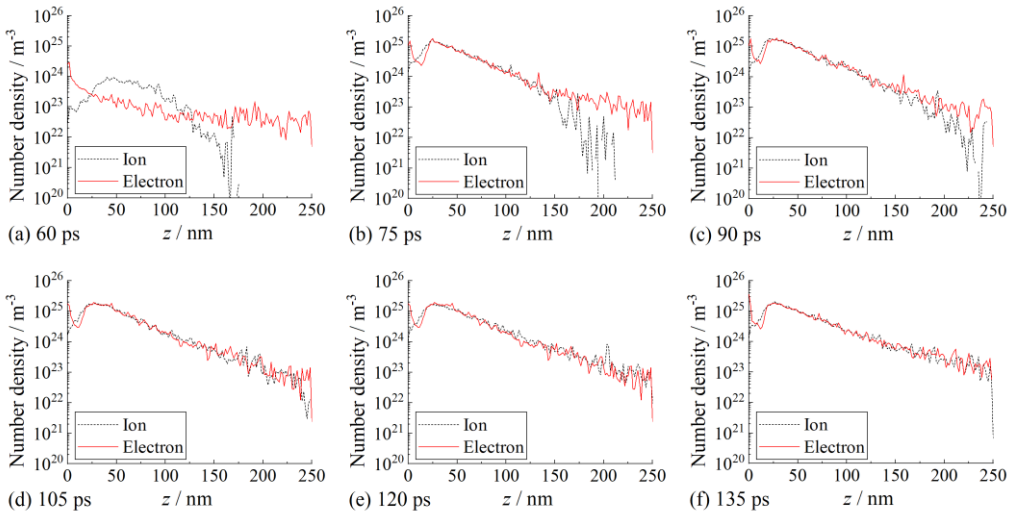

Figure 5-7 Variation of electron and ion densities near the axis (R_{ext}=20 kΩ, cathode temperature=7000 K)

The spatial distribution of the electron density, ion density and atom density at the end of the simulation (300 ps) is given in Figure 5-8, Figure 5-9 and Figure 5-10, respectively. The maximum densities of both electrons and ions appear around 30 nm from the cathode surface, while the density of atoms decreases gradually from the cathode to the anode. Figure 5-11 gives the axial distribution of the three particle densities near the symmetry axis at 300 ps. The maximum density of electrons and ions is 2.2×10^{25} m^{-3}, while the density of atoms is about one order of magnitude higher than that of electrons and ions. This shows that the ionization of atoms is very low (10%), which is not consistent with the high ionization degree of vacuum arcs measured in other literature, probably because the calculation domain is not large enough and the calculation time is not long enough, which needs to be further investigated later. A closer inspection of the electron and ion densities near the cathode (5-15 nm) reveals that the ion density is higher than the electron density here, and thus a positive space charge layer (i.e., the cathode sheath layer) would exist, resulting in an enhanced electric field in this region, as shown in Figure 5-13(b). In the region to the right of 15 nm, the densities of electrons and ions are essentially the same,

indicating that this region is all plasma.

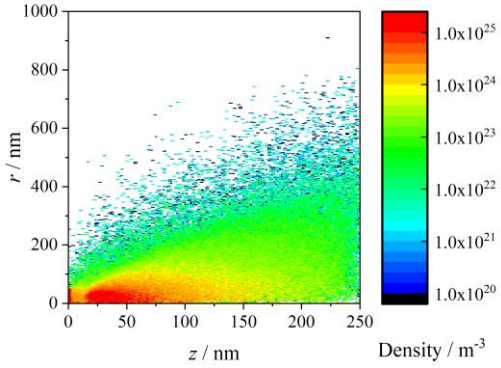

Figure 5-8 Electron density distribution at 300 ps (R_{ext}=20 kΩ, cathode temperature=7000 K)

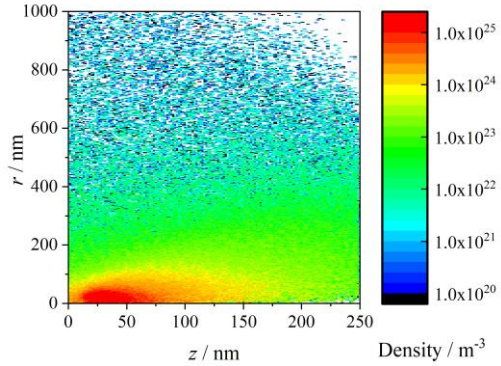

Figure 5-9 Ion density distribution at 300 ps (R_{ext}=20 kΩ, cathode temperature=7000 K)

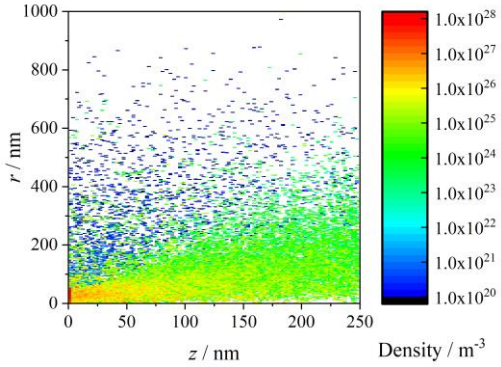

Figure 5-10 Atom density distribution at 300 ps (R_{ext}=20 kΩ, cathode temperature=7000 K)

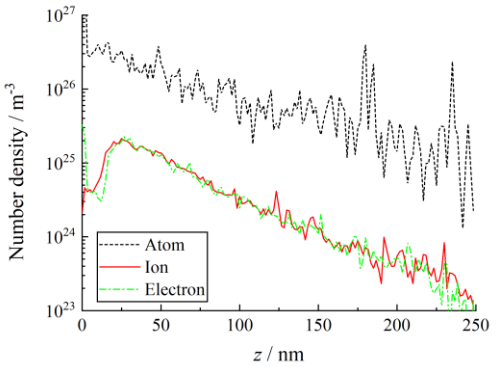

Figure 5-11 Particle density distribution at 300 ps (R_{ext}=20 kΩ, cathode temperature=7000 K)

According to the experimental results, the expansion velocity of the cathode plasma

to the anode can reach 20000 m/s, while the average expansion velocity of the ions shown in Figure 5-5 is only about 2000-3000 m/s. The reasons for these differences are manifold. First, the spatial and temporal scales of the computational region are not large enough to simulate the subsequent expansion process of the plasma. Second, the huge density gradient of ions and atoms in the region near the cathode is the main reason for the acceleration of ions toward the anode, while the elastic collision process between heavy particles is not considered in the simulation of this chapter, and it is impossible to simulate the ion acceleration process under the effect of density gradient. Although there are some differences between simulations and experiments, the simulation results obtained in this chapter can still well describe the formation of conductive channels in vacuum breakdown from a qualitative point of view.

5.3.2 ELECTRIC POTENTIAL AND ELECTRIC FIELD DISTRIBUTION

Figure 5-12 illustrates the variation of electric potential distribution as a function of time, with plots (a)-(f) corresponding to 30 ps, 60 ps, 75 ps, 90 ps, 120 ps, and 300 ps, respectively. Before the start of the simulation, the potential in the vacuum gap is uniformly distributed (the equipotential lines are all equally spaced parallel lines), and the potential rises linearly from 0 V at the cathode (z=0 nm) to 50 V at the anode (z=250 nm). At 30 ps, some ions has already been generated (see Figure 5-5), which result in a weak perturbation of the local potential distribution and a slight bending of the lower end of the 5 V and 10 V contours, as in Figure 5-12(a). The potential on the anode side only drops slightly from 50 V to 48 V due to the very small electron current in the gap, which is consistent with the voltage waveform in Figure 5-14. At 60 ps, as shown in Figure 5-12(b), due to the generation of the initial cathode plasma, the potential distribution near the axis changes more significantly. The electric field is enhanced in the region between 0-50 nm, while it decreases to some extent in the region between 50-150 nm. The voltage across the gap also decreases slightly. At 75 ps, as illustrated in Figure 5-12(c), the potential distribution changes dramatically. The gap voltage drops abruptly from 45 V to about 18 V, and accordingly the electric field in the whole calculated region undergoes a significant decrease. Near the region of 25 nm-100 nm from the cathode, the potential is around 8 V, maintaining the ionization process in this region. At 90 ps, the gap voltage drops further to 12 V and the electric field in space continues to decrease, while the potential at the ionization center near the cathode remains at about 8 V. At 120 ps, when the whole gap is filled by the cathode plasma, the gap voltage drops to the lowest value, 7 V, as in Figure 5-12(e). Since then, the gap voltage remains at 7 V and the ionization center maintains a potential of 8 V.

Figure 5-13 shows the spatial distribution of the electric field intensity near the symmetry axis as a function of time, where the electric field intensity values picked are the components of the electric field along the gap axis. At 30 ps, the electric field remains at 200 MV/m in most areas of the gap, with that near the cathode decreasing to 110-120 MV/m. This low value of the electric field indicates the buildup of the space charge effect due the accumulation of electrons near the cathode surface, which in turn limits the electron emission. At 60 ps, stronger ionization happens near the

position of 50 nm and the initial cathode plasma is formed. This causes a change in the electric field in the gap and especially an increase in the local electric field near the cathode sureface, which makes it possible for the electron emission current to break through the limitation of space charge effect. The rapid rise of the gap current implies the start of the vacuum breakdown. At 75 ps, the electric field in part of the gap (25 nm-125 nm) decreases almost zero, because this region has been occupied by the quasi-neutral cathode plasma (see Figure 5-7(b)). As the breakdown process evolves, the cathode plasma occupies more and more space in the gap, with the corresponding electric field declining to almost zero. At 120 ps, when the expanding cathode plasma reaches the anode (see Figure 5-7(e)), the entire vacuum gap is connected by the plasma channel, and the electric field in most regions of the gap almost disappears. Only a small region in front of the cathode surface keeps a very high electric field for the maintaining of electron emission and subsequent ionization process at the cathode. At this point, the insulated vacuum gap becomes a good conductive channel.

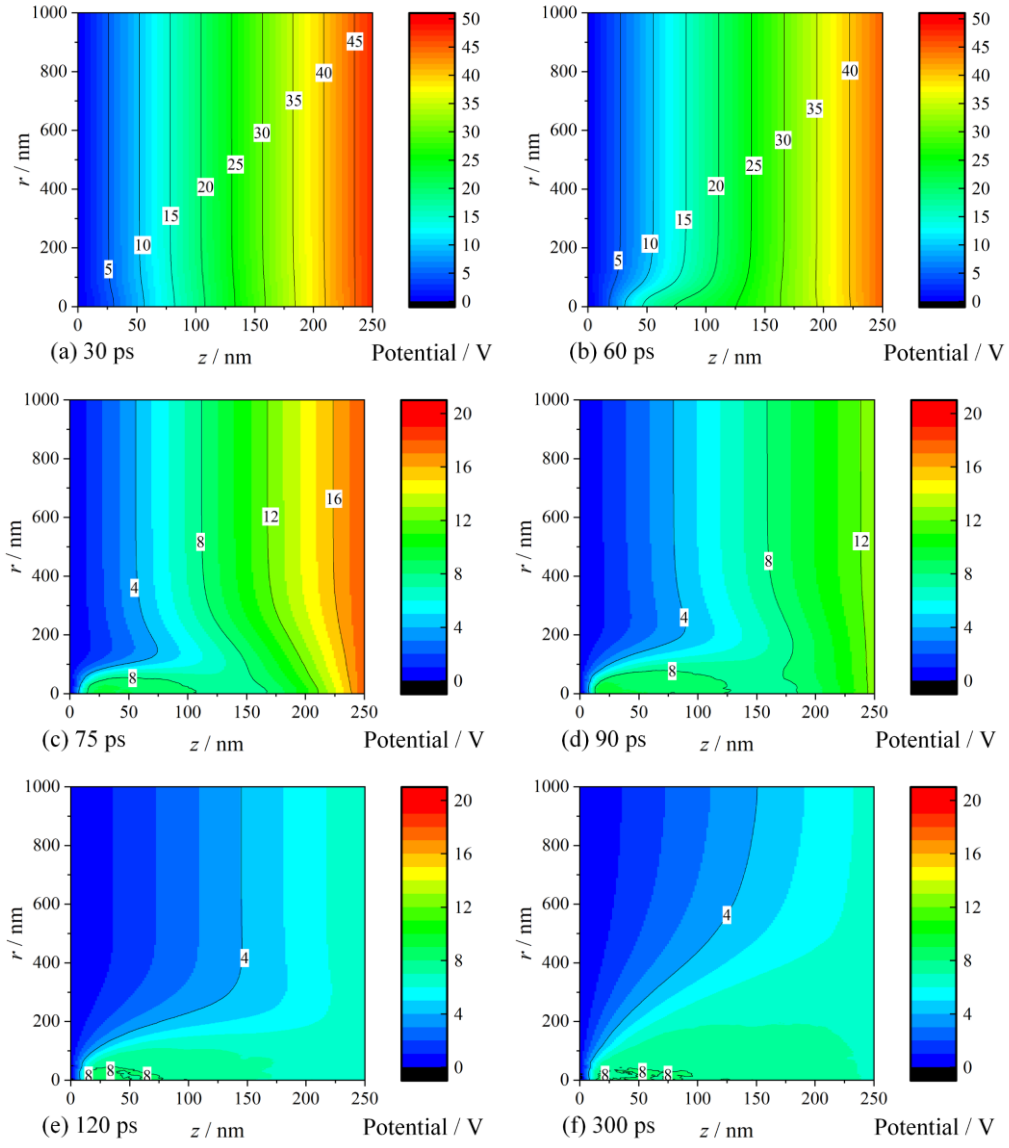

Figure 5-12 Variation of potential distribution with time (R_{ext}=20 kΩ, cathode temperature=7000 K)

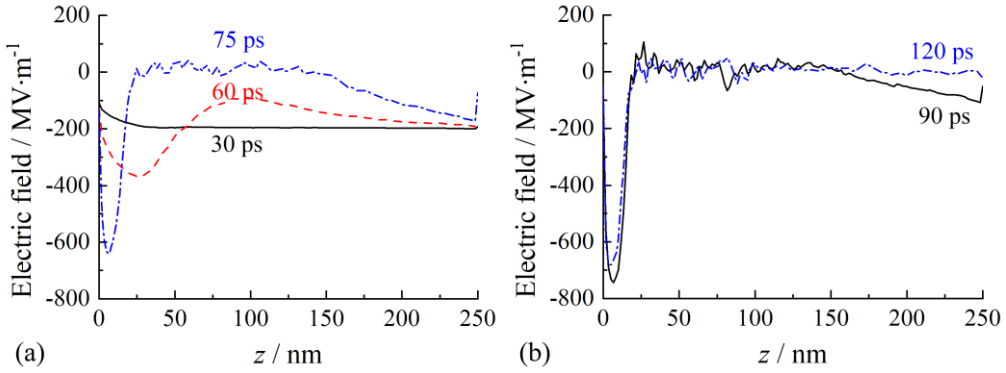

Figure 5-13 Electric field intensity distribution at different instants (R_{ext}=20 kΩ, cathode temperature=7000 K)

5.3.3 VOLTAGE AND CURRENT

Figure 5-14 shows the waveforms of the gap voltage u_{gs} and the external circuit current I_{ext} during the vacuum breakdown process obtained by simulation. As shown in the figure, the gap voltage and the external circuit current at the initial instant are 50 V and 0 A, respectively. After a very short period, the external circuit current rises to about 0.1 mA and maintains at this current level for about 50 ps. During this stage, the voltage on the resistance of the external circuit is approximately 2 V (0.1 mA×20 kΩ), while the gap voltage is approximately 48 V. After 50 ps, the external circuit current starts to rise rapidly and the corresponding gap voltage drops rapidly, indicating the breakdown initiation. Until about 120 ps, the gap voltage and the external circuit current reached steady-state values of 6.4 V and 2.18 mA, respectively, indicating the conductive channel formation. At this point, the voltage on the resistance of the external circuit is 43.6 V (2.18 mA×20 kΩ).

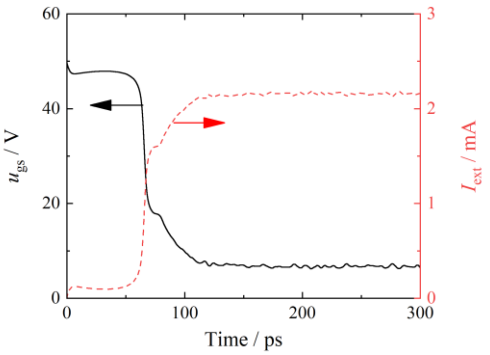

Figure 5-14 Voltage and current waveforms of the vacuum breakdown process obtained by simulation (R_{ext}=20 kΩ, cathode temperature=7000 K)

Figure 5-15 shows the total current flowing from the gap to the cathode ($I_{cathode}$, hereafter referred to as the total cathode current) and its components as a function of time. The components of the total cathode current include the electron emission current $I_{e\_em\_c}$, the electron absorption current $I_{e\_ab\_c}$ and the ion absorption current $I_{Cu1\_ab\_c}$, where the emission of electrons and the absorption of ions are positive contributions to the total cathode current, while the electron absorption current is a

negative contribution to the total cathode current, and the relationship between them is shown in Equation (5-7). As can be seen from Figure 5-15, the trend of each current component with time is consistent with the trend of the external circuit current in Figure 5-14. The total cathode current consists mainly of electron emission from the cathode, which contributes 107% to the total cathode current in the steady-state stage. The electron absorption current and ion absorption current contribute -9.5% and 2.5%, respectively. A closer look at the waveform of the electron emission current $I_{e\_em\_c}$ shows that this current has a very high pulse at the very beginning of the simulation, but it quickly decreases to the level of 0.1 mA. During the next 50 ps, all of the total cathode current comes from the electron emission current, being 0.1 mA, which is consistent with the value of the external circuit current in Figure 5-14 for that time period. Based on the current density of the field electron emission (see Equation (5-1)) and the area of the emission point (a circular region of 50 nm radius), the current of the field electron emission can be easily calculated to be 7.83 mA, which is much larger than 0.1 mA. As mentioned in Chapter 2, the current at the cathode surface is limited by the space charge effect when pure electron emission occurs. According to Equation (2-7), the electron emission current density when space charge effect is considered is 1.32×10^{10} A/m^2, which corresponds to a total current in the emission region of 0.1036 mA. This current is also consistent with the reduced electric field at the cathode surface, 110-120 MV/m, as shown in Figure 5-13(a). Therefore, the pulses in the total cathode current and electron emission current at the beginning of the simulation are the result of the electron emission according to Equation (5-1). However, the electron emission is soon limited by the space charge effect, which keeps the current between 0 and 50 ps at 0.1 mA. After 50 ps, both the electron emission current and the total cathode current start to rise rapidly, in agreement with the rise of the external circuit current in Figure 5-14. This indicates that the gap current starts to break the limit of space charge effect, which is caused by the initiation of the cathode plasma and the increase in the local electric field at the cathode surface, as discussed in the two previous sections. Therefore, the breakdown process of the vacuum gap starts from 50 ps.

The total current flowing from the anode to the gap on the anode side (I_{anode}, hereafter referred to as the total anode current) and its components as a function of time are given in Figure 5-16. The components of the total anode current include the electron absorption current $I_{e\_ab\_a}$ and the ion absorption current $I_{Cu1\_ab\_a}$, where the electron absorption current is a positive contribution to the total anode current, while the ion absorption current is a negative contribution to the total anode current, and the relationship between them is shown in Equation (5-8). The total anode current comes mainly from the absorption of electrons by the anode, and the contribution of the latter to the total anode current in the steady-state phase is 101%. The contribution of the ion absorption current is only -1%, which is inconsistent with the experimentally measured ion current in the vacuum arc (-10%)[97, 98]. This may be because the calculation domain is too small and considers only a single ionization process, where the copper atoms evaporated from the cathode are not yet fully ionized. In addition, the total anode current and the electron absorption current do not appear as high pulses at the beginning of the simulation, and the total anode current stays around 0.1 mA

until 50 ps.

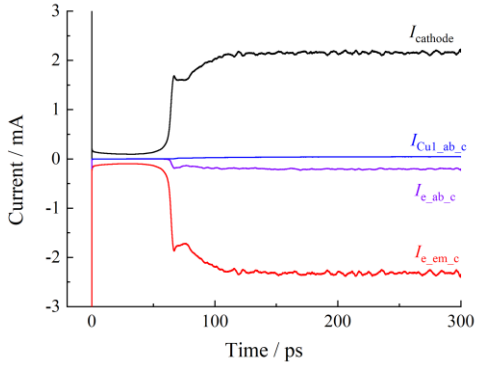

Figure 5-15 Total cathode current and its components (R_{ext}=20 kΩ, cathode temperature=7000 K)

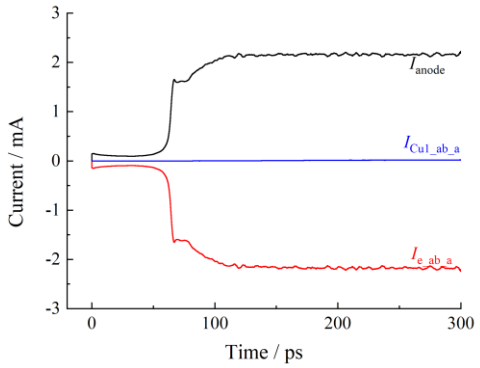

Figure 5-16 Total anode current and its components (R_{ext}=20 kΩ, cathode temperature=7000 K)

Figure 5-17 shows the variation of the total cathode current, the total anode current and the external circuit current with time. After the vacuum breakdown starts at the 50 ps instant, all three currents rise rapidly. The total cathode current and the total anode current are so close that they are almost indistinguishable, while they differ somewhat from the external circuit current between 50 and 120 ps. According to Equation (5-9), the quantitative relationship between the three currents determines the trend of the stored charge on the gap, Q_{tot}, and the gap voltage, u_{gs}. The time variation of Q_{tot} and the current difference between the external circuit and the gap is given in Figure 5-18, where the current difference is $I_{dif}=I_{ext}-0.5(I_{cathode}+I_{anode})$. As in the figure, the absolute value of the current difference starts to rise at 50 ps, and the gap charge starts to decrease gradually, corresponding to a gradual decrease in the gap voltage, as shown in Figure 5-14. The current difference reaches its peak at 66 ns, and the rate of decrease of Q_{tot} reaches the maximum accordingly. Thereafter, the reduction rate of the gap charge gradually slows down. After 120 ps, the external circuit current and the total cathode and anode currents are basically equal to each other, and the gap charge and voltage no longer change significantly, as shown in Figure 5-14, Figure 5-17 and Figure 5-18. This instant coincides well with the instant when the expanding cathode plasma arrives the anode, indicating the beginning of the steady vacuum arc stage and also the conductive channel formation.

To summarize the above three sections, both the initiation of the vacuum breakdown and the formation of the conductive channel are related to the evolutions of particles, electric field and waveforms. The cathode plasma generation, the increase of local

electric field at the cathode surface, and the rapid rise of gap current correspond to the breakdown initiation. The arrival of the expanding cathode plasma at the anode, the collapse of the electric field to almost zero in the gap, and the drop of the gap voltage to the low arc voltage correspond to the conductive channel formation.

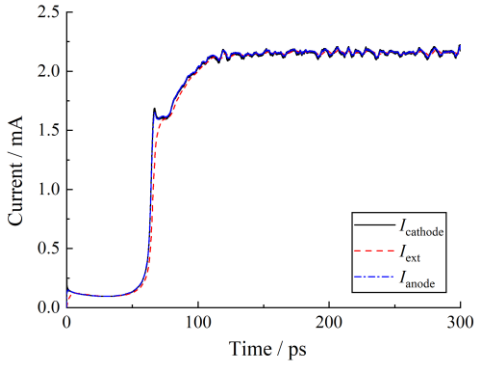

Figure 5-17 Variation of total cathode current, total anode current and external circuit current with time (R_{ext}=20 kΩ, cathode temperature=7000 K)

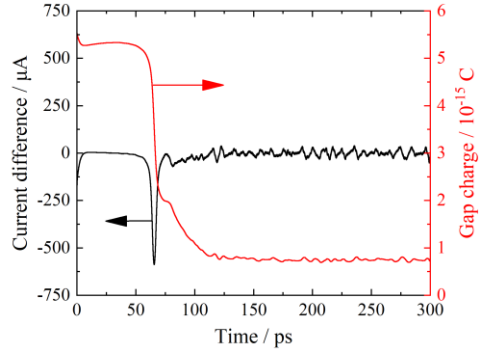

Figure 5-18 Variation of gap charge and current difference, I_{ext}-0.5($I_{cathode}$+I_{anode}), over time

5.3.4 EFFECTS OF EXTERNAL CIRCUIT RESISTANCE

To investigate the effect of external circuit resistance on the vacuum breakdown process, the external circuit resistance is set to 50 kΩ in this section, and the temperature at the cathode surface remains at 7000 K. The waveforms of the gap voltage and external circuit current during vacuum breakdown with different external circuit resistances are compared in Figure 5-19. As shown in Figure 5-19(b), there is no significant difference between the external circuit currents in the phase before the onset of breakdown (t<50 ps), which are 0.1 mA in both cases, i.e., the electron emission current limited by the space charge effect. At the same current (0.1 mA), the voltages across the external circuit resistor are 2 V and 5 V. Therefore, the gap voltages are 48 V and 45 V, respectively, as shown in Figure 5-19(a). The trend of the current waveforms shows that the breakdown occurs at about the same instant in both cases, around 50 ps. Both the current and voltage reach stable values at around 120 ps. The stable values are 6.4 V and 2.18 mA for 20 kΩ, and 7.5 V and 0.85 mA for 50 kΩ. In other words, the increase in the external circuit resistance causes a significant decrease in the external circuit current, while the gap voltage does not change much. The other

current components are reduced accordingly and are not shown here.

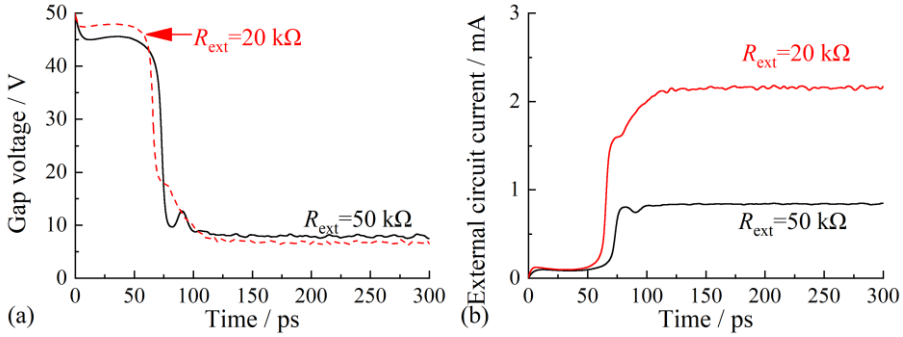

Figure 5-19 Voltage and current waveforms of breakdown process at different external circuit resistance (cathode temperature=7000 K)

Figure 5-20 presents the variation of the number of electrons and ions in the breakdown process with time for an external circuit resistance of 50 kΩ. In comparison with Figure 5-6, it is found that the increase in the external circuit resistance causes a significant decrease in the number of both electrons and ions in the gap, which corresponds to the decrease in the current. At 50 kΩ, the number of ions is still more than the number of electrons, because the ion density at the cathode sheath is still higher than the electron density.

The spatial distribution of electrons, ions and atoms is similar to that given in Figure 5-8 to Figure 5-10 for 20 kΩ. The axial distribution of electron and ion densities near the symmetry axis at the instant of 300 ps for 50 kΩ is given in Figure 5-21. The maximum density of electrons and ions is about 7.5×10^{24} m^{-3}, both of which are reduced compared to the case of 20 kΩ. The cathode sheath layer still exists near the cathode surface, where the ion density is higher than the electron density.

Figure 5-22 shows the potential distribution at 300 ps in the case of 50 kΩ. In comparison with the potential distribution Figure 5-12(f) for 20 kΩ, the potential on the anode side is higher in Figure 5-22 being 7.5 V. However, the potential in the region with the highest plasma density near the cathode is still 8 V, which is consistent with Figure 5-12(f). The above comparison shows that the increase of the external resistance limits the current in the whole system, which in turn affects the ionization process and particle density in the vacuum gap, with some changes in the gap voltage and electric field distribution.

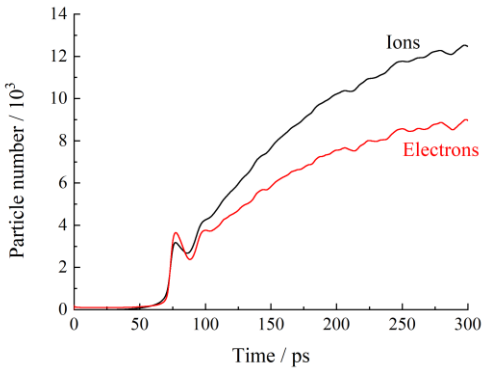

Figure 5-20 Number of electrons and ions during breakdown at an external circuit resistance of 50 kΩ (cathode temperature=7000 K)

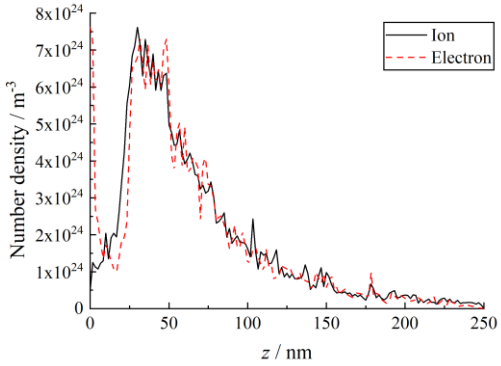

Figure 5-21 Particle density distribution at 300 ps (R_{ext}=50 kΩ, cathode temperature=7000 K)

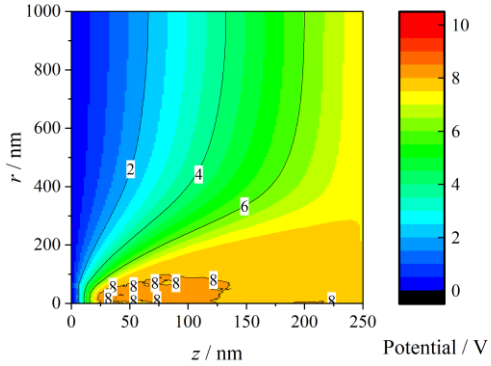

Figure 5-22 Potential distribution at 300 ps when the external circuit resistance is 50 kΩ (cathode temperature=7000 K)

5.3.5 EFFECTS OF CATHODE SURFACE TEMPERATURE

The metal vapor used to form the plasma during vacuum breakdown comes from the metal electrode, and the cathode is the main source of metal vapor in the case of small currents. In the simulations of this chapter, only the evaporation process on the cathode surface is also considered, and the change of the cathode temperature will directly affect the development of the breakdown process. In the following, the cases of cathode surface temperature of 2000 K and 5000 K will be discussed and compared with the case of 7000 K mentioned above. The external circuit resistance is uniformly set to 20 kΩ.

Figure 5-23 compares the gap voltage and external circuit current waveforms for the breakdown process at different cathode surface temperatures. In the phase from 0 to 50 ps, the gap voltage and external circuit current do not differ much, being 48 V and 0.1 mA, respectively. In the phase after 50 ps, the results corresponding to the three temperatures are significantly different. The rate of current rise and voltage drop at a cathode surface temperature of 5000 K is significantly lower than that of the 7000 K. The steady-state current corresponding to a cathode surface temperature of 5000 K is 1.86 mA, which is smaller than that of the 7000 K case (2.18 mA), which also results in a higher gap voltage (12.8 V) for the former case. According to the trend of voltage and current, vacuum breakdown also occurs at the 5000 K case, except that the formation of the discharge channel takes longer time. However, when the cathode

surface temperature is reduced to 2000 K, vacuum breakdown does not occur at all. Throughout the simulation, the current remains at 0.1 mA and the voltage remains at 48 V. This means that the ionization process does not occur and there are only electron currents in the gap that are limited by space charge effects.

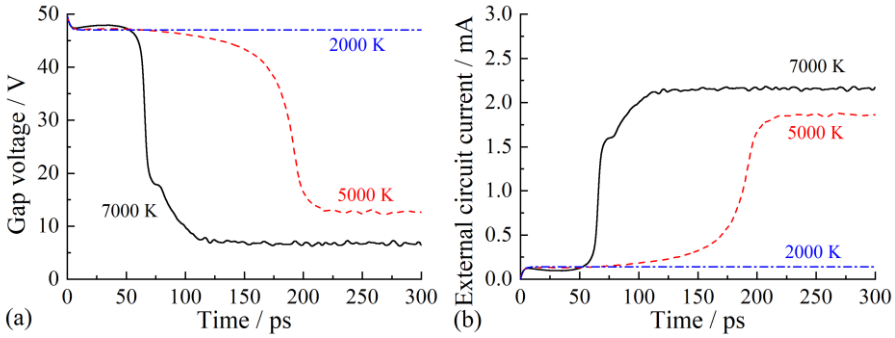

Figure 5-23 Comparison of voltage (a) and current (b) waveforms of breakdown process at different cathode surface temperatures (R_{ext}=20 kΩ)

Figure 5-24 compares the number of electrons, ions and atoms during breakdown for different cathode surface temperatures. As can be seen from the figure, the number of particles decreases significantly with the decrease of the cathode surface temperature. At a surface temperature of 2000 K, there are only 6 atoms in total in the calculation domain, which prevents the ionization process from taking place and the corresponding number of ions is zero. The temperature of the cathode surface directly determines the number and density of metal atoms in the vacuum gap, which in turn influences the ionization and the multiplication process of charged particles. Therefore, the occurrence and maintenance of vacuum breakdown requires the temperature of the cathode surface to be above a certain threshold.

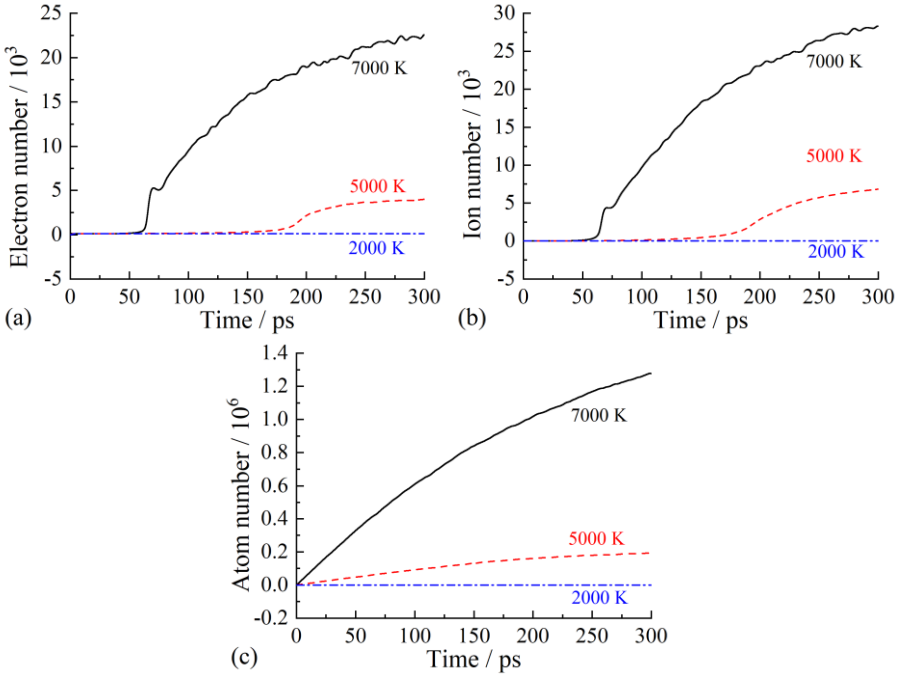

Figure 5-24 Comparison of the number of electrons (a), ions (b) and atoms (c) during breakdown at different cathode surface temperatures (R_{ext}=20 kΩ)

Figure 5-25 shows the potential distribution at 300 ps for a cathode temperature of 5000 K. Comparing this figure with Figure 5-12(f), it can be observed that the potential in the region near the cathode increases from 8 V to 14 V. This is due to the decrease in the collision probability due to the decrease in the metal vapor density, which requires an increase in the ionization collision cross section between electrons and atoms in order to produce a breakdown. The collision cross section for this reaction increases monotonically in the electron energy range of 0-30 eV[106-108], so the potential near the cathode rises to 14 V to ensure sufficient ionization. Figure 5-26 gives the electron and ion density distributions at 300 ps for the 5000 K case. The density reaches a maximum of 4×10^{24} m^{-3} between 50 and 75 nm from the cathode surface, which is lower than in the case of 7000 K (Figure 5-11). A cathode sheath layer still exists near the cathode surface, where the ion density is higher than the electron density.

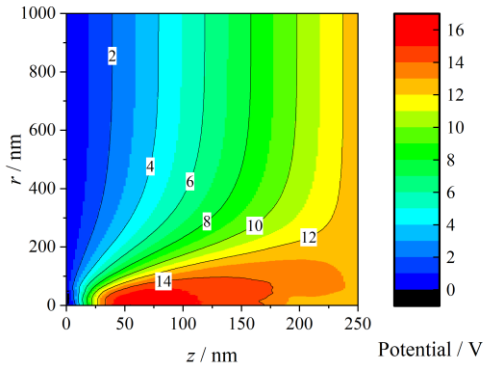

Figure 5-25 Potential distribution at 300 ps (R_{ext}=20 kΩ, cathode temperature=5000 K)

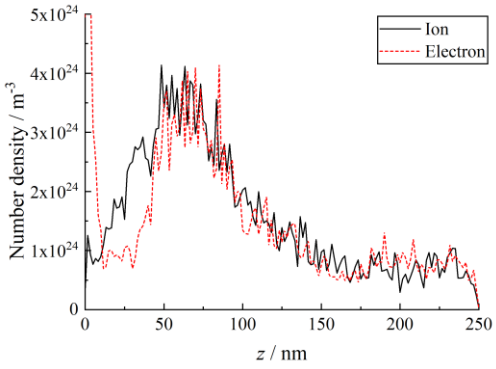

Figure 5-26 Particle density distribution at 300 ps (R_{ext}=20 kΩ, cathode temperature=7000 K)

5.4 DISCUSSION

Summarizing the simulation results of this chapter and the experimental results of the previous chapters, the conductive channel formation stage of vacuum breakdown (P1, the transition from insulation to conduction) can be described as Figure 5-27, where the description involves physical processes such as cathode glow, anode glow, and cathode plasma expansion. As shown in Figure 5-27(a), the occurrence of vacuum breakdown requires electron emission from the cathode surface as a precondition. When a high voltage is applied between the cathode and the anode, electrons are

emitted from the cathode surface in the presence of an electric field, called field electron emission. The field electron emission can be described by Equation (1-1). The electrons emitted from the cathode fly to the anode due to acceleration through the electric field in the gap, forming electron current. However, since the pure electron emission process is limited by the space charge effect (see Equation (2-7)), the current in the external circuit is relatively low. Therefore, at this time the gap voltage remains high and the vacuum gap is essentially in an insulating state. On the other hand, the electron current emitted from the cathode leads to a thermal instability process through Ohmic heating and Nottingham effect which causes a significant increase in the temperature of the local cathode surface[63], prompting the emission of atoms from the cathode material into the vacuum gap. As shown in Figure 5-27(b), the cathode atoms are ionized during the continuous collisions with electrons, resulting in the formation of a dense cathode plasma near the cathode. Interactions between electrons and heavy particles in the cathode plasma are constantly occurring, resulting in bright cathode glow. At this point, the voltage across the gap starts to drop and the voltage is mainly distributed between the anode and the boundary of the cathode plasma facing the anode. This is because the plasma is quasi-electrically neutral and the voltage drop in the region occupied by the cathode plasma is small, and the boundary of the cathode plasma can be considered as a virtual cathode at this time. Under the action of the electric field in the gap, electrons escape from the boundary of the cathode plasma and accelerate toward the anode. Since the boundary area of the cathode plasma is much larger than the area of electron emission from the cathode surface, the electron current at this time can break through the limit of the space charge effect, causing the conductive current in the gap and the external circuit to rise rapidly. Thus, the formation of the cathode plasma marks the beginning of the vacuum breakdown process. Due to the spatial density gradient and the friction with electrons (electrostatic friction), the ions in the cathode plasma move rapidly toward the anode at a velocity of the order of 10^4 m/s, which also causes further expansion of the region occupied by the cathode plasma, as shown in Figure 5-27(c). That is, the expansion of ions in the cathode plasma toward the anode is synchronized with the expansion of the cathode plasma, and both expand at the same rate. As the cathode plasma expands, the gap voltage decreases further while the gap current and external circuit current increase further. Figure 5-27(d) shows the situation when the front of the expanding cathode plasma reaches the anode. At this point the entire vacuum gap is occupied by the plasma and the voltage across the gap drops almost completely. This causes the gap to change from an insulating state to a fully conducting state, i.e., a conductive channel is formed. The cathode ions that reach the anode surface may undergo two processes after interacting with the anode surface: reflected back into the gap or causing sputtering of atoms from the anode surface. The sputtered and reflected atoms from the anode surface interact with electrons in the vicinity of the anode surface to produce the anode glow.

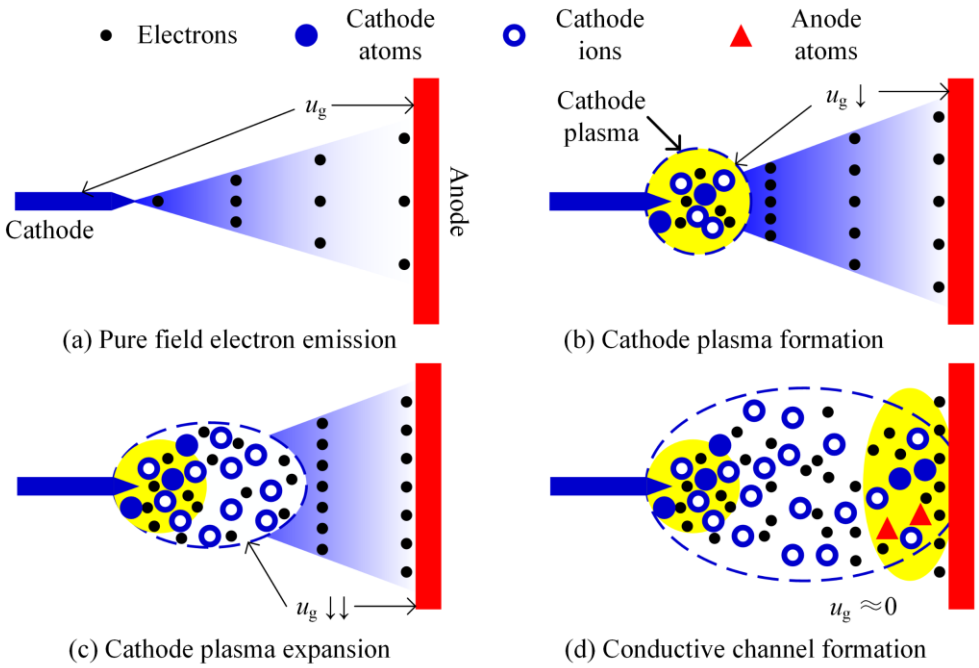

Figure 5-27 conductive channel in a vacuum breakdown

It should be noted here that the conclusion that the anode glow mainly results from the reflection of the cathode atoms and the sputtering of the anode atoms was obtained under the experimental conditions of this work. The anode glow in this situation does not mean the generation of an anode plasma. However, this conclusion does not deny the possibility of evaporation and subsequent anode glow from the anode under the heating effect of the electron flow. In fact, both the evaporation process and the sputtering process on the anode surface are the result of cathode plasma expansion. The degree of contribution of the two processes to the anode glow depends on factors such as electrode structure, gap length, gap voltage, gap current, and anode material. When the experimental conditions are such that the energy flux of the cathode electron beam at the anode is low, which is the case in this work, the evaporation process at the anode surface is not as significant as the sputtering process. On the contrary, if the gap current is sufficiently high or the gap size is sufficiently small, the electron beam may develop a very high heating power on the anode surface, so high that not only a sufficient number of atoms can be generated by evaporation, but even a new plasma may be formed near the anode surface. The generation and expansion of the anode plasma (the anode glow) can accelerate the formation process of the conductive channel in the vacuum gap so that the drop of the gap voltage coincides with the instant when the anode glow connects the gap, as the results obtained by some previous researchers[76, 81]. However, it must be clarified that the appearance of the anode plasma (and/or the anode glow) is not a necessary condition for the establishment of the conductive channel. As the experimental results of this study show, the expansion of the cathode plasma is sufficient to transform the vacuum gap from an insulating state to a fully conducting state, while the emergence and expansion of the anode glow is only a secondary effect of the expansion of the cathode plasma, which has no decisive effect on the formation of the conductive channel. Therefore, this research analyzes the role of the relevant physical processes in the conductive channel

formation stage of vacuum breakdown from the perspective of sufficiency and necessity, and clarifies the formation mechanism of the conductive channel, which is a significant addition and improvement to the existing theories for conductive channel formation and enhances the rigor of the conductive channel formation theory.

According to the results of this work, in the insulation design process of vacuum equipment such as vacuum circuit breakers and particle accelerators, the cathode and anode need to be optimized separately from different perspectives to obtain higher insulation capability. Since the generation and expansion of cathode plasma is a sufficiency and necessary condition for the formation of conductive channels, the design of cathodes should be aimed at limiting cathode plasma formation. Specifically, a material with a high breakdown threshold should be selected as the cathode material and microscopic defects on the cathode surface should be minimized. Although the anode glow and the anode plasma are not necessary for the conductive channel formation, the anode plasma generated by the excessive heating of the anode by the electron flow will promote and accelerate the formation of the conductive channel. Therefore, the anode should be designed with the goal of limiting the evaporation process on the anode surface. Specifically, materials with high thermal conductivity and low saturated vapor pressure can be chosen as anodes, or separate cooling of the anode can be tried. In addition, the design of the electrode structure should seek to reduce the concentration of the cathode electron flow as it reaches the anode surface, thus reducing the density of the energy flow into the anode. Therefore, the design of vacuum insulation should be based on the premise of good insulation of the cathode, and try to prevent the anode from generating local high temperature and anode plasma due to the heating of electron flow, so that the cathode insulation capacity could be brought to its maximum potential.

6 CONCLUSIONS

This dissertation investigated the physical processes involved in the conductive channel formation stage of vacuum breakdown, aiming to analyze the role of cathode, anode and various related physical processes in the transition of vacuum gap from insulating to conducting state and to improve the existing theory on the conductive channel formation in vacuum breakdown. The study used experimental tools such as high-speed imaging by ICCD camera, continuous-time imaging by streak camera, spectral analysis, microscopic morphology analysis, and energy spectrum analysis to observe and analyze the electrical signals, optical radiation signals, electrode surface morphology, and electrode surface composition during the vacuum breakdown process, and also established a simulation model of the vacuum breakdown process based on the PIC-MCC method. Based on the analysis of the experimental and simulation results, the intrinsic mechanism of the main physical phenomena in the vacuum breakdown process and their interrelationships are clarified. The roles played by the cathode and anode in the establishment of the conductive channel are clarified from the viewpoints of sufficiency and necessity. The mechanism for the formation of the conductive channel in the vacuum breakdown process is revealed. The main conclusions of this paper are as follows:

(1) The critical role of cathode plasma for the onset of vacuum breakdown is revealed, and the necessity of high temperature and ablation on the cathode surface for the formation and maintenance of cathode plasma is elucidated, providing evidence for a cathode-dominated breakdown mechanism. The experimental results in this paper show that the start of vacuum breakdown process is all predicated on the cathode surface electric field strength reaching the breakdown threshold (160±30 MV/m). The nanosecond-resolved images show the appearance of the cathode glow immediately after the onset of vacuum breakdown, and the comparative analysis of the current shows that the appearance of the cathode glow implies the generation of the cathode plasma. According to the simulation results of vacuum breakdown process, before the formation of cathode plasma, only electron emission current limited by space charge effect can flow in the vacuum gap, while the formation of cathode plasma can make the gap current break through the limit of space charge effect and rise rapidly, thus starting the construction process of vacuum breakdown conductive channel. Therefore, the formation of cathode plasma is a necessary condition for the beginning of vacuum breakdown and the development of conductive channels. In addition, simulations of the vacuum breakdown process and experimentally obtained changes in cathode micromorphology indicate that the formation of cathode plasma requires sufficient amount of atoms provided by ablation at the cathode surface due to elevated temperatures. The above results support the cathode-dominated vacuum breakdown mechanism.

(2) The origin of the particle components of the anode glow and the corresponding physical processes on the anode surface during the conductive channel formation stage

of vacuum breakdown are clarified, and a new mechanism for the anode glow existence based on the joint contribution of both electrodes and the sputtering process on the anode surface is proposed.

a) In terms of the particle composition of the anode glow, it was found that both the cathode and the anode contribute to the anode glow process, in contrast to the conventional view that the anode glow is produced by the anode. Spectroscopic and energy spectral analysis shows that the atoms provided by the cathode to the anode glow belong to the cathode material, they are the result of charge neutralization and reflection of the cathode material ions in the expanding cathode plasma upon arrival at the anode, and they have arrived at the anode surface before the appearance of the anode glow. The atoms provided by the anode to the anode glow contain both anode material and cathode material because the material migration in the preceding breakdowns can form a cathode material contamination layer on the anode surface. The increase of this contamination layer will lead to smaller and smaller percentage of atoms of the native anode material in the anode glow region, which is manifested by the attenuation or even complete disappearance of the spectra of the anode material in the anode glow.

b) In terms of the electrode physical processes corresponding to the anode glow, it was found that the mechanism leading to the escape of the anode surface atoms from the anode and their participation in the anode glow under the experimental conditions of this study is the sputtering of the anode surface under the bombardment of the cathode ion stream, rather than the evaporation of the anode surface under the heating of the cathode electron stream. This is because: ①the maximum difference in the density of evaporated atoms generated by different anode materials under the heating of the electron flow can be up to 11 orders of magnitude, while the instant of the anode glow appearance is very close; ②microscopic analysis shows that the anode surface does not melt in the breakdown process, which implies that it is impossible to produce intense evaporation due to high temperature; ③anode surface temperature and evaporated atom density is very sensitive to changes in the distribution radius of the electron flow from the cathode on the anode surface and if the distribution radius of the electron flow is estimated based on the fact that no melting occurs on the anode surface, the resulting evaporated atom density is likely to be much lower than the level capable of producing optical radiation; ④the sputtering effect of the cathode ion flow on the anode surface can produce sputtered atom densities up to the order of 10^{20} m^{-3}, and the sputtered atom density is not sensitive to changes in the distribution radius of the ion flow. This finding indicates that the degree of contribution of the evaporation process and sputtering process on the anode surface to the anode glow varies with the experimental conditions, and forms an important complement to the conventional view that the anode glow comes from the evaporation of the anode surface under heating.

(3) The dependence of the conductive channel establishment process on the anode glow generation and light-radiation channel formation is excluded, and the non-necessity of the anode glow in the formation of the conductive channel during vacuum breakdown is elucidated. According to the experimentally obtained gap voltage

waveform and the temporal evolution of the anode glow, the instant of gap voltage collapse during vacuum breakdown is much earlier than the instant when the expanding anode glow connects to the gap. This means that the expansion of the anode glow is not a necessary condition for the formation of the conductive channel. In addition, the instants of the anode glow appearance and the conductive channel formation have a strong linear correlation, but the sequential order of the two events has a random nature. This means that the emergence of the anode glow and the establishment of the conductive channel depend on the same process, i.e., cathode plasma expansion, but there is no causal relationship between the anode glow emergence and the conductive channel formation. Thus, both the appearance of the anode glow and the formation of the conductive channel are the result of the expansion of the cathode plasma to the anode, but neither the production nor the expansion of the anode glow is necessary for the formation of the conductive channel. Some of the previous conclusions emphasizing the importance of the anode glow are only phenomenological descriptions obtained in the special situation when the anode is overheated by the electron flow, which do not prove the necessity of the anode glow for the conductive channel formation.

(4) The expansion mode of the cathode plasma in the absence of light emission is discovered, and the sufficiency and necessity of the generation and expansion of the cathode plasma for the formation of the conductive channel in vacuum breakdown is clarified. A new mechanism for the establishment of conductive channels dominated by the cathode plasma expansion is proposed, which compliments the existing theories for conductive channel formation. The spectral analysis shows that although the expansion of the cathode glow region is very limited, the cathode plasma can continuously expand along the gap toward the anode without glowing, and the time of reaching the anode precedes the appearance of the anode glow. The simulation results show that the front of the cathode plasma expansion is determined by the ion expansion velocity. The region between the front and the cathode is occupied by plasma composed of electrons and ions with a low voltage drop, while the region between the front and the anode bears most of the gap voltage, with only electrons in the region moving toward the anode under the acceleration of the electric field to maintain the current conservation. The expansion of the cathode plasma causes the gradual decrease of the gap voltage and the gradual increase of the gap current. When the cathode plasma front reaches the anode surface, the whole vacuum gap is connected by the plasma, leading to complete drop of the gap voltage and the formation of the conductive channel. Therefore, the generation and expansion of the cathode plasma is a sufficient condition for the formation of the conductive channel. Moreover, according to the first conclusion, the generation of the cathode plasma is a necessary condition for the initiation of the vacuum breakdown process, and the continuous burning and expansion of the cathode plasma is a necessary condition for the further rise of the current and the development of the vacuum breakdown. Therefore, the generation and expansion of the cathode plasma is also a necessary condition for the establishment of the conductive channel. In summary, the necessary and sufficient condition for the formation of the conductive channel in the vacuum breakdown process is the generation and expansion of the cathode plasma.

ACKNOWLEDGEMENTS

With this dissertation finished, my PhD career is coming to an end. During the seven years of scientific research, there have been successes and joys, as well as failures and sorrows. Fortunately, at the age of 30, I have finally completed my studies successfully. What is more fortunate is that I have been accompanied by mentors and friends along the way. On this occasion of completing my dissertation, I would like to express my heartfelt thanks to my supervisors, colleagues, friends and family members for their selfless help in my research and life.

First of all, I would like to sincerely thank my supervisor, Prof. Yingsan Geng from Xi'an Jiaotong University. From the selection of doctoral project to the writing of dissertation, my whole research journey has been filled with Prof. Geng's great efforts. I was impressed by his meticulous work attitude, serious teaching style, profound professional knowledge and keen academic thinking, and he is a model for me to follow throughout my life. I would like to express my high respect and sincere gratitude to Prof. Yingsan Geng.

Meanwhile, I would like to thank my co-supervisor, Prof. Flyura Djurabekova. I was very lucky to receive funding from the China Scholarship Council to conduct my research as a joint PhD student at the University of Helsinki, Finland. During this period, Prof. Flyura Djurabekova provided me with great support as my supervisor. Her novel scientific ideas and rigorous logical thinking have inspired me greatly. I am also grateful to Prof. Kai Nordlund and Dr. Andreas Kyritsakis for their help during my stay in Finland.

In addition, I would like to thank Dr. Zhenxing Wang, and the other members of my two groups in China and Finland, who are not only my companions in research, but also my close friends in life. The springs, summers, autumns and winters we spent together will be the most precious memories of my life.

Finally, I would like to express my deepest gratitude to my parents. They have worked hard to bring me up and have been supporting me all along. Their love and support are my most solid backing.

REFERENCES

[1] P. G. Slade, *The Vacuum Interrupter: Theory, Design and Application*, Boca Raton: CRC press, 2007.

[2] J. S. Townsend, *The theory of ionization of gases by collision*, London: Constable & Company LTD, 1910.

[3] H. Wiedemann, *Particle accelerator physics*, New York: Springer Nature, 2015.

[4] A. Saressalo, A. Kyritsakis, F. Djurabekova, I. Profatilova, J. Paszkiewicz, S. Calatroni, and W. Wuensch, "Classification of vacuum arc breakdowns in a pulsed dc system," *Physical Review Accelerators and Beams,* vol. 23, no. 2, pp. 023101, 2020.

[5] W. Wuensch, "A review of vacuum breakdown in high-gradient accelerators." pp. 747-752.

[6] S. Dobert, C. Adolphsen, G. Bowden, D. Burke, J. Chan, V. Dolgashev, J. Frisch, K. Jobe, R. Jones, and J. Lewandowski, "High gradient performance of NLC/GLC X-band accelerating structures." pp. 372-374.

[7] J. Pappas, S. Pish, and M. Salinas, "Characterization of triggered vacuum switches for high current operation," *IEEE transactions on magnetics,* vol. 35, no. 1, pp. 367-371, 1999.

[8] M. Liao, Z. Fan, Z. Chen, T. Zhao, H. Zhang, and X. Duan, "Influence of Electrode Configurations on the Interruption Capacity of Laser Triggered Vacuum Switch," *IEEE Transactions on Plasma Science,* vol. 48, no. 6, pp. 2180-2186, 2020.

[9] J. De Lara, F. Pérez, M. Alfonseca, L. Galán, I. Montero, E. Román, and D. R. Garcia-Baquero, "Multipactor prediction for on-board spacecraft RF equipment with the MEST software tool," *IEEE Transactions on Plasma Science,* vol. 34, no. 2, pp. 476-484, 2006.

[10] N. Rozario, H. F. Lenzing, K. F. Reardon, M. S. Zarro, and C. G. Baran, "Investigation of Telstar 4 spacecraft Ku-band and C-band antenna components for multipactor breakdown," *IEEE transactions on microwave theory and techniques,* vol. 42, no. 4, pp. 558-564, 1994.

[11] S. Tabakov, "X-ray tube arcing: manifestation and detection during qualuty control," *MEDICAL PHYSICS INTERNATIONAL,* vol. 6, no. 1, pp. 157-161, 2018.

[12] M. A. Bashir, M. H. Sanhory, F. J. Alrasheed, A. Abdelrahman, and A. A. Abdullah, "X-ray Tube Arc Preventation by Stabilization of Voltage in a Dual Energy CT Scanner: A Review Study." pp. 1-6.

[13] L. Koch, A. Lesche, and W. Maring, "Fighting arcing and field emission in medical X-ray tubes." pp. 1077-1081.

[14] I. Brodie, and P. R. Schwoebel, "Vacuum microelectronic devices," *Proceedings of the IEEE,* vol. 82, no. 7, pp. 1006-1034, 1994.

[15] G. Meng, Y. Cheng, K. Wu, and L. Chen, "Electrical characteristics of nanometer gaps in vacuum under direct voltage," *IEEE Transactions on Dielectrics and Electrical Insulation,* vol. 21, no. 4, pp. 1950-1956, 2014.

[16] G. Meng, Y. Cheng, C. Dong, L. Chen, B. Zhu, and C. Men, "Effect of electrode geometry on the vacuum breakdown behaviors at nanoscale." pp. 1159-1162.

[17] O. A. Enholm, *Device for transforming and controlling electric currents*, U.S.

441542, U. S. Patent, 1890.
[18] D. M. Moore, *Magnetic Circuit Breaker*, U.S. 593230, 1897.
[19] D. M. Moore, *Interrupter for Electric Lighting Systems*, U.S. 604681, 1898.
[20] D. M. Moore, *Circuit Interrupting Mechanism*, U.S. 604687, 1898.
[21] D. M. Moore, *Electric Light Apparatus*, U.S. 672452, 1901.
[22] D. M. Moore, *Automatic Circuit Interrupter*, U.S. 702318, 1902.
[23] R. W. Sorensen, and H. E. Mendenhall, "Vacuum switching experiments at California Institute of Technology," *Transactions of the American Institute of Electrical Engineers,* vol. 45, no. 1, pp. 1102-1107, 1926.
[24] R. A. Millikan, and R. W. Sorensen, *Electrical Swiches*, G.B. 291815, 1926.
[25] J. Cobine, "Research and development leading to the high-power vacuum interrupter-A historical review," *IEEE Transactions on Power Apparatus and Systems,* vol. 82, no. 65, pp. 201-217, 1963.
[26] K. Takayama, and R. J. Briggs, *Induction accelerators*, New York: Springer Science & Business Media, 2010.
[27] S. Humphries, *Principles of charged particle acceleration*, New York: Courier Corporation, 2013.
[28] L. C. Teng, "Conceptual and technological evolutions of particle accelerators," *Chinese Physics C,* vol. 33, no. S2, pp. 112-114, 2009.
[29] M. Boland, U. Felzmann, P. Giansiracusa, T. Lucas, R. Rassool, C. Balazs, T. Charles, K. Afanaciev, I. Emeliantchik, and A. Ignatenko, *Updated baseline for a staged Compact Linear Collider*, Geneva: CERN Publishing, 2016.
[30] A. Saressalo, I. Profatilova, W. L. Millar, A. Kyritsakis, S. Calatroni, W. Wuensch, and F. Djurabekova, "Effect of dc voltage pulsing on high-vacuum electrical breakdowns near Cu surfaces," *Physical review accelerators and beams,* vol. 23, no. 11, pp. 113101, 2020.
[31] A. Descoeudres, Y. Levinsen, S. Calatroni, M. Taborelli, and W. Wuensch, "Investigation of the dc vacuum breakdown mechanism," *Physical Review Special Topics-Accelerators and Beams,* vol. 12, no. 9, pp. 092001, 2009.
[32] M. Jacewicz, V. Ziemann, T. Ekelöf, A. Dubrovskiy, and R. Ruber, "Spectrometers for RF breakdown studies for CLIC," *Nuclear Instruments and Methods in Physics Research Section A: Accelerators, Spectrometers, Detectors and Associated Equipment,* vol. 828, no. 1, pp. 63-71, 2016.
[33] D. K. Davies, and M. A. Biondi, "Vacuum electrical breakdown between plane-parallel copper electrodes," *Journal of applied physics,* vol. 37, no. 8, pp. 2969-2977, 1966.
[34] R. H. Fowler, and L. Nordheim, "Electron emission in intense electric fields," *Proceedings of the Royal Society of London. Series A, Containing Papers of a Mathematical and Physical Character,* vol. 119, no. 781, pp. 173-181, 1928.
[35] W. P. Dyke, J. Trolan, E. Martin, and J. Barbour, "The field emission initiated vacuum arc. I. Experiments on arc initiation," *Physical review,* vol. 91, no. 5, pp. 1043-1054, 1953.
[36] G. Mesyats, *Cathode phenomena in a vacuum discharge : the breakdown, the spark and the arc*, Moscow: Nauka, 2000.
[37] B. Jüttner, "Cathode spots of electric arcs," *Journal of Physics D: Applied Physics,* vol. 34, no. 17, pp. R103, 2001.
[38] H. Ma, Z. Zhang, Z. Liu, Z. Wang, Y. Geng, and J. Wang, "Anode current density distribution measurements for different vacuum arc modes subjected to axial magnetic field," *IEEE Transactions on Plasma Science,* vol. 43, no. 8, pp. 2335-

2344, 2015.
[39] S. Jia, Z. Shi, and L. Wang, “Vacuum arc under axial magnetic fields: experimental and simulation research,” *Journal of Physics D: Applied Physics,* vol. 47, no. 40, pp. 403001, 2014.
[40] R. L. Boxman, D. M. Sanders, and P. J. Martin, *Handbook of vacuum arc science & technology: fundamentals and applications*, New Jersey: Noyes Publications, 1996.
[41] X. Zhang, L. Wang, J. Ma, Y. Wang, and S. Jia, “Improved model for cathode spot crater in vacuum arc,” *Journal of Physics D: Applied Physics,* vol. 52, no. 3, pp. 035204, 2018.
[42] L. Wang, X. Zhang, J. Li, M. Luo, and S. Jia, “Study of cathode-spot crater and droplet formation in a vacuum arc,” *Journal of Physics D: Applied Physics,* vol. 54, no. 21, pp. 215202, 2021.
[43] W. Dolan, W. Dyke, and J. Trolan, “The field emission initiated vacuum arc. II. The resistively heated emitter,” *Physical review,* vol. 91, no. 5, pp. 1054-1057, 1953.
[44] C. Child, “Discharge from hot CaO,” *Physical Review (Series I),* vol. 32, no. 5, pp. 492-511, 1911.
[45] W. Boyle, P. Kisliuk, and L. Germer, “Electrical breakdown in high vacuum,” *Journal of Applied Physics,* vol. 26, no. 6, pp. 720-725, 1955.
[46] H. Anderson, “Effect of total voltage on breakdown in vacuum,” *Electrical Engineering,* vol. 55, no. 7, pp. 830-831, 1936.
[47] A. Denholm, “The electrical breakdown of small gaps in vacuum,” *Canadian Journal of Physics,* vol. 36, no. 4, pp. 476-493, 1958.
[48] D. Alpert, D. Lee, E. Lyman, and H. Tomaschke, “Initiation of electrical breakdown in ultrahigh vacuum,” *Journal of Vacuum Science and Technology,* vol. 1, no. 2, pp. 35-50, 1964.
[49] P. G. Slade, *Electrical contacts: principles and applications*: CRC press, 2017.
[50] J. M. Lafferty, *Vacuum arcs: Theory and applications*, New York: John Wiley & Sons, 1980.
[51] Y. Yu, J. Wang, H. Yang, Y. Geng, and Z. Liu, “Asymmetrical AC field emission current characteristics of vacuum interrupters subjected to inrush current,” *IEEE Transactions on Dielectrics and Electrical Insulation,* vol. 23, no. 1, pp. 49-57, 2016.
[52] S. Li, Y. Geng, Z. Liu, and J. Wang, “" V" shape curves of physical parameters of field emitters versus applied voltage toward breakdown in vacuum,” *IEEE Transactions on Dielectrics and Electrical Insulation,* vol. 25, no. 2, pp. 749-755, 2018.
[53] G. A. Mesyats, and D. I. Proskurovsky, *Pulsed Electrical Discharge in Vacuum*, Heidelberg: Springer‐Verlag Berlin, 1989.
[54] A. Descoeudres, T. Ramsvik, S. Calatroni, M. Taborelli, and W. Wuensch, “DC breakdown conditioning and breakdown rate of metals and metallic alloys under ultrahigh vacuum,” *Physical review special topics-accelerators and beams,* vol. 12, no. 3, pp. 032001, 2009.
[55] W. Wuensch, *Advances in the understanding of the physical processes of vacuum breakdown*, CERN, Geneva, 2013.
[56] F. Charbonnier, R. Strayer, L. Swanson, and E. Martin, “Nottingham effect in field and t− f emission: Heating and cooling domains, and inversion temperature,” *Physical Review Letters,* vol. 13, no. 13, pp. 397-401, 1964.

[57] G. Mesyats, "Ecton mechanism of the vacuum arc cathode spot," *IEEE transactions on plasma science,* vol. 23, no. 6, pp. 879-883, 1995.
[58] G. Mesyats, "Ectons in electric discharges," *JETP letters,* vol. 57, no. 2, pp. 95-98, 1993.
[59] Y. Yen, D. Tuma, and D. Davies, "Emission of electrode vapor resonance radiation at the onset of impulsive breakdown in vacuum," *Journal of applied physics,* vol. 55, no. 9, pp. 3301-3307, 1984.
[60] G. N. Fursey, *Field emission in vacuum microelectronics*, New York: Springer Science & Business Media, 2007.
[61] H. Timko, K. Ness Sjobak, L. Mether, S. Calatroni, F. Djurabekova, K. Matyash, K. Nordlund, R. Schneider, and W. Wuensch, "From field emission to vacuum arc ignition: A new tool for simulating copper vacuum arcs," *Contributions to Plasma Physics,* vol. 55, no. 4, pp. 299-314, 2015.
[62] H. Timko, K. Matyash, R. Schneider, F. Djurabekova, K. Nordlund, A. Hansen, A. Descoeudres, J. Kovermann, A. Grudiev, and W. Wuensch, "A One‐Dimensional Particle‐in‐Cell Model of Plasma Build‐Up in Vacuum Arcs," *Contributions to Plasma Physics,* vol. 51, no. 1, pp. 5-21, 2011.
[63] A. Kyritsakis, M. Veske, K. Eimre, V. Zadin, and F. Djurabekova, "Thermal runaway of metal nano-tips during intense electron emission," *Journal of Physics D: Applied Physics,* vol. 51, no. 22, pp. 225203, 2018.
[64] E. L. Murphy, and R. Good Jr, "Thermionic emission, field emission, and the transition region," *Physical review,* vol. 102, no. 6, pp. 1464-1473, 1956.
[65] A. Kyritsakis, and F. Djurabekova, "A general computational method for electron emission and thermal effects in field emitting nanotips," *Computational Materials Science,* vol. 128, pp. 15-21, 2017.
[66] G. Beukema, "Electrical breakdown properties of stainless steel and titanium electrodes in ultra-high vacuum," *Physica B+ C,* vol. 103, no. 2-3, pp. 397-411, 1981.
[67] T. Utsumi, "Cathode‐and Anode‐Induced Electrical Breakdown in Vacuum," *Journal of applied physics,* vol. 38, no. 7, pp. 2989-2997, 1967.
[68] C. J. Bennette, L. W. Swanson, and F. M. Charbonnier, "Electrical breakdown between metal electrodes in high vacuum. II. experimental," *Journal of Applied Physics,* vol. 38, no. 2, pp. 634-640, 1967.
[69] F. M. Charbonnier, C. J. Bennette, and L. W. Swanson, "Electrical breakdown between metal electrodes in high vacuum. I. Theory," *Journal of Applied Physics,* vol. 38, no. 2, pp. 627-633, 1967.
[70] I. Chalmers, and B. Phukan, "Breakdown time lags in short vacuum gaps," *Vacuum,* vol. 32, no. 3, pp. 145-150, 1982.
[71] B. Jüttner, "Vacuum breakdown," *Nuclear Instruments and Methods in Physics Research Section A: Accelerators, Spectrometers, Detectors and Associated Equipment,* vol. 268, no. 2-3, pp. 390-396, 1988.
[72] D. K. Davies, and M. A. Biondi, "The Effect of Electrode Temperature on Vacuum Electrical Breakdown between Plane‐Parallel Copper Electrodes," *Journal of Applied Physics,* vol. 39, no. 7, pp. 2979-2990, 1968.
[73] J. R. Lamarsh, and A. J. Baratta, *Introduction to nuclear engineering*, Upper Saddle River: Prentice hall, 2001.
[74] X. Qiu, J. Su, Y. Zhang, B. Zeng, M. Li, J. Cheng, L. Zhao, X. Xu, B. Yu, and R. Li, "Investigation of vacuum gap breakdown under microsecond pulses,"

IEEE Transactions on Dielectrics and Electrical Insulation, vol. 25, no. 6, pp. 2040-2048, 2018.
[75] B. Mazurek, J. Cross, and K. Srivastava, “Point-to-plane breakdown in vacuum at cryogenic temperatures,” *Physica B+ C,* vol. 104, no. 1-2, pp. 82-87, 1981.
[76] Y. Inada, T. Kamiya, S. Matsuoka, A. Kumada, H. Ikeda, and K. Hidaka, “Two-dimensional electron density visualization over plasma flare in vacuum breakdown process,” *Journal of Applied Physics,* vol. 124, no. 8, pp. 083301, 2018.
[77] X. D. Qiu, J. C. Su, Y. Zhang, Z. M. Yao, B. Zeng, R. Li, J. Cheng, L. Zhao, and W. P. Yan, "Optical diagnosis of vacuum breakdown characteristics under microsecond pulse." pp. 202-205.
[78] B. Mazurek, A. Nowak, and A. Tyman, “X-ray emission accompanying cathode microdischarge,” *IEEE transactions on electrical insulation,* vol. 28, no. 4, pp. 488-493, 1993.
[79] B. Mazurek, and J. Cross, “Fast cathode processes in vacuum discharge development,” *Journal of applied physics,* vol. 63, no. 10, pp. 4899-4904, 1988.
[80] G. Mesyats, "The role of fast processes in vacuum breakdown." pp. 333-336.
[81] I. Chalmers, and B. Phukan, “Photographic observations of impulse breakdown in short vacuum gaps,” *Journal of Physics D: Applied Physics,* vol. 12, no. 8, pp. 1285-1292, 1979.
[82] A. Maitland, and R. Hawley, “High speed photographs of vacuum sparks at voltages up to 250 kV,” *Vacuum,* vol. 18, no. 7, pp. 403-408, 1968.
[83] W. Yang, Q. Zhou, Q. Sun, and Z. Dong, “Two-dimensional particle simulation on the behavior of multi-charged copper ions in the cathode spot of a pulsed vacuum arc discharge,” *Journal of Applied Physics,* vol. 126, no. 24, pp. 243303, 2019.
[84] D. L. Shmelev, and S. A. Barengolts, “Modeling of cathode plasma flare expansion,” *IEEE Transactions on Plasma Science,* vol. 41, no. 8, pp. 1964-1968, 2013.
[85] E. Nefedtsev, and A. Batrakov, "Plasma expansion in vacuum gap: Three-fluid hydrodynamic simulation." pp. 1-4.
[86] E. Nefedtsev, and A. Batrakov, “Simulations of the stable expansion of a monoelement three-component explosive-emission plasma,” *Journal of Experimental and Theoretical Physics,* vol. 126, no. 4, pp. 541-549, 2018.
[87] E. Nefedtsev, and A. Batrakov, “Numerical simulations of stable explosive-emission center plasma expansion in vacuum,” *Journal of Experimental and Theoretical Physics,* vol. 121, no. 4, pp. 706-716, 2015.
[88] O. Morimiya, “Theoretical and experimental study of a high‐current vacuum arc in a uniform axial magnetic field,” *Journal of applied physics,* vol. 71, no. 1, pp. 101-107, 1992.
[89] H. Schellekens, “The high‐current vacuum arc in an axial magnetic field: An experimental investigation,” *Journal of applied physics,* vol. 54, no. 1, pp. 144-149, 1983.
[90] A. Anders, “The evolution of ion charge states in cathodic vacuum arc plasmas: a review,” *Plasma Sources Science and Technology,* vol. 21, no. 3, pp. 035014, 2012.
[91] A. Anders, and G. Y. Yushkov, “Ion flux from vacuum arc cathode spots in the absence and presence of a magnetic field,” *Journal of Applied Physics,* vol. 91, no. 8, pp. 4824-4832, 2002.

[92] I. Krinberg, “Acceleration of a multicomponent plasma in the cathode region of a vacuum arc,” *Technical Physics,* vol. 46, no. 11, pp. 1371-1378, 2001.
[93] G. Y. Yushkov, A. Bugaev, I. Krinberg, and E. Oks, "On a mechanism of ion acceleration in vacuum arc-discharge plasma." pp. 307-309.
[94] P. A. Ni, and A. Anders, “Supersonic metal plasma impact on a surface: an optical investigation of the pre-surface region,” *Journal of Physics D: Applied Physics,* vol. 43, no. 13, pp. 135201, 2010.
[95] M. Berger, J. Coursey, M. Zucker, and J. Chang, “Stopping-power and range tables for electrons, protons, and helium ions (2005),” *Available on http://physics.nist.gov*, 2015.
[96] J. Ziegler, J. Biersack, and M. Ziegler. "SRIM-2008 software package," Available on http://www.srim.org.
[97] E. Hantzsche, “Consequences of balance equations applied to the diffuse plasma of vacuum arcs,” *IEEE Transactions on Plasma Science,* vol. 17, no. 5, pp. 657-660, 1989.
[98] A. Anders, S. Anders, A. Forster, and I. G. Brown, “Pressure ionization: its role in metal vapour vacuum arc plasmas and ion sources,” *Plasma Sources Science and Technology,* vol. 1, no. 4, pp. 263-270, 1992.
[99] Z. Zhou, Z. Wang, Z. Zha, Y. Li, L. Sun, H. Li, and Y. Geng, “Anodic Glow and Conductive Channel Formation in Single and Double Long Vacuum Gaps,” *IEEE Transactions on Dielectrics and Electrical Insulation,* vol. 28, no. 1, pp. 207-214, 2021.
[100] G. Djogo, and J. D. Cross, “Circuit modeling of a vacuum gap during breakdown,” *IEEE Transactions on Plasma Science,* vol. 25, no. 4, pp. 617-624, 1997.
[101] G. Djogo, and J. Cross, “Dependence of gap voltage collapse during vacuum breakdown on geometry and plasma dynamics,” *IEEE transactions on dielectrics and electrical insulation,* vol. 4, no. 6, pp. 848-853, 1997.
[102] C. Nieter, and J. R. Cary, “VORPAL: a versatile plasma simulation code,” *Journal of Computational Physics,* vol. 196, no. 2, pp. 448-473, 2004.
[103] C. K. Birdsall, and A. B. Langdon, *Plasma physics via computer simulation*, New York: CRC press, 2004.
[104] A. Anders, *Cathodic arcs: from fractal spots to energetic condensation*, New York: Springer Science & Business Media, 2009.
[105] H. Kaufmann, M. Cunha, M. S. Benilov, W. Hartmann, and N. Wenzel, “Detailed numerical simulation of cathode spots in vacuum arcs: Interplay of different mechanisms and ejection of droplets,” *Journal of Applied Physics,* vol. 122, no. 16, pp. 163303, 2017.
[106] A. Tkachev, A. Fedenev, and S. Yakovlenko, “Townsend coefficient, escape curve, and fraction of runaway electrons in copper vapor,” *Laser physics,* vol. 17, no. 6, pp. 775-781, 2007.
[107] D. Wang, L. Wang, J. Liu, and S. Jia, “2D particle-in-cell/Monte Carlo collisional simulation of the plasma initiation in the vacuum breakdown stage,” *Journal of Physics D: Applied Physics,* vol. 53, no. 3, pp. 035201, 2020.
[108] W. Yang, Q. Zhou, W. Yang, Y. Dong, and Z. Dong, “The accuracy of collision cross sections in particle modeling on copper vacuum arcs,” *Physics of Plasmas,* vol. 25, no. 6, pp. 063521, 2018.